

OPTICAL PROBING OF LASER PRODUCED PLASMAS

by

Y. B. S. R. PRASAD

PHYS 03 2009 04 001

Raja Ramanna Centre for Advanced Technology, Indore

A thesis submitted to the

Board of Studies in Physical Sciences

In partial fulfilment of requirements

for the Degree of

DOCTOR OF PHILOSOPHY

of

HOMI BHABHA NATIONAL INSTITUTE



August, 2016

Homi Bhabha National Institute


Recommendation of the Viva Voce Board

As members of the Viva Voce Board, we certify that we have read the dissertation prepared by *Shri Y B S R Prasad* entitled "*Optical probing of laser-produced plasmas*" and recommend that it may be accepted as fulfilling the dissertation requirement for the Degree of Doctor of Philosophy.


Chairman – Prof. P.D. Gupta Date: 16/07/2018


Guide – Prof. P.A. Naik Date: 16/07/2018


Member – Prof. N.K. Gupta Date: 16/07/2018



Member – Prof. G.S. Lodha Date: _____


External Examiner – Prof. Alike Khare, IIT, Guwahati Date: 16/07/2018

Final approval and acceptance of this dissertation is contingent upon the candidate's submission of the final copies of the dissertation to HBNI.

I hereby certify that I have read this dissertation prepared under my direction and recommend that it may be accepted as fulfilling the dissertation requirement.

Date: 16/07/2018

Guide: 
(Prof. P. A. Naik)

Place: Indore.

STATEMENT BY AUTHOR

This dissertation has been submitted in partial fulfilment of requirements for an advanced degree [Ph.D.] at Homi Bhabha National Institute (HBNI) and is deposited in the Library to be made available to borrowers under rules of the HBNI.

Brief quotations from this dissertation are allowable without special permission, provided that accurate acknowledgement of source is made. Requests for permission for extended quotation from or reproduction of this manuscript in whole or in part may be granted by the Competent Authority of HBNI when in his / her judgement the proposed use of the material is in the interests of scholarship. In all other instances, however, permission must be obtained from the author.

(Y. B. S. R. Prasad)

DECLARATION

I, Y.B.S.R. Prasad, hereby declare that the investigations presented in the thesis have been carried out by me. The work is original and has not been submitted earlier as a whole or in part for any degree / diploma at this or any other Institution / University.

(Y. B. S. R. Prasad)

List of Publications arising from the thesis

Journal

1. "Chirped pulse shadowgraphy for single shot time-resolved plasma expansion measurements",
Y. B. S. R. Prasad, S. Barnwal, P.A. Naik, J. A. Chakera, R. A. Khan and P. D. Gupta,
Appl. Phys. Lett., **2010**, 96, 221503-1 - 221503-3.
2. "Chirped pulse interferometry for time resolved density and velocity measurements of laser produced plasmas" ,
Y. B. S. R. Prasad, S. Barnwal, P. A. Naik, J. A. Chakera and P. D. Gupta,
Journal of Applied Physics, **2011**, 110, 023305-1 - 023305-4.
3. "Study of self generated magnetic fields in laser produced plasmas using a three channel polaro- interferometer",
Y. B. S. R. Prasad, S. Barnwal, E. A. Bolkhovitinov, P. A. Naik, M. P. Kamath, A. S. Joshi, S. R. Kumbhare, A. A. Rupasov, and P. D. Gupta,
Review of Scientific Instruments, **2011**, 82, 123506-1 - 123506-5.
4. "Calculation of self-generated magnetic fields in laser produced plasmas"
Y. B. S. R. Prasad, S. Barnwal, P. A. Naik, E.A. Bolkhovitinov, A.A. Rupasov, and P.D. Gupta,
Journal of Russian Laser Research, **2015**, 36, 395- 402.
5. "Study of shock wave propagation in soda lime glass using optical shadowgraphy"
Y. B. S. R. Prasad, S. Barnwal, P. A. Naik, Y. Yadav, R. Patidar, M.P. Kamath, A.Upadhyay, S. Bagchi, A. Kumar, A.S. Joshi, and P.D. Gupta,
Pramana J. Physics, **2016**, 87:9, 1-8.

Conferences

1. "Study of self-generated magnetic fields in laser produced plasmas using a three-channel polaro-interferometer",
Y.B.S.R. Prasad, S. Barnwal, P.A. Naik, P.D. Gupta, E.A. Bolkhovitinov, and A. Rupasov.
“23rd National Symposium on Plasma Science and Technology”, PLASMA-08, Mumbai, Dec. 2008.
2. "A three-channel polaro-interferometer for detection and measurement of self-generated magnetic fields in laser produced plasmas",
S.Barnwal, **Y.B.S.R. Prasad**, P.A.Naik, P.D.Gupta, E.A. Bolkhovitinov, and A. Rupasov
DAE-BRNS National Laser Symposium 2008, New Delhi, an 2009.
3. "A novel single shot time-resolved optical diagnostics for plasma using a chirped laser pulse as probe",
S.Barnwal, **Y. B. S. R. Prasad**, P. A. Naik , J. A. Chakera , R. A. Khan , P. D. Gupta
24th National Symposium on Plasma Science & Technology, Hamirpur, 8-11 Dec. 2009.
4. "Time resolved chirped pulse interferometry of laser produced plasma",
S. Barnwal, **Y.B.S.R. Prasad**, P.A. Naik, J. A. Chakera, S. R. Kumbhare and P. D. Gupta
DAE-BRNS National Laser Symposium 2009, BARC Mumbai, Jan 13-16, 2010.
5. "Analysis of three channel polaro-interferometer data of self generated magnetic fields in laser produced plasmas",
Y.B.S.R. Prasad, S.Barnwal, P.A.Naik, P.D. Gupta.
25th National Symposium on Plasma Science & Technology, Guwahati, 8-11 Dec. 2010.
6. "Time resolved measurements of plasma expansion velocity using chirped pulse interferometry",
Y.B.S.R. Prasad, S. Barnwal, P.A. Naik, J.A. Chakera, S.R. Kumbhare, P.D. Gupta,
20th DAE-BRNS National Laser Symposium, Chennai, 9-12 Jan 2012.

7. "Chirped pulse shadowgraphy for studying the evolution of shock wave velocity",
Y.B.S.R.Prasad, S. Barnwal, R.K. Patidar, A.K. Sharma, A.S. Joshi, P.A. Naik, and P.D. Gupta,
29th National Symposium on Plasma Science & Technology, Kottayam, 8-11, Dec-2014.
8. "Temporal variation of shock wave velocity in soda-lime glass",
Y.B.S.R. Prasad, S. Barnwal, A.Upadhyay, M.P. Kamath, S. Bagchi, A. Kumar, A.S. Joshi, P.A. Naik, and P.D. Gupta,
29th National Symposium on Plasma Science & Technology, Kottayam, 8-11, Dec-2014.
9. "Observation of jet-like structures in the laser irradiated soda lime targets",
Y.B.S.R. Prasad, S.Barnwal, Y. Yadav, M.P. Kamath, A.S. Joshi, M. Goswami, P.A. Naik and P.D. Gupta,
24th DAE-BRNS National Laser Symposium, Dec 2-5, 2015 at RRCAT, Indore.

(Y. B. S. R. Prasad)

DEDICATION

I
dedicate this thesis
to
my parents
and
beloved teachers.

ACKNOWLEDGEMENTS

Over the years, a number of persons have helped me in this thesis. It may not be possible to acknowledge the help given by each of them. However, help from some of the major contributors is acknowledged here.

First and foremost, I would like to express my sincere, hearty thanks to my guide Prof. Prasad A. Naik for his continuous guidance and encouragement while doing experiments, during discussion about scientific problems, and analysis of the results. This was followed with many suggestions and continuous guidance in writing manuscripts. I am highly obliged to him for spending his invaluable time and efforts at various stages of the research work, thesis preparation, and finalization. His nature of dealing things in a simple and straight forward manner made life much easier for me.

I am highly thankful to Prof. P.D. Gupta for a number of things. There are things he taught me directly and there are things which I tried to learn from him. I am highly thankful to him for his help in writing my first paper on time resolved interferometry. With his keen acumen and clarity of thought, he gave us directions that improved on many fronts. Moreover, he motivated me enormously with his endless energy, persistence, and punctuality.

I would like to thank Prof. N.K. Gupta, Prof. L.J. Dhareshwar and Prof. G.S. Lodha for their helpful suggestions as members of my Doctoral Committee, in improving the quality of this research work.

My sincere thanks are due to Shri A.S. Joshi, Prof. J.A.Chakera, Prof. A. Moorti, Prof. M.P.Singh, (Drs.) S.Bagchi, A. Upadhyay, V. Arora, U.Chakravarty, H. Singhal and B.S.Rao for the helpful scientific discussions. Special thanks to Shri S. Barnwal, who has been a wonderful

team member in all the work reported in this thesis. Shri M.P. Kamath is a very good friend and extremely helpful colleague right from my days at BARC, with his contagious smile. My sincere thanks to Shri H.S. Vora for his enthusiastic support with his image analysis softwares PROMISE and TRILOCHAN which were valuable assets in my data analysis.

My team members Dr. A. Kumar, Dr. A.K. Sharma, Shri R.Patidar, Shri Deepak Daiya, Shri S.R. Kumbhare, Shri Atul Kumar, Shri A. P. Kulkarni, Smt. S. Jain, Shri R.A. Khan, Shri R.A. Joshi, Shri R.K. Bhat, Shri P.K. Tripathi, Shri J.D. Singh and Shri Patwa deserve praise and my heartfelt thanks for all their support during these experiments. Shri R.P. Kushwaha deserves special thanks for the prompt, timely help, as and when required.

Continuous support received from our colleagues from LESD, specially Shri C.P.Navathe, Dr. M.S.Ansari, Shri V.Bhanage, Smt J.Upadhyay, Shri Anand Valecha and Shri N.Sreedhar is gratefully acknowledged. Working with Shri S. Nigam, Shri K. Aneesh and Shri M.L.Sharma was always a pleasant experience.

Thanks to my international collaborators Prof. A.A. Rupasov and Dr. E. Bolkhotinov, from whom I have learnt some experimental techniques related to optical probing.

I am highly indebted to the strong support from my parents and family members, particularly my wife Suma during this period. My daughters Keerthana and Subha also helped me in completing the thesis by demanding less time from me at home.

Y.B.S.R. Prasad

CONTENTS

<i>SYNOPSIS</i>	1
<i>LIST OF FIGURES</i>	7
<i>LIST OF TABLES</i>	13
Chapter 1 : Introduction to Laser Produced Plasmas	1
1.1 Introduction	1
1.2 Generation of laser plasma	3
1.3 Characteristics of Laser Plasmas	4
1.3.1 Plasma frequency and the critical density	5
1.4 Absorption of laser light in Plasmas	7
1.4.1 Inverse Bremsstrahlung absorption	7
1.4.2 Resonance absorption	9
1.4.3 Absorption due to ion-acoustic turbulence	11
1.4.4 Comparison between three absorption processes	11
1.4.5 Losses due to stimulated scattering	12
1.5 Absorption processes with short (fs) laser pulses	13
1.5.1 Vacuum/Brunel heating	13
1.5.2 $\mathbf{j} \times \mathbf{B}$ heating	14
1.6 Self generated magnetic fields in laser produced plasmas	15
1.6.1 $\nabla n_e \times \nabla T_e$ mechanism	16
1.6.2 Fountain Effect	18
1.6.3 Inverse Faraday Effect	18
1.6.4 Weibel Instability	19

1.7 <i>Laser generated shock waves</i>	21
1.7.1 Mechanism of Shock Wave Generation	23
1.7.2 Scaling of shock pressure with laser intensity and wavelength	25
1.7.3. Shock Wave Propagation: Material Response	27
1.7.4 Shock Wave Propagation : Effect of Laser Pulse	33
1.8 <i>Conclusion</i>	34
Chapter 2 : Lasers for Plasma Experiments	35
2.1 <i>Introduction</i>	35
2.2 <i>High Power Laser System</i>	36
2.2.1 Oscillator 1 : SL-223	39
2.2.2 Oscillator 2 : Chameleon Ultra II	40
2.2.3 Image Relays / Spatial relays	41
2.2.4 Faraday Isolator	43
2.2.5 Control System	45
2.3 <i>10 TW femtosecond laser system</i>	45
2.3.1 Kerr lens mode locking	47
2.3.2 Chirped Pulse Amplification	49
2.3.3 Regen and Pre-Amplifiers	52
2.3.4 Pulse Compressor	53
Chapter 3 : Diagnostics for Laser Produced Plasmas	56
3.1 <i>Introduction</i>	56
3.2 <i>Time resolved studies using snap shot / multi-frame approach</i>	58
3.2.1 Generation of the probe beam	60

3.2.2 Duration of the probe pulse	60
3.2.3 Wavelength of the probe beam	62
3.3 <i>Time resolved studies using multi-frame diagnostics</i>	64
3.4 <i>Time resolved studies using streak camera, chirped probes pulses</i>	64
3.4.1 Time resolved studies using Streak Camera	65
3.4.2 Chirped pulse diagnostics	68
3.5 <i>Conclusions</i>	70
Chapter 4 : Chirped Pulse Diagnostics for Laser Plasmas	72
4.1 <i>Introduction</i>	72
4.2 <i>Generation of Chirped Pulses and Their Characterization</i>	74
4.3 <i>Temporal Characterization of the probe pulse</i>	76
4.4 <i>Experimental Setup</i>	79
4.4.1 Setup for Shadowgraphy Measurements	80
4.4.2 Setup for Interferometry Measurements	83
4.5 <i>Results and Discussion</i>	86
4.5.1 Shadowgraphy Measurements	86
4.5.2 Interferometric Measurements	93
4.5.3 Advantages and disadvantages of chirped diagnostics	97
4.6 <i>Conclusions</i>	99
Chapter 5 : Detection of Self Generated Magnetic Fields	101
5.1 <i>Introduction</i>	101
5.2 <i>Optical setup of a three channel polaro-interferometer</i>	104

5.3	<i>Experimental Setup</i>	108
5.4	<i>Results and the Analysis of data</i>	112
5.4.1	Reproducibility of the measurements	119
5.5	<i>Conclusions</i>	122
Chapter 6 :	Shock wave propagation in transparent materials	123
6.1	<i>Introduction</i>	123
6.1.1	Basics of high pressure generation using shock wave	124
6.1.2	Methods of shock velocity measurements	126
6.2	<i>Chirped pulse shadowgraphy</i>	128
6.2.1	Description of experiment	128
6.2.2	Results and discussion	131
6.3	<i>Snapshot Shadowgraphy</i>	133
6.3.1	Results from snap shot shadowgraphy	134
6.4	<i>Analysis of shock wave velocity evolution</i>	136
6.4.1	Detection of ionization tracks	141
6.5	<i>Conclusions</i>	145
Chapter 7 :	Conclusions and Future Plans	146
7	<i>Optical probing of laser produced plasmas</i>	146
7.1	<i>Chirped Pulse Diagnostics</i>	146
7.2	<i>Detection of self generated magnetic fields</i>	147
7.3	<i>Equation of state studies</i>	148
Appendix A :	Streak Camera	149

<i>A.1 Introduction</i>	149
<i>A.2 Triggering the Streak Camera</i>	152
A.2.1 Using a photo-diode	153
A.2.2 Using the master clock of the oscillator	154
<i>A.3 Calibration procedure</i>	154
Appendix B : Abel Inversion	156
Appendix C : Calculation of Magnetic Fields	160
<i>C.1 Introduction</i>	160
<i>C.2 Steps of the program</i>	161
<i>C.3 Program</i>	167
<i>C.3.1 Two Dimensional Profile of the Rotation Angle</i>	167
<i>C.3.2 Calculation of the Density and Magnetic Fields</i>	168
ps: These programs are compatible with MATLAB version 2008a	174
References	175

SYNOPSIS

Optical Probing of laser produced plasmas

Laser produced plasmas, with their extreme characteristics of steep gradients in density (vacuum to 10^{23} cm^{-3}) and temperatures (up to hundreds of eV), have become an interesting medium to be studied for many applications. The typical physical dimensions of few hundreds of micron in space and short existence for a duration of less than few ns, has enhanced the interest in developing high resolution (spatial and temporal) diagnostics tools to probe these plasmas.

When a powerful laser beam is focussed onto a focal spot measuring few hundreds of microns, the laser intensities reach $10^{11-14} \text{ W/cm}^2$ in the case of nanosecond laser pulses and $10^{17-20} \text{ W/cm}^2$ for ultra-short, ultra-intense femto second laser pulses. At these intensities, many interesting phenomena occur during the laser - plasma interaction and immediately afterwards during the rapid expansion phase.

The typical temperature in such a plasma can reach as high as few hundreds of eV during a short span of time. The plasma generated from the nanosecond lasers has become an excellent point x-ray source for imaging applications. Similarly, magnetic fields of several mega gauss are generated in the laser produced plasmas. The magnetic fields of this order are very difficult to realize otherwise. The research area of the laser produced plasmas acquired its importance with the inertial confinement fusion concept which is pursued vigorously worldwide by developing Mega joule laser facilities like National Ignition Facility (NIF), USA, Laser Mega Joule (LMJ), France, Laboratory for Laser Energetics (LLE), USA, etc.

The appearance of femto second lasers has led to further increase in the laser power to several petawatt (PW). These lasers, when focussed, give rise to intensity $\sim 10^{21}$ W/cm². A completely new regime known as *relativistic laser plasma interaction* has unveiled several new phenomena which were unimaginable a few decades back. The acceleration of electrons to GeV is promising as a compact alternative to future linear accelerators. The acceleration of protons to tens of MeV range promises a medical tool to treat various malignancies with minimal collateral damage to the neighbouring tissues unlike the present radiation treatment. The generation of higher order harmonics is a very easy way to generate coherent radiation at shorter wavelengths, competing with free electron lasers (FEL). The generation of attosecond pulses will take the time resolved studies to newer heights unimaginable few years back.

In order to understand all these phenomena, one needs to study the laser plasmas in detail, with good spatial and temporal resolutions. Since the wavelength of the probing radiation puts an upper limit on the plasma densities that can be reached, probing with shorter wavelengths is preferred. Similarly, in order to study the dynamics of the laser plasma, one needs short duration probes. The optical probing of laser produced plasmas is an important diagnostics tool providing both spatially and temporally resolved information.

The present research work is concentrated around developing different types of optical probing techniques to study various phenomena in laser produced plasmas. To understand the expansion of plasma at ultra-short duration, ultra-high laser intensities, chirped pulse shadowgraphy (CPS) and chirped pulse interferometry (CPI) techniques have been developed. In order to study the evolution of the self generated magnetic fields in plasmas, a three channel polaro-interferometer has been used. Finally, in order to understand the evolution of propagation

of shock waves in transparent media, snap shot shadowgraphy and chirped pulse shadowgraphy techniques have been used for recording the forming and decay phases of the shock waves. The sequence of presentation of the work in the thesis is as follows.

Chapter 1 covers the basic mechanisms of plasma generation using lasers and the interaction of the laser with the plasma formed. As different types of lasers, from Q-switched nanosecond duration lasers to ultra-short femtosecond laser systems, are used in the present work, different absorption mechanisms play dominant roles in different regimes. These mechanisms are discussed in this chapter. Since a part of the work deals with self generated magnetic fields in laser produced plasmas, a brief introduction to different mechanisms leading to the generation of these fields are described in this chapter. Similarly, since another part of the work deals with generation and time resolved study of shock waves in laser produced plasmas, a brief introduction to the generation of high pressures and shock waves is also given in this chapter.

Chapter 2 covers different laser systems used in the present experimental work and the methods to characterize the laser pulses. Two types of lasers were used in the experiments. The first one is a nanosecond duration master oscillator power amplifier (MOPA) type of system in which a nanosecond pulse is amplified using a series of amplifiers. The system also consists of beam relay systems to relay the beam from one amplifier to the next, with proper magnification and spatial filtering. It has Faraday isolators to prevent back reflections of the laser pulse from the target into the laser system. The second type of laser is a commercial 10 TW, 45 fs Ti:sapphire laser system employing chirped pulse amplification to increase the energy. The laser system exhibits a large bandwidth ~ 20 nm (at the final stage, after amplification) around the

central wavelength of 796 nm. The fs laser pulses from the oscillator are stretched in time to ~ 200 ps (FWHM) for amplification using a pulse stretcher and compressed back to 45 fs using a evacuated compressor consisting of large gratings. The details of both the systems are given in this chapter.

Chapter 3 mainly covers the different diagnostic techniques used to get time resolved information about plasma. The advantages and limitations of these techniques are discussed. The first technique to be discussed is the snap shot approach in which a short duration probe pulse is passed tangentially to the laser produced plasmas and the transmitted beam profile is recorded using detectors like CCD or DSLR camera. In order to construct the time resolved picture of the phenomena under investigation, the delay between the probe and the main laser pulse is varied in different shots and experiments under identical conditions (energy, pulse duration etc.) are compared. An alternative to this i.e. Multi-frame snap shots is also discussed. As the information is integrated over the probe pulse duration, efforts are made to keep the probe duration as short as possible. The second approach is to use long probe duration but obtain the temporal information using a time dispersing instrument like an optical streak camera using which continuous temporal information is obtained in a single shot. With the advent of femtosecond laser systems, the chirped pulse amplification (CPA) technique has become a standard method in which the pulse is stretched in time, amplified using conventional techniques, and compressed back to the femtoseconds duration. The temporal stretching using gratings introduces a linear chirp in the frequencies, which can be used as a valuable temporal diagnostics tool simply by recording the spectrum of the transmitted probe beam. This is a simpler alternative to optical

streak camera and offers temporal resolutions of picoseconds and lower. These issues are briefly discussed in this chapter.

Chapter 4 covers the experimental work on the chirped pulse diagnostics viz. chirped pulse shadowgraphy and chirped pulse interferometry. These two novel techniques have been used to obtain the temporal evolution of the plasma expansion velocity and the plasma density over a continuous time period of ~ 400 ps with temporal resolution nearly 8 ps in a single shot. The shadowgraphy experiments revealed a sharp variation in the plasma expansion velocity from 10^7 cm/s for few hundreds of picoseconds immediately after the arrival of intense femtosecond laser pulse. The details about these experiments and the analysis of the results are presented in this chapter. A comparison is also made between time resolved interferometry carried out using an optical streak camera and a chirped probe pulse.

Chapter 5 discusses about an instrument "three channel polaro-interferometer" built to detect the self generated magnetic fields in laser produced plasmas. Using this instrument, the spatial profiles of the magnetic fields could be obtained. We have obtained the plasma density, and the magnetic field information, in addition to the spatial profile of the probe beam, by simultaneously using interferometry, polarimetry and shadowgraphy respectively. Initially the information retrieval from the three channel data was quite time consuming and laborious. An interactive MATLAB program was specifically developed to analyze the recorded images and to calculate the density and magnetic field information interactively. Details about the polaro interferometer and the data retrieval method has been discussed along with the results obtained.

Chapter 6 mainly deals with the shock propagation studies in the transparent targets of soda lime glass. High pressures of several mega bars are generated when a high intensity laser

pulse is incident on a target. When the laser produced plasmas expand rapidly in the outward direction, it launches a shock wave (compression wave) in the medium due to recoil momentum of the expanding plasma ions. During the ‘forming phase’ which occurs the first half of laser pulse (up to the peak of laser pulse), coalescing of shock waves occurs leading to the formation of a shock front. During this phase, the shock velocity increases in time. On the other hand, once the laser pulse is over, a rarefaction wave is launched at the front surface the target on which laser pulse incident. This waves travels much faster in the already compressed medium. The shock front decays once this rarefaction wave catches it in time. Thus, the study of shock velocity variation in time is quite interesting and this was accomplished in experiments in transparent soda lime targets using both : snap shot approach at discrete time steps and also over a continuous time period, using chirped pulse shadowgraphy.

In addition, an interesting phenomena associated with the filamentation occurring in the long scale length plasmas has been recorded using the snap shot shadowgraphy technique. Some thin channel like structures have been observed, with the length of the channel extending to $\sim 500 \mu\text{m}$ ($5\text{-}10 \mu\text{m}$ wide) at a delay of 1 ns between the heating and probing pulse. These structures have been attributed to the x-ray hotspots ($1\text{-}10 \text{ keV}$) generated in the dense laser produced plasmas due to small scale filamentation instabilities at higher intensities. These intense bursts of keV x-rays causing these long ionization tracks whose length depends on the x-ray energy, which in turn depends on the laser intensity. The experimental details and the results are discussed in the Chapter 6.

The last chapter, Chapter 7, summarizes different experimental observation and conclusions. The possible outlook and future directions of the work are also discussed here.

LIST OF FIGURES

Figure 1.1: <i>Spatial profile of the plasma density and temperature in long duration lasers</i>	4
Figure 1.2: <i>A schematic diagram of Resonance Absorption</i>	9
Figure 1.3: <i>Brunel (Vacuum) absorption mechanism</i>	14
Figure 1.4: <i>(a) Schematic of density and temperature gradients, and (b) generation of magnetic fields in laser plasmas</i>	17
Figure 1.5: <i>Schematic of fountain effect in laser produced plasmas generating magnetic fields</i>	18
Figure 1.6: <i>Inverse Faraday effect with circularly polarized light.</i>	19
Figure 1.7: <i>Weibel instability</i>	19
Figure 1.8: <i>Scaling of shock pressure with laser intensity</i>	27
Figure 1.9 <i>Shock wave propagation due to application of pressure at $x=0$, $t=0$</i>	28
Figure 1.10: <i>Hugoniot for a material</i>	29
Figure 1.11: <i>Hugoniot of a material with a elastic-plastic flow or phase transition</i>	30
Figure 1.12: <i>Shock wave coalescence forming a shock front</i>	33
Figure 2.1: <i>A photograph of the two beam high power laser system at RRCAT</i>	37
Figure 2.2: <i>A schematic diagram of the two arm high power laser chain at RRCAT</i>	38
Figure 2.3: <i>A schematic diagram of a Faraday isolator</i>	44
Figure 2.4: <i>A photograph of the 10 TW Ti:sapphire laser system at RRCAT.</i>	46
Figure 2.5 : <i>Overall schematic layout of the Ti:sapphire laser system.</i>	47

Figure 2.6: <i>Soft aperture Kerr-lens mode locking. Within crystal from inside to outside: Green=pump, blue, red are shorter and longer pulses (Courtesy: Wikipedia : Arnero)</i>	49
Figure 2.7: <i>The principle of laser chirped pulse amplification.</i>	50
Figure 2.8: <i>Pulse stretcher configuration using two gratings and an afocal telescope system.</i>	51
Figure 2.9: <i>Offner type Pulse Stretcher</i>	52
Figure 2.10: <i>Schematic of Laser Pulse Compressor</i>	54
Figure 2.11: <i>Relation between the laser pulse duration and the grating separation</i>	55
Figure 2.12: <i>(a) spectrum and (b) corresponding pulse duration after pulse compressor</i>	55
Figure 3.1: <i>A schematic diagram of a typical setup used for snap shot interferometry</i>	59
Figure 3.2: <i>Time separation between the main and probe pulses</i>	61
Figure 3.3: <i>Pump probe experiments with sub picosecond resolution</i>	63
Figure 3.4: <i>A schematic diagram of a typical setup used of three-frame shadowgraphy</i>	64
Figure 3.5: <i>Schematic diagram showing the experimental setup¹</i>	66
Figure 3.6: <i>Interferograms recorded for aluminium plasma; (a) in the absence of plasma, (b) with streak camera slit (dotted lines) parallel to plasma expansion direction (arrow), and (c) with slit perpendicular to plasma expansion direction.</i>	66
Figure 3.7: <i>Temporal variation of the electron density for aluminium plasma at two axial distances¹.</i>	67
Figure 3.8: <i>A schematic diagram of the setup used in chirped pulse reflectometry</i>	70

Figure 4.1: <i>A schematic diagram showing laser chirped pulse amplification</i>	75
Figure 4.2: <i>A schematic diagram of a Laser Pulse Stretcher</i>	75
Figure 4.3 : <i>A typical spectrum of the stretched laser pulse</i>	77
Figure 4.4 : <i>Setup to characterize the probe beam : (1) monochromator, (2) image rotator, (3) imaging lens, and (4) Streak camera with a CCD camera.</i>	77
Figure 4.5 : <i>(a) Calibration of the streak camera using fs heating and pico second probe pulses (b) additional 2cm path difference between fs and ps pulses</i>	78
Figure 4.6 : <i>Streaked image of the probe beam spectrum showing a liner chirp^a</i>	79
Figure 4.7 : <i>A Schematic of the experimental setup for the shadowgraphy and interferometry measurements^b</i>	80
Figure 4.8 : <i>A schematic diagram of a cyclic interferometer</i>	84
Figure 4.9 : <i>Shadowgram (spectral domain) of probe pulse in absence of plasma^a</i>	86
Figure 4.10 : <i>Shadowgram (spectral domain) of the probe pulse in presence of plasma^a</i>	88
Figure 4.11 : <i>Temporal variation of the plasma expansion^a</i>	89
Figure 4.12 : <i>Temporal variation of the plasma expansion velocity^a</i>	90
Figure 4.13: <i>Shadowgrams recorded at different laser intensities on the target</i>	91
Figure 4.14 : <i>(a) Temporal profiles of the plasma expansion velocity for different laser intensities and (b) the scaling between peak expansion velocity and laser intensity</i>	91
Figure 4.15 : <i>Interference fringes in the absence of plasma (reference)^b</i>	93
Figure 4.16 <i>Interference fringes at two different time delays^b</i>	94
Figure 4.17 : <i>Temporal profile of the density at two distances from the target surface^b</i>	96

Figure 4.18 : <i>The temporal profile of the expansion velocity. The circles/squares show experimental data from shadowgraphy and interferometry respectively</i>	97
Figure 4.19 <i>Time resolved interferometry with an optical streak camera (a) without and (b) with plasma</i> ^c	99
Figure 5.1: <i>A schematic of optical setup of the three channel polaro interferometer</i> ^l	105
Figure 5.2: <i>A photograph of the plasma chamber. Arrows show the polaro-interferometer mounted on the side ports</i>	109
Figure 5.3: <i>A schematic diagram of probe beam generation and propagation</i>	110
Figure 5.4: Three channel polaro-interferometer image recorded	113
Figure 5.5: <i>Magnified view of three channels at a probe delay of 3 ns a) Polarogram, b) Interferogram, and c) Shadowgram</i> ^l	114
Figure 5.6 : <i>Rotation angle contours at a probe delay of 3 ns</i>	115
Figure 5.7: <i>Radial profile of the electron density for a delay ~ 3ns</i>	117
Figure 5.8: <i>Spatial profiles of the self-generated magnetic field at a delay of 3ns.</i>	118
Figure 5.9 : <i>The electron density and magnetic fields in different laser shots for 3 ns delay</i>	120
Figure 5.10: Three channel images at probe delays a)1.6, b) 1.9 and c)2.7 ns	120
Figure 5.11 : <i>Rotation angle contour after a probe delay of 1.9ns</i>	121
Figure 6.1: <i>A schematic diagram of the chirped pulse shadowgraphy</i>	129
Figure:6.2 <i>Shadowgrams recorded with chirped probe pulse providing temporal evaluation of shock propagation in soda lime glass a) without and b) with shock wave propagation</i> ^l	131

Figure 6.3: <i>Variation of the shock velocity with time at $I_L \sim 1 \times 10^{14} \text{ W/cm}^2$</i> ¹	133
Figure 6.4: <i>Snap-shot shadowgrams a) without shock, b) with shock wave propagation</i> ¹ (schematic on left most side)	134
Figure 6.5: <i>Variation of the shock velocity with time at two laser intensities 4×10^{13} (blue) and 1×10^{14} (red) (The curves are only to guide the eyes.)</i> ¹	136
Figure 6.6: <i>Shock Hugoniot diagram in $\rho - P$ plane for a material undergoing phase transition and delayed compaction</i>	139
Figure 6.7: (a) <i>Shadowgram recorded showing jet-like structures after a delay of 2 ns (top left) (b) A reference shadowgram taken in absence of plasma (shock) (c, d) Time integrated shadowgrams with a He-Ne laser, much after the experiment (bottom left to right) (e) Shadowgram after 1 ns delay (f) Shadowgram showing diverging trend in the structure (g) Reference shadowgram taken in absence of plasma (shock).</i> ¹	142
Figure A.1: <i>A schematic depiction of space and time resolved information from a streak camera</i>	151
Figure A.2: <i>Temporal profile of the ramp voltage.</i>	153
Figure A.3: <i>Streak camera calibration Procedure</i>	155
Figure B.1: <i>A schematic diagram of chord integrated measurement</i> ^a	156
Figure C.1: <i>CCD picture showing the three simultaneously recorded channels : Polarogram (lower right), Interferogram (overlapping region of lower images), and shadowgram (top).</i> ^a	162
Figure C.2: <i>Selecting a enhanced region in Faraday channel.</i> ^a	162
Figure C.3: <i>A magnified view of interference fringes in which one fringe is tracked.</i> ^a	163

Figure C.4: *The fringe shift of a marked fringe and the electron density calculated.^a* 164

Figure C.5: *The experimentally measured Faraday rotation angle and the magnetic fields.^a* 166

LIST OF TABLES

Table 2.1: <i>Technical Specifications EKSPLA SL-223 Oscillator</i>	40
Table 2.2: <i>Technical specifications the Chameleon ULTRA II oscillator</i>	41
Table 2.3 : <i>Parameters of the 10 TW Ti:sapphire laser system.</i>	47
Table 6.1: <i>Experimental parameters for figures 6.7 a to g^l</i>	142
Table A.1: <i>Spectral ranges of different photo-cathodes</i>	149
Table A.2: <i>Technical specification of the streak camera</i>	152

Chapter 1 : Introduction to Laser Produced Plasmas

1.1 Introduction

The field of laser produced plasmas has attained its present momentum, starting with a novel suggestion made by Edward Teller and N. Basov about laser induced nuclear fusion as possible solution to the energy crisis of the modern world. This suggestion was made immediately after the demonstration of a laser by T. Maiman in Ruby crystal (694.3 nm)¹. In fact, this field was of such a strategic importance that it remained classified over the next few decades. The importance of the Inertial Confinement Fusion (ICF) can be understood from the fact that several megajoule laser facilities like National Ignition Facility (NIF), USA; Laser Mega Joule (LMJ), France; Laboratory for Laser Energetics (LLE), USA; Extreme Light Infrastructure (ELI), Europe etc. are pursuing this activity vigorously. With the introduction of techniques like *Q-switching* and *mode locking*, the focussed laser intensities crossed 10^{14-15} W/cm². The huge electric fields associated with these lasers are capable of fully ionizing any medium from which the plasma is formed. At these high temperatures, these plasmas become intense point x-ray sources. The small dimensions of the plasma coupled with strong emission in the x-ray range lead to many interesting applications like imaging of biological samples, stereoscopic imaging, lithography², imaging of dense plasmas³ using back-lighting etc. Similarly, the high power densities that are achieved in laser-plasma interactions enable the equations of state (EOS) studies of matter under extreme conditions. More recent advances in the *Chirped Pulse Amplification* (CPA)⁴ techniques have led to generation of ultra-short ultra-intense (USUI) femtosecond laser systems delivering powers of TW to a few PW. With laser intensities reaching 10^{16-22} W/cm², the relativistic laser plasma interaction regime is reached. This has opened up

several possibilities: table-top electron acceleration generating mono-energetic electron beams (few MeV - ~ 4 GeV)⁵ ; MeV energy protons/ ions which can find application in the area of oncology⁶; γ -rays, neutrons, which can cause nuclear reactions, high order harmonic generation leading to coherent radiation at wavelengths down to 2.7 nm⁷ etc. In addition, the interaction of these intense fs lasers with exotic targets like clusters, nano-particles, nano-tubes etc. have led to efficient laser absorption (80-90%) creating intense x-ray sources.

For all these applications, ranging from point x-ray sources to the exotic table top electron accelerators and table top x-ray lasers, the diagnostics of the plasma is very important. The small spatial dimensions of a few microns and extremely short duration (sub- μ s) of the laser produced plasmas demand a completely different set of diagnostic techniques with good spatial and temporal resolutions. Since the wavelength of the probing radiation puts an upper limit on the plasma densities that can be reached, probing with shorter wavelengths is preferred. Similarly, in order to study the dynamics of the laser plasma, one needs short duration probes. The optical probing of laser produced plasmas has provided both space and time resolved information. The research work described in this thesis is focused on developing such diagnostics for probing laser produced plasmas in the optical range. The present dissertation describes the results from our experiments using different diagnostic techniques like snap shot shadowgraphy, chirped pulse shadowgraphy, and chirped pulse interferometry. Chapter 1 gives a brief introduction to laser produced plasmas. The following sections deal with generation of plasmas, characteristics of these plasmas and different mechanisms of laser absorption in the plasmas. The physical aspects behind two main areas involving laser plasmas viz. generation of magnetic fields of several MG and high pressures of a few Gbar in different materials are briefly discussed, as experiments have been carried out in these two areas.

1.2 Generation of laser plasma

In order to create plasmas, powerful lasers are focussed on different materials (referred to as “targets”). The typical focal spots are \sim few microns (μm). With laser pulse duration in the ns - fs range, the focussed intensities easily exceed 10^{11} W/cm^2 . The electrical fields associated with the laser pulse go as $\sim(I)^{1/2}$, and are typically 10^{5-6} V/cm and more. In these conditions, the initial few electrons are created through processes like multi-photon ionization (MPI)⁸ provided that the laser wavelength is short enough and the irradiance is high enough. For example, considering the case of nitrogen gas at 1 atm., the threshold irradiance is $\sim 2 \times 10^{11} \text{ W/cm}^2$ for a laser pulse ($\tau = 30 \text{ ns}$) at $\lambda = 1.06 \mu\text{m}$. This implies MPI of nitrogen requires absorption of 12 photons. The presence of impurities with lower ionization potential eases this condition⁹. The multi photon absorption can be expressed as

$$n\eta\varpi_L > E_i > (n-1)\eta\varpi_L \quad \text{--- -- 1.1}$$

The MPI requires simultaneous absorption of n photons with total energy just exceeding the ionization energy of the bound electron E_i . Simultaneous absorption here means absorption within the lifetimes of the virtual states of electrons, which is typically in fs.

In the case of short duration laser pulses, the ionization can occur almost instantly through two different mechanisms. They are known as *tunnel ionization* (TI) and *barrier suppression ionization* (BSI)¹⁰. The laser electric field at intensities $> 10^{18} \text{ W/cm}^2$ approaches the Coulomb potential of the atom and significantly distorts the potential well. This leads to significant change in the height and width of the potential barrier the bound electron sees. With the reduced barrier height and width, the electrons have certain probability of tunnelling through the barrier leading to ionization. At still higher intensities $> 10^{18}$ this potential is fully suppressed

and electrons are free. The latter case is also known as *over the barrier ionization* (OBI). The threshold intensity for BSI is given by¹¹

$$I_{BSI} (W / cm^2) \approx 4 \times 10^9 E_i^4 (eV) Z^{-2} \quad \text{--- 1.2}$$

where Z is atomic number of the target, and E_i is the ionization energy. For intensities $> 10^{18}$ W/cm², gases like H₂, He are fully ionized and N₂, Ar are partly ionized in the initial part of the femtosecond laser pulse. Rest of the pulse interacts with this plasma.

Some general characteristics of the laser produced plasma will be discussed now. A brief discussion about different absorption processes will follow in Section 1.4.

1.3 Characteristics of Laser Plasmas

Once the laser produced plasma is generated, it will start expanding axially outwards due to steep density and temperature gradients forming a monotonically decreasing density profile as shown in the Fig. 1.1 below. In such an expanding plasma, the laser can propagate only up to a region

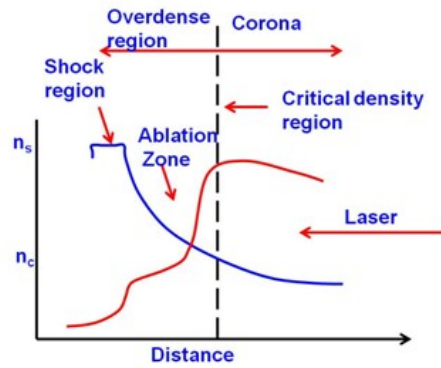


Figure 1.1: Spatial profile of the plasma density and temperature in long duration lasers

of plasma known as the critical density. The reasons for this are explained slightly later. Since the laser cannot propagate beyond this region, laser energy is coupled to the plasma upto the

critical density region through various absorption mechanisms described in Section 1.4. This energy is transferred to the colder solid density target region through the plasma. As significant laser energy is deposited at and before the critical density region, the plasma temperature peaks near the critical density region.

1.3.1 Plasma frequency and the critical density

If the electrons are displaced from their position, an electric field builds up between the electrons and background ions, pulling back the electrons to their original positions. However, due to their inertia, the electrons overshoot and move away from ions in the opposite direction. Thus electrons oscillate around their equilibrium positions. The frequency of these oscillations is known as *plasma frequency*. The plasma frequency ω_p is given by¹²

$$\omega_p^2 = n_e e^2 / \epsilon_0 m_e \quad \text{--- -- 1.3}$$

substituting the values of physical constants, this becomes

$$\omega_p \text{ (rad/s)} = 56.4 (n_e \text{ [/cm}^3\text{]})^{0.5} \quad \text{--- -- 1.4}$$

The plasma frequency decides the time-scale in which the electrons respond to the external perturbations. Any external field at lower frequencies will be shielded by electrons by responding to it. Thus the plasma frequency plays an important role in the propagation of electromagnetic waves in the plasma.

Once plasma is formed, the propagation of an electromagnetic wave in the plasma follows the dispersion relation¹³

$$\omega^2 = \omega_p^2 + k^2 c^2 \quad \text{--- -- 1.5}$$

As the plasma has density gradients, the plasma frequency will change in space, and the plasma will behave like a dielectric with varying refractive index given by

$$\mu = c/v_\phi = (1 - \omega_p^2/\omega^2)^{0.5} \quad \text{--- --- 1.6}$$

where v_ϕ is the phase velocity of the light. It can also be seen here that due to their higher mass, the natural oscillation frequency of ions is too low and one can treat the ions to be stationary compared to the laser frequency ω . This relation indicates that the laser light with frequency ω can propagate only up to a density region where $\omega > \omega_p$. Beyond this point the refractive index becomes imaginary and the laser light cannot propagate into the over dense region of the plasma. The region where both the frequencies are equal is called the *critical density* region. The value of the critical density is given by¹⁴

$$n_c = 1.1 \times 10^{21} (\lambda_L [\mu\text{m}])^{-2} \text{ cm}^{-3} \quad \text{--- --- 1.7}$$

In reality, even before the critical density region, the laser light undergoes strong refraction. This is the reason why the laser energy will be either reflected or absorbed only up to the critical density region. This is also the reason why a higher frequency (shorter wavelength) laser beam is used for probing the plasmas, as this will allow denser regions to be probed.

The region around the critical density region and away from the target is called the *corona* region. The corona consists of hot plasma formed initially from the solid target. The laser energy is absorbed in the corona region and the resulting thermal energy is transported towards the cold, high density region referred to as *over-dense* region. It is this over-dense region where the ablation occurs.

The temperature of the corona near the critical density is given by¹⁴

$$T_e(\text{keV}) \approx 0.6 [(1/f) (I_{\text{abs}}/10^{14} \text{ W/cm}^2) (\lambda_L / 1\mu\text{m})^2]^{2/3} \quad \text{--- --- 1.8}$$

where $f < 1$ is a flux inhibition factor. For laser plasma experiments at intensity 10^{14} W/cm^2 this expression gives temperatures of 6.4 keV for 1.06 μm and 0.9 keV for 0.25 μm assuming $f=0.03$.

In another experiment by Louzon et al.¹⁵ a plasma temperature of ~ 1.8 keV was estimated in the corona region of iron plasmas from spectroscopic measurements at a laser intensity of $\sim 10^{15}$ W/cm².

1.4 Absorption of laser light in Plasmas

Once the initial electrons are created through mechanisms like MPI, TI, or OBI (discussed earlier), the electrons interact with the electric fields of the lasers and transfer the energy to the background ions/neutrals through processes like *collisional absorption* (*Inverse Bremsstrahlung* (IB)), collisionless process of *resonance absorption* (RA) and *parametric decay* for further coupling of laser energy to the plasma. In the case of ultra-short fs pulses, processes like *vacuum/ Brunel heating* and *jxB heating* also play a prominent role in the energy coupling between the laser and the plasma. All these mechanisms are briefly discussed in subsequent sections. The duration of the laser pulse, its wavelength etc. will decide which of these processes will be the most dominating absorption process for coupling of the laser energy in different parameter regimes.

1.4.1 Inverse Bremsstrahlung absorption

Inverse Bremsstrahlung absorption is due to electron-ion collisions in the plasma. The plasma electrons oscillate back and forth in the transverse electric field associated with the laser pulse and then they undergo scattering collisions with the background ions^{12,17,18}. Through these collisions, their oscillating energy referred to as *quiver energy* is transferred to these ions. Thus, the laser light wave gets effectively damped.

In order to understand how the laser absorption depends upon the different plasma parameters like plasma electron density n_e and electron temperature T_e , consider the damping

rate ν_E of the electric field which can be equated with the damping of the kinetic energy of the oscillating electrons and can be expressed as^{12,14}

$$\nu_E (E_L^2/8\pi) = \nu_{ei} [(n_e/2) m_e (eE_L/m_e\omega_L)^2] \quad \text{--- -- 1.9}$$

Simplifying, one gets (using $\omega_p^2 = 4\pi e^2 n_e/m_e$)

$$\nu_E = (\omega_p^2/\omega_L^2) \nu_{ei} = (n_e/n_c) \nu_{ei} \quad \text{--- -- 1.10}$$

and using some more mathematics we get

$$\nu_E \propto (Zn_e/T_e^{3/2}) \quad \text{--- -- 1.11}$$

Thus, the damping rate of the electric field is directly proportional to the electron density and inversely proportional to temperature as $T_e^{3/2}$. The other important parameter, the spatial damping rate of the wave energy K_{IB} is twice the imaginary part of the wave vector k and is expressed as

$$K_{IB} = Zn_e^2 / T_e^{3/2} (1 - n_e / n_c)^{1/2} \quad \text{--- -- 1.12}$$

which means that in the case of colder and denser regions, the collision absorption is dominant. It can also be seen from equation 1.12 that inverse bremsstrahlung process is strong in high Z plasmas. In the case of nanosecond laser pulses, laser light absorption as high as upto 80% is observed¹⁶ at shorter wavelengths at $\sim 10^{13}$ W/cm². But for higher laser intensities this process becomes less effective as the collision frequency reduces at higher temperatures¹⁶. In the case of femtosecond laser plasmas, after the initial part of the laser has ionized the material, the rest of the laser pulse sees a steep density gradient(solid density plasma). Further, during the ultra short laser pulse, the IB process cannot grow. In this situation, other mechanisms like resonance absorption described below serve as the dominant mechanism of absorption.

1.4.2 Resonance absorption

In this process, the laser light which is obliquely incident on plasma with density gradient excites resonant plasma oscillations^{17,18,19} at critical density surface as shown in Fig. 1.2 when

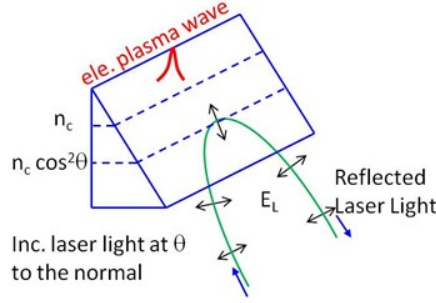


Figure 1.2: A schematic diagram of Resonance Absorption

these electrostatic plasma oscillations are damped either by collisions or by collisionless (Landau damping) process²⁰, energy is, in effect, transferred from the laser electric field to the plasma. It is seen that resonance absorption (RA) process persists when the classical collision frequency is small. So RA dominates over the IB absorption mechanism in plasmas with high temperature, longer wavelength (lower n_c), and short plasma scale-length. However, it may be noted that this process (RA) takes place only if the laser electric field has a component in the direction of the density gradient which results in the polarization dependence of absorption as shown in Fig. 1.2.

In Fig1.2, consider a laser beam incident at an angle θ with the density gradient (∇n_e). It gets reflected from the surface $n_e(\theta) = n_{cr} \cos^2 \theta$, according to the Snell's law. Here one can see that if the electric field of the incident laser light is in the plane formed by k and ∇n_e then at the turning point the component of the electric field will be in the direction of ∇n_e . Some of this *evanescent* field tunnels up to the critical density surface where it can resonantly drive electron plasma oscillations (Langmuir waves). It may be noted that this is possible only in the case of p -

polarized light. In the case of s -polarized light, as the electric field will be perpendicular to the plane of \mathbf{k} and ∇n_e , there will be no Langmuir wave excitation, and hence no resonance absorption.

Now let us examine how the RA varies with the angle of incidence. It can be seen that as θ varies, the turning point density $[n_e(\theta) = n_{cr} \cos^2 \theta]$ shifts towards lower density. Thus, for larger angles, the wave must tunnel a larger distance and thus the Langmuir wave is not driven efficiently. On the other hand, for at smaller angles, the component of E parallel to density gradient (∇n_e) will be small (for normal incidence this component vanishes). Hence, there exists an optimum angle for RA. The absorption (A) can be expressed quantitatively as¹⁴

$$A = (\omega_L L/c)^{1/3} \sin(\theta) \quad \text{--- -- 1.13}$$

for a plasma having linear density profile whose scale length is L . The peak in the absorption (around 60%) occurs at the intermediate angles of incidence for p -polarization at an angle given by the expression $\sin(\theta) \sim 0.8 (\omega_L L/c)^{-1/3}$.

For high laser intensities, e.g. $I_L \lambda^2 > 10^{15} \text{ (W/cm}^2\text{) } \mu\text{m}^2$, with the p -polarized laser and at optimum angle of incidence, absorption more than 50 % can occur through resonance absorption mechanism¹⁴. One important feature of the resonant absorption is the creation of *hot electrons*, where only a small fraction of plasma electrons acquire most of the absorbed energy. This is in contrast to collisional absorption (inverse bremsstrahlung), which heats bulk of plasma where a large number of electrons share the energy. The temperature of the hot electrons is given by¹⁴,

$$T_h (\text{keV}) = 13 (T_e^{1/4} / \text{keV}) [(I_L / 10^{15} \text{ W/cm}^2) (\lambda_L / 1.06 \mu\text{m})^2]^{0.39} \quad \text{--- -- 1.14}$$

where T_e is the temperature of the background electrons. The density fraction of the hot electrons is decided by the laser intensity.

1.4.3 Absorption due to ion-acoustic turbulence

In case the short-wavelength ion fluctuations present in the plasma are coherent, it is seen that the absorption of light in the plasma is enhanced. In the collisional absorption process, thermal distribution of electrons and randomly distributed ions are assumed. However, if these ions are exhibiting coherent nature in turbulence with a fluctuation spectrum $\delta n_i(\mathbf{k})/n_i$ then the energy damping rate of the laser light of frequency ω_L becomes¹⁴

$$(V_E)_{\text{eff}} = (\omega_L/2) \sum_k (\delta n_i(\mathbf{k})/n_e)^2 \text{Im}[1/\epsilon(\mathbf{k}, \omega_L)] (\mathbf{k} \cdot \mathbf{E}_L)^2 \quad \text{--- 1.15}$$

Here, the $\text{Im}[1/\epsilon(\mathbf{k}, \omega_L)]$ depends on the plasma density. For short-wavelength ion fluctuations with $k \sim (1/(2\lambda_{De}))$, the absorption between the plasma density regions $0.4 n_c$ and n_c can be substantial if the level of ion fluctuations $(\delta n_i(\mathbf{k})/n_e)$ is large enough. For pulse length < 100 ps, it is seen that for $n_e > n_c/3$ and $T_e > 5T_i$, the coherent ion turbulence can contribute up to 20% extra absorption¹⁴. This absorption due to ion turbulence would add to the fraction absorbed through RA, since these two processes enhance the absorption process in different regions of the plasma density profile. For long pulse duration, simulations indicated absorptions by ion-acoustic turbulence (>150 ps, $1.06 \mu\text{m}$) reached²¹ 54% at $7 \times 10^{14} \text{ W/cm}^2$. However, the hot electrons due to RA are hotter than ion turbulence electrons. The source for these coherent ion turbulence either heat-flow drive ion acoustic instabilities or ion-ion streaming instabilities.

1.4.4 Comparison between three absorption processes

As we have seen above, IB is due electron-ion collisions. It increases with target Z , with plasma density, and with length of the under-dense plasma, and decreases at higher plasma

temperatures.¹⁴ Resonance absorption by contrast, tends to dominate at higher intensities, and for short laser pulses. It is both angle and polarization dependent as it depends on the excitation of resonant electron plasma oscillations at the critical density surface. Theoretical absorption peaks at 50-60% for p- polarized laser. At higher intensities, when the critical density surface is steepened ($I_L \lambda_L^2 > 10^{15} \text{ W}\mu\text{m}^2/\text{cm}^2$), the resonance absorption creates a nearly Maxwellian tail of hot electrons and these electrons are ejected in the outward direction (in the direction of decreasing plasma density).

Enhanced ion-acoustic fluctuations can increase absorption by as much as 20%, especially for short pulse durations lasers.

1.4.5 Losses due to stimulated scattering

In competition with the absorption processes discussed in previous sections, *stimulated scattering processes* take away significant part of the laser energy reducing the fraction of absorbed energy. Like in RA, the electromagnetic wave can excite other modes of waves and transfer its energy. For example, in the *stimulated Brillouin scattering* (SBS), the laser wave decays into an ion acoustic wave and a back scattered light wave. The other process : *stimulated Raman scattering* (SRS) occurs when the laser energy is coupled to a plasma wave and a light wave. While the SRS occurs up to quarter critical density ($n_c/4$), the SBS can occur up to the critical density (n_c) and diverts significant fraction of laser energy. The problem with the SBS is that the backscattered light couples back to the laser system and can damage optical components if precautions were not taken. The third decay process is *Two plasmon decay* wherein the laser light gives it energy to two plasma waves.

1.5 Absorption processes with short (fs) laser pulses

In the case of ultra-short laser pulses (duration tens to hundreds of femtosecond), the initial fraction of laser pulse itself creates solid density plasma. As the pulse duration is small, the plasma expansion during this short time period will be very small. Rest of the laser interaction occurs with this plasma of steep density gradient. In this type of plasmas, the gradient scale length L is much smaller than the wavelength λ_L of the laser. The absorption occurs within a very small layer as the laser cannot propagate beyond the critical density region. Due to the steep density gradient, the laser energy absorption through inverse Bremsstrahlung (IB) process will be minimal. In this type of plasmas, other absorption processes like resonance absorption, vacuum/Brunel heating²² and $\mathbf{j} \times \mathbf{B}$ heating are the major absorption processes. The resonance absorption mechanism has been discussed previously. The other two processes: vacuum/Brunel heating and $\mathbf{j} \times \mathbf{B}$ heating are discussed below.

1.5.1 Vacuum/Brunel heating

In the plasmas with steep density gradients, Brunel had proposed that electrons from the under-dense plasma will be accelerated from the plasma-vacuum interface in the outward direction into vacuum during one half cycle of a electric field for an obliquely incident p-polarized laser pulse and pushed back into the target during the other half-cycle²². For this to happen, the quiver amplitude of an electron has to be greater than plasma density scale length i.e.,

$$(\nu_{osc} / \omega) > (\partial \ln n / \partial z)^{-1} \quad \text{--- -- 1.16}$$

This process is schematically illustrated in Fig. 1.3.

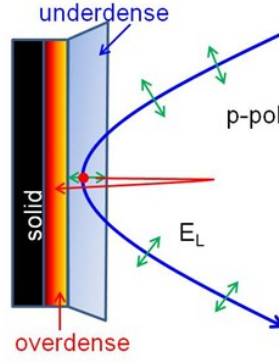


Figure 1.3: Brunel (Vacuum) absorption mechanism

During the other half cycle, the electron is accelerated in the reverse direction with a velocity $\sim v_{osc}$ and is pushed back into the plasma. It penetrates deep into the over-dense region of the plasma and loses its energy through collisions. The laser cannot penetrate beyond the skin depth $\sim c/\omega_p$, but efficient transfer of energy can occur through these electrons for a p-polarized light incident at large angles. This creates a fraction of fast electrons in every cycle.

1.5.2 $\mathbf{j} \times \mathbf{B}$ heating

At ultra-high intensities, the electron motion become relativistic and the $\mathbf{v} \times \mathbf{B}$ term^{23,24} in the Lorentz force becomes significant. The electrons are also accelerated by the magnetic field component and execute "Figure of 8" motion. At the ultra high intensities, the $\mathbf{v} \times \mathbf{B}$ term leads to acceleration of electrons in the propagation direction of the laser. Compared to the previous mechanism of acceleration in which p-polarization was preferred, the $\mathbf{j} \times \mathbf{B}$ acceleration is same for both s- or p- polarizations. When $v/c \sim 1$, the $\mathbf{v} \times \mathbf{B}$ term becomes comparable to the $q\mathbf{E}$ term. So with this longitudinal component, the electron can penetrate into the over-dense region and lose its energy. As this process is significant at very high intensities, it is not relevant for the experiments described in present thesis.

After this brief discussion about laser plasma interaction processes, two phenomena occurring in the laser produced plasmas and experimentally studied as part of this thesis are discussed below.

1.6 Self generated magnetic fields in laser produced plasmas

Laser produced plasmas are highly inhomogeneous in nature, exhibiting large density and temperature gradients. Absorption processes like resonance absorption, particularly at high laser intensities ($I\lambda^2 > 10^{14} \text{ W } \mu\text{m}^2/\text{cm}^2$) leads to generation of fast electrons. In the case of ultra short ultra intense laser pulses, production of high energy electron bunches are reported²⁵ by Baton *et al* . All these may constitute un-compensated electron currents leading to production of self-generated magnetic fields ranging from a few MG to several hundreds of MG as discussed below. Study of these magnetic fields is important as they may affect the processes of energy transport and laser plasma interaction in different ways.

Occurrence of self-generated magnetic fields was predicted using theoretical models and was also experimentally observed in many laboratories world-wide. Using Faraday rotation technique, Stamper *et al.* had measured magnetic fields of $\sim 2 \text{ MG}$ ⁸⁸ . This was followed by several studies of magnetic field measurements using different detection methods. By using higher order harmonics as probes, self-generated magnetic fields of order of $\sim 700 \text{ MG}$ had been predicted by Wagner *et al*³⁹. Najmudin *et al*²⁶ have reported detection of magnetic fields in excess of 7 MG in the interaction of a circularly polarized laser light in under-dense helium plasma at intensities upto 10^{19} W/cm^2 . They had attributed these fields due to the fast electrons spiralling around a channel created by the laser field. Thus these fields act as signatures for different processes occurring in the laser produced plasmas. In case of ultra-short ultra-intense

laser plasma interaction, generation of hot electrons jets, acceleration of electrons upto few GeV leave their stamp in the form of localized magnetic fields. The acceleration of sub-fs electron bunches by the laser pulses at relativistic intensities was shown by Popescu *et al* by measurements of harmonics of the laser light²⁵. Cecchetti *et al*²⁷ had measured large scale magnetic fields ~45 T in the outer coronal region using proton deflectometry technique. All these indicate the importance of studying self-generated magnetic fields in laser produced plasmas. A brief description of various mechanisms for generation of these magnetic fields is given in the following.

1.6.1 $\nabla n_e \times \nabla T_e$ mechanism

This is the most classical mechanism of production of toroidal magnetic fields in plasmas having strong temperature and density gradients. When plasma starts expanding, the electron pressure generates a charge separation electric field expressed as^{28,29,30}

$$en_e \mathbf{E} \sim \nabla p_e \quad \text{--- -- 1.17}$$

This leads to magnetic field in regions where the gradients of density and temperature are orthogonal.

$$\delta B / \delta t = -c \nabla \times \mathbf{E} \sim - (c/e) \nabla \ln n_e \times \nabla T_e \quad \text{--- -- 1.18}$$

In the case of laser plasma, the laser focal spot is finite. So the above phenomena results in magnetic fields, especially at the outer regions of the plasma, as shown in Figs. 1.4(a) and (b). The density gradients point towards the target surface (i.e. axial). The temperature gradients at the edge of the plasma are inwards (i.e. radial). This gives rise to toroidal (azimuthal) magnetic field.

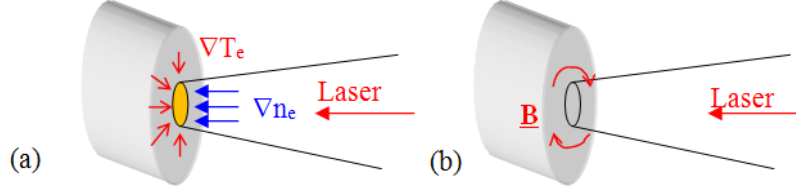


Figure 1.4: (a) Schematic of density and temperature gradients, and (b) generation of magnetic fields in laser plasmas

In the bulk of the plasma, the gradients in the temperature and density have no or small angle between them. This is because the intensity distribution of the incident laser is usually flat in the central portion leading to negligible temperature gradients in the radial direction. The magnetic fields at the centre of the focal spot will thus be quite low. The net result is generation of a toroidal magnetic field near the periphery of the laser spot.

The generated magnetic field can be expressed in terms of the temperature T_e , temperature scale lengths (L_T) as¹⁴

$$(B/10^6 \text{ gauss}) \cong (T_e / \text{keV})^{1/2} (1 \mu\text{m} / L_T) (A/Z)^{1/2} \quad \text{--- -- 1.19}$$

where A and Z represent the atomic mass and number respectively. For a plasma with 1 keV temperature and scale lengths of $20\mu\text{m}$ will have $B \sim 1.5 \text{ MG}$. This mechanism can also lead to generation of small scale magnetic fields if density and temperature gradients are present on

small spatial scales. Processes like filamentation and shock waves can produce such gradients resulting in generation of small scale magnetic fields.

1.6.2 Fountain Effect

In the case of plasmas with significant resonance absorption, as discussed earlier, there will be generation of hot electrons. These electrons move down the density gradient (i.e. in the axially outward direction). These hot electrons can lead to generation of magnetic fields^{31,32} at the boundary, as shown in Fig. 1.5. In the bulk of the plasma, any flow of hot electrons will result in a compensating current to flow in the opposite direction in the close-by region. But at the boundary of the plasma, such compensating current is absent and this leads to generation of magnetic fields.

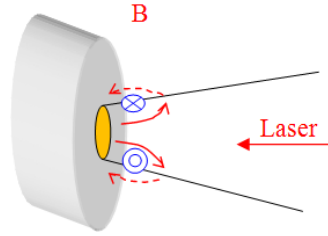


Figure 1.5: *Schematic of fountain effect in laser produced plasmas generating magnetic fields*

The fountain effect is important at higher intensities as the resonance absorption mechanism³³ will be the dominant energy transfer mechanism when laser duration is short and intensity is high.

1.6.3 Inverse Faraday Effect

Najmudin *et al*²⁶ had detected magnetic fields around 7 MG in the interaction of circularly polarized intense laser light with helium plasmas at intensities upto 10^{19} W/cm² in the

under-dense region. They have attributed these fields to the inverse Faraday effect²⁶. This is opposite to the Faraday (magneto-optical) effect. In the IFE, a circularly polarized light will induce axial magnetic fields in the presence of plasma. Ali *et al*³⁴ have shown that even with a linearly polarized light, the IFE mechanism can occur by considering both the spin and angular momenta of the laser pulse.

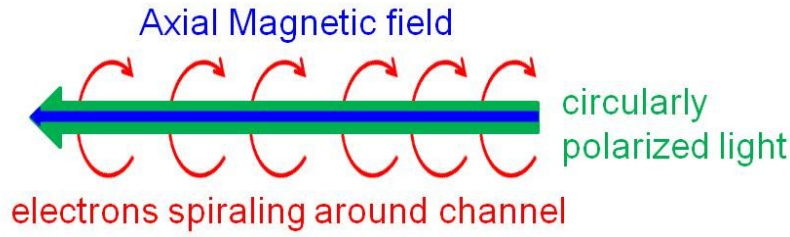


Figure 1.6: *Inverse Faraday effect with circularly polarized light.*

1.6.4 Weibel Instability

Another important source for generation of strong magnetic fields is the production of relativistic electron currents in both under dense and over dense regions of plasmas during interaction with Ultra Short Ultra Intense (USUI) laser pulses at intensities $>10^{18}$ W/cm². The source of these electron currents is a mechanism known as Weibel instability³⁵ as described below.

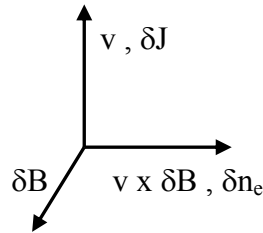


Figure 1.7: *Weibel instability*

Weibel instability occurs in a homogeneous or nearly homogeneous plasma where two counter propagating fluids are present resulting in momentum anisotropy (velocity v). The

anisotropy in momentum space and the resulting two stream instability occurs when the total current carried by the electrons inwards far exceeds the Alfvén limit (even after considering the return neutralizing currents). In this case, any perturbation (δB) in the form of an electromagnetic wave in the transverse direction will grow exponentially to reduce this anisotropy. The reason is as follows. The electrons will feel a $\mathbf{v} \times \delta \mathbf{B}$ force in the transverse direction (\perp to \mathbf{v} and $\delta \mathbf{B}$) and this leads to a perturbation in the electron density δn_e and in turn to a perturbation in the current δJ . Now via Maxwell's equation, this current perturbation δJ enhances the magnetic perturbation δB . This growth in the magnetic field results in division of propagating fluid into many filaments carrying current.

As said in the beginning, the magnetic fields are generated due to relativistic electron currents. Presence of pulsating channels (dia $\geq 5\mu\text{m}$, length $130\mu\text{m}$) of relativistic electrons with energy (1- 30 MeV) was experimentally observed by Borghesi et al³⁶. The numerical simulations using 3D-PIC code by Pukhov et al³⁷ under these experimental conditions also confirmed formation of relativistic electrons travelling along with the laser pulse and generation of multi mega Gauss magnetic fields which controlled the propagation of these electrons. These simulation studies were later extended into over dense regions (10 times critical density)³⁸. The laser light could propagate into over dense region due to the relativistically induced transparency, accelerate electron currents in the form of a bunch of current filaments transporting laser energy. This induces a return current from over dense region outwards. This leads to Weibel instability resulting in formation of filaments. The magnetic field associated with these current filaments leads to formation of a single strong filament along the laser axis. The presence of magnetic fields of order of 700 MG in the *over dense region* ($1 \times 10^{23} \text{ cm}^{-3}$) was experimentally detected

by Wagner et al³⁹ in intense laser interaction experiments with solid targets at $I_L \sim 10^{20}$ W/cm². It may be mentioned here that the generation of large magnetic fields in over dense region is important for the fast ignition fusion scheme in which a short duration intense laser pulse bores a hole through a surrounding over dense plasma region and ignites a compressed core at the centre.

1.7 Laser generated shock waves

There has been great scientific interest to study different materials under extreme pressures over the last few decades. Some of this research was aimed to understand different phenomena related to geophysical⁴⁰ and astrophysical sciences⁴¹. For example, one can represent the earth's internal structure or interiors of other planets better, after studying similar materials at extreme pressures in the laboratory. High pressure research also found many applications like material strengthening and hardening, electrical and optical phenomena (refractive index) at high pressures, high-stress structural designing and preparation of various synthetic materials like industrial grade diamonds at high pressures. Two major applications drawing a lot of attention in the high pressure research are related to inertial confinement fusion (ICF)⁴² and equation of state studies (EOS) for different materials at high pressures. In the ICF research, several laser beams are used to compress a fuel pellet symmetrically to extreme density and temperature conditions in order to achieve thermonuclear fusion reactions. In the EOS research, one would like to obtain accurate EOS data at higher pressures for different materials of interest.

Thus it can be seen that there is a wide-spread interest in generating high pressure conditions in the laboratory to study different phenomena. Depending upon the application, either static or dynamic pressures can be generated. These two approaches differ in many ways

like methods of pressure loading, attainable pressures, uniformity of the pressure over applied region, maximum sample size and the type of diagnostics one requires to measure the pressures generated etc. Thus it is the application that decides whether one will use dynamic or static approach. In general, static approaches provide uniform lower pressures and restricted to smaller samples. The dynamic approach can provide much higher pressures. The high pressure research has been mainly conducted using Diamond Anvil Cell (DAC)⁴³ for static pressures where as techniques like high velocity impacts using light-gas guns^{44,45} and explosive contacts provide dynamic pressures. The dynamic techniques like light-gas guns are limited to a few Mbar (Sandia 2-stage smooth bore LGG - 6.5 Mbar)⁴⁶ and for pressures > 10 Mbar one must employ either nuclear explosive devices or high-power lasers. Although nuclear explosive experiments generating shock pressures 400 - 4000 Mbar have been reported⁴⁷ due to security aspects and international ban, they are restricted to a few laboratories and rarely used now.

Under these conditions laser produced plasmas have become a valuable alternative to generate extremely high pressures upto a few Gbar⁴⁸ in the laboratory conditions. The laser generated shock waves have become an attractive option to conduct the high pressure research as a) one can reach much higher pressures on small spatial dimensions (hundred of μm to a few mm) and b) it makes possible to reproduce the extreme conditions of matter in a safe manner. As the temporal shape of the laser pulse can be changed, different strain-rate conditions can be realized in the laboratory. The availability of simpler diagnostic methods with high time resolution are an added advantage. The generation of shock waves using intense lasers as a method to generate high pressures is discussed below.

1.7.1 Mechanism of Shock Wave Generation

When a powerful laser beam is focussed on any solid material, the area in which the interaction is occurring can be divided into three distinct regions which include coronal region, ablation zone and shock compressed region. During the initial part of the laser pulse incident on the target, ionization occurs due to processes like multi photon ionization etc. forming an ionized low density gas cloud near the front surface of the target. As this expands outwards, the laser light can penetrate up to critical density where the laser frequency becomes equal to the local electron plasma frequency. The later part of the laser pulse interacts with the underdense plasma region upto the critical density (referred to as coronal plasma region) through absorption processes like inverse bremsstrahlung as explained in section 1.4. At higher laser intensities, significant part of the laser energy can be coupled to the plasma near the critical density surface through resonance absorption. The energy absorbed in the hot corona region upto the critical density surface is transported towards cold, dense interiors of the target. The region of energy transport is known as ablation region. A large temperature gradient exists in this region resulting in large heat flux from the critical density surface to the target surface. The heat transport is mainly due to electron thermal conduction as the ions are massive and slow to move. The actual electron flux estimated from the experimental results at higher laser intensities was much lower compared to the theoretical values. This led to introduction of many empirical flux limiting factors⁴⁹(f).

The inward heat flux results in continuous ablation (vaporization) of the fresh target surface. The ablated material expands outwards at high speeds up to 10^7 cm/s. This process generates a pressure at the ablation surface (ablation pressure) and due to recoil effect (Rocket blow-off model) this leads to a compression wave being launched in the target over the area of

laser irradiation. The large outward momentum flux associated with the rapid expansion of ablated material gives rise to a pressure which in turn drives a compression wave in rest of the target. The ablation pressure and the ablation velocity increase with increasing laser intensity. The dependence of ablation pressure on the laser intensity may be visualized as follows. If we assume a fraction (E') of the incident laser energy is coupled to the kinetic energy of the plasma expanding with velocity v ,

$$E' = \frac{1}{2} m v^2 \quad \text{--- -- 1.20}$$

the mass m of the material being ejected out per unit area ' A ', per unit time ' t ' can be expressed in terms of the mass density ρ as

$$m/At = \rho v \quad \text{--- -- 1.21}$$

Multiplying these two equations (1.20 and 1.21), the expansion velocity can be expressed in terms of the absorbed laser intensity I' as

$$v = (2 I' / \rho)^{1/3} \quad \text{--- -- 1.22}$$

Once again from 1.21 and 1.22, the pressure generated at the target surface due to the outwardly expanding plasma can be expressed as

$$P = \rho^{1/3} (2 I')^{2/3} \quad \text{--- -- 1.23}$$

It can be seen that the ablation velocity and ablation pressure have a dependence of $I'^{1/3}$ and $I'^{2/3}$ respectively. If we assume that all the laser energy is absorbed near the critical density only, the pressure can be expressed as⁵⁰

$$P = \left[(2\pi\epsilon)^2 \frac{m_p m_e \epsilon_o}{Z^* e^2} \right]^{1/3} \left[\frac{2 I'}{\lambda} \right]^{2/3} \quad \text{--- -- 1.24}$$

where m_p , m_e , ϵ_o , Z^* , e , I' and λ stand for the proton mass, electron mass, permittivity of free space, fractional ionization state of the target material, electron charge, absorbed laser intensity

and wavelength of the incident laser respectively. It may be noted from equation 1.24 the ablation pressure is higher in plasma produced by short wavelength lasers. ($\lambda^{-2/3}$ dependence).

1.7.2 Scaling of shock pressure with laser intensity and wavelength

Many empirical and theoretical models had been proposed as the experimentally measured ablation pressure at different laser intensities were not matching with predicated values of rocket blow off model (1.24). Max⁵¹ had reported the dependence of ablation pressure on the laser intensity for a flux limiting factor of $f \sim 0.03$, in terms of the atomic number Z , mass number A , laser intensity I (W/cm^2) and the laser wavelength λ (in μm) as

$$P_a [\text{Mbar}] \approx 7.2 \left[\left(\frac{I}{10^{14}} \right)^{0.57} \left(\frac{1\mu\text{m}}{\lambda} \right)^{0.99} \left(\frac{ZR_a}{0.1\text{cm}} \right)^{0.07} \right] \quad \text{--- -- 1.25}$$

which was modified by Lindl in 1995 as⁵²

$$P [\text{Mbar}] \approx 8.6 \left[\left(\frac{I}{10^{14}} \right)^{2/3} \left(\frac{1\mu\text{m}}{\lambda} \right)^{2/3} \left(\frac{A}{2Z} \right)^{1/3} \right] \quad \text{--- -- 1.26}$$

where I is the laser intensity on target in W/cm^2 , λ is the laser wavelength in μm , and A and Z are the mass number and atomic number of the target material. These expressions assume that all the laser light is absorbed near the critical density region (localized absorption). They showed a positive scaling exponent of ablation pressure with laser intensity and negative exponent with laser wavelength. Somewhat different expression of ablation pressure is obtained if one considers the movement of critical density surface with time. This in turn leads to a reduction in the energy transport up to the ablation front. Considering this movement of the critical density and the effect of ionization state of material Z^* , Mora theoretically derived the expression for ablation pressure as⁵³

$$P[\text{Mbar}] \approx 11.6 \left[\left(\frac{I(\text{W/cm}^2)}{10^{14}} \right)^{3/4} \left(\frac{1}{\lambda \mu\text{m}} \right)^{1/4} \left(\frac{A}{2Z} \right)^{7/16} \left(\frac{3.5}{Z^* t} \right)^{1/8} \right] \text{ --- --- 1.27}$$

In addition, there are other empirical relations by Henis⁵⁴, Eliezer⁵⁵ etc., The main difference between the expression by Max, Lindl with the one by Mora is whether the laser energy is absorbed locally or distributed. The plasma corona size will increase with time due to outward expansion and this will lead to an increase in separation between the absorption region and the target surface⁵⁶. Thus the absorption is no more localized and leads to a reduction in the mass absorption rate with time as considered by Mora. This effect could be seen in ablation pressure scaling measurements by Batani *et al.*⁵⁶ at shorter wavelength (0.44 μm) for laser intensities up to $2 \times 10^{14} \text{ W/cm}^2$. Their intensity scaling measurements are more close to expressions given by Mora's as compared to Lindl's expression. These results led to a scaling law in terms of the laser and target parameters expressed for case of Aluminum (A=27 and Z=Z*=13) as

$$P[\text{Mbar}] \approx 15.36 \left[\left(\frac{I(\text{W/cm}^2)}{10^{14}} \right)^{4/5} \left(\frac{1}{\lambda \mu\text{m}} \right)^{4/15} \left(\frac{1}{\rho_o (g/cm^3)} \right)^{1/15} \left(\frac{1}{d(\mu\text{m})} \right)^{2/15} \right] \text{ --- --- 1.28}$$

Here ρ_o is the mass density and d is the average thickness of base and step. As an example in an aluminium plasma heated at $1 \times 10^{14} \text{ W/cm}^2$ of $1 \mu\text{m}$ laser with $d = 8.25 \mu\text{m}$. the ablation pressure is estimated to be $\sim 12 \text{ Mbar}$. The intensity scaling of ablation pressure estimated using different models for an aluminum foil of $10 \mu\text{m}$ thickness is shown in the figure 1.8.

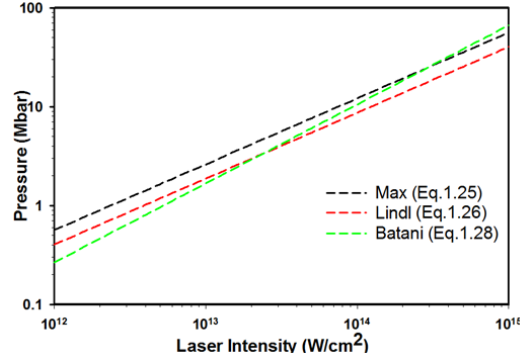


Figure 1.8: *Scaling of shock pressure with laser intensity*

From all these expressions (eq. 1.24 to 1.28) it is evident that ablation pressure increases as the wavelength of the laser light decreases. In other words, to produce identical ablation pressures one requires a laser of higher laser intensity at longer wavelengths. In general shorter wavelengths are preferred to improve the laser plasma coupling, ablation pressures and also the hydrodynamic efficiencies.

1.7.3. Shock Wave Propagation: Material Response

In order to understand the dynamics of shock wave propagation let us take a simple and ideal case in which uniform pressure is suddenly applied across the surface of a material and held constant thereafter (step pulse). The launching of shock wave is the initial response of the material to sudden change in the applied pressure or particle velocity at the boundary⁵⁷. An illustration of ideal shock transition in the material is shown in Figure 1.9 below. The shock front S is a region across which material properties like density, temperature, and pressure change rapidly in a discontinuous manner.

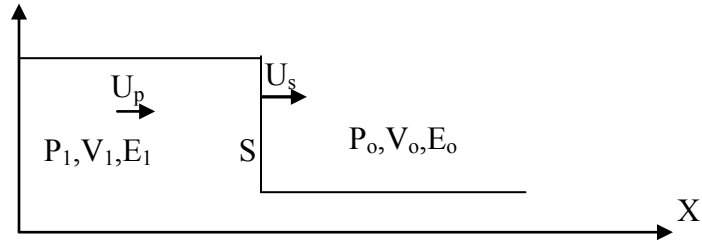


Figure 1.9 Shock wave propagation due to application of pressure at $x=0, t=0$

The thermodynamic state on either side of the steady state shock front are related through Rankine - Hugoniot equations⁵⁸ expressed below.

$$\rho_0 U_s = \rho_1 (U_s - U_p) \quad \text{--- -- 1.29}$$

$$P_1 - P_0 = \rho_0 U_s U_p \quad \text{--- -- 1.30}$$

$$E_1 - E_0 = 0.5 (P_1 + P_0) (1/\rho_0 - 1/\rho_1) \quad \text{--- -- 1.31}$$

combining equations 1.29 and 1.30 one can also express

$$U_s = [(P_1 - P_0) / (V_0 - V_1)]^{1/2} V_0 \quad \text{--- -- 1.32}$$

$$U_p = [(P_1 - P_0) / (V_0 - V_1)]^{1/2} \quad \text{--- -- 1.33}$$

Here $\rho_0, P_0, E_0, \rho_1, P_1, E_1$ are the mass density($1/V$), pressure and internal energy of the material before and after passage of the shock wave respectively. U_s, U_p are the shock and particle velocities. These expressions are based on the conservation laws of mass, momentum, and energy, before and after the passage of the shock wave. As the initial conditions ρ_0, P_0, E_0 are known, there are five unknown variables $\rho_1, P_1, E_1, U_s, U_p$ related through these three equations (1.29-1.31). This is a case of underdetermined system with two free parameters. In order to calculate the exact values of these parameters, one needs to simultaneously measure two shock parameters (usually U_s and U_p) experimentally. The locus of all the points reached by using a single shock is called shock adiabat, the Rankine - Hugoniot curve or simply the Hugoniot. The

Hugoniot can be in the form of U_s vs U_p or P vs U_s so on. A typical Hugoniot is shown in figure 1.10 below showing the initial and final states. The dotted straight line connecting the initial and final states is known as Rayleigh line with slope proportional to U_s^2 as given in equation 1.32.

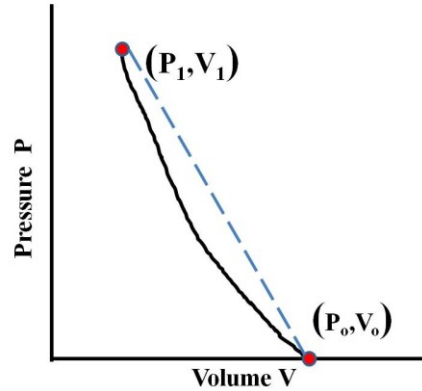


Figure 1.10: *Hugoniot for a material*

The simple treatment given above describes shock propagation in gases and in ideal liquids (zero viscosity). The treatment will also satisfactorily describe strong shock wave propagation in solids where material strength effects can be neglected and the material behaves like a hydrostatically compressed fluid. But at lower shock pressures we have to consider the material strength effects. In this regime, shock wave propagation becomes complicated because relations between the applied pressure and material response are non linear. Beyond a pressure the material loses its elastic property and tends to permanent deformation known as plastic deformation. The pressure at which the elastic failure occurs during shock wave propagation is called as Hugoniot Elastic Limit (HEL). In addition, it is also known that many materials undergo pressure induced phase transitions. Above these pressures, the phase of the material changes and the behaviour can no more be described by a simple Hugoniot as shown in the previous figure. A typical Hugoniot showing either elastic - plastic deformation or a phase transformation is shown in the figure 1.11 below.

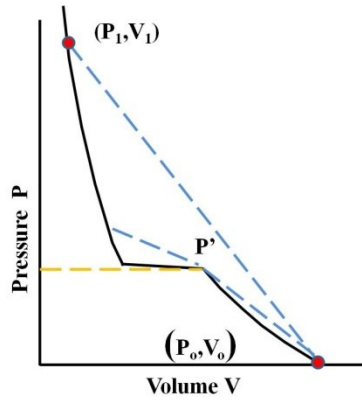


Figure 1.11: *Hugoniot of a material with an elastic-plastic flow or phase transition*

In any solid material, the application of pressure in a limited region leads to two components of stress in forward and lateral directions. As the pressure increases the difference between the two components results in generation of a shear stress. When the pressure crosses the HEL, this difference leads to a partial shear failure due to finite strength of the material. This failure is represented by a kink in the Hugoniot curve shown at P' in the figure above. At much higher pressures these effects become less significant and the material responds like a hydrostatically compressed fluid.

Other than elastic-plastic failures, some materials can also show phase transformation from one structural form to another while they undergo compression due to an increase in the applied pressure. Such a phase transition involves a change in the internal arrangement of the solid and thus leads to a large change in the density and entropy. In Fig. 1.11 at pressures smaller than P' , the shocked material remains in one phase, represented by the concave shape of the Hugoniot below P' . At transition pressure P' the material undergoes structural changes into another phase represented by a sudden change in the slope and *sudden* reduction in the volume. At higher pressures, the Hugoniot is represented by the second phase. A material can exhibit more than one

such phase transitions, each represented by a sudden change in the slope of the Hugoniot at those pressures.

The phase transitions occurring in any material can be classified in different ways. Ehrenfest had labelled the transitions by the lowest derivative of the free energy that is discontinuous around the transition⁵⁹. First order transitions have discontinuity in the first derivative of the free energy with respect to some thermodynamic variable. The solid/liquid/gas transitions are generally first order transitions as they lead to a sudden change in the density (or volume) which can be expressed as inverse of first derivative of Gibbs free energy with change in pressure ($V = \delta G / \delta P|_T$). For example the water undergoes first order transitions from ice-water and then water-vapour phases. Second order phase transitions are continuous in the first derivative but exhibit discontinuity in a second derivative of the free energy. An example of a second order phase transition is ferromagnetic phase transition occurring in iron in which the magnetization varies continuously but the magnetic susceptibility is discontinuous. One can also have higher order phase transitions. Another type of classification is based on whether the transition are with latent heat or without latent heat. The latent heat is absorbed or emitted by the system without increasing its temperature. This classification whether the transition is of order first or second depends on the discontinuity of the derivatives of the thermodynamic potential (with nonzero or zero latent heat respectively)⁶⁰.

The detection mechanisms for the presence of these phase transitions depend on the shock loading methods. In case of static pressures, diagnostics techniques like X-ray diffraction can be used in crystalline samples⁶¹. In case of amorphous material like soda-lime glass, changes in the micro Raman scattered signals had been used to study the densification process⁶². On the other hand, most of the techniques to detect elastic-plastic flows or phase transitions under

shock wave loading depend on measuring the shock and particle velocities. Depending on the time scales of shock loading these measurements can introduce large errors in the estimates. In the conventional shock loading techniques like contact explosives, accelerated flyer plates and projectile impacts, the typically shock arrival times are to be determined with a few ns resolution. Techniques like electrically charged pins, flash gaps, and optical time of arrival help in making discrete measurements. This kind of discrete measurements are sufficient for a single shock but for shock waves with multiple shock fronts, continuous time resolved measurements using quartz gauges⁶³, Velocity Interferometer System for Any Reflector (VISAR)⁶⁴ etc., are used. Real time x-ray diffraction technique has been used to detect changes below and above the phase transition stress in shock loaded KCl along [100] plane by Almeida et al.⁶⁵ in their impact plate experiments.

In case of laser generated shock waves, time resolutions of sub-nanosecond and lower are required. Techniques like time resolved x-ray diffraction (TXRD), laser shadowgraphy with short duration laser pulses, chirped pulse shadowgraphy, optical streak cameras⁶⁶ and VISAR are used for this purposes. Using TXRD technique, Loveridge-Smith et al⁶⁷ have detected a prompt transition to plastic flow in a single crystal Cu, shocked along the [200] axis. They had used quasi-blackbody XUV radiation from a hohlraum cavity to drive the shockwave and an x-ray streak camera to record the diffracted x-rays. Using pump probe technique, Gleason et al.⁶⁸ had recorded a transition from amorphous fused silica phase to crystalline high pressure stishovite phase. In the case of transparent glass materials, one can use time resolved optical diagnostics techniques like optical shadowgraphy, VISAR etc., to study the shock wave propagation by measuring the shock wave velocity. We have used optical shadowgraphy to

measure the shock wave velocities in soda lime glass at different instances with respect to the peak of the laser pulse and the results are discussed in chapter 6.

1.7.4 Shock Wave Propagation : Effect of Laser Pulse

The laser pulses may have different temporal profiles like Gaussian, trapezoidal, triangular etc. All these have a rising portion, then reach a peak value, may have a finite flat top, and then have a falling portion. As the shock wave velocity has a sub-linear dependence on the laser intensity, the ablation pressure can launch only an elastic wave at early times, as the laser intensity is relatively weak. During the rising part of the laser pulse, the ablation pressure will increase resulting in further compression of the material behind the wave front with increasing laser intensity, thus increasing the shock wave velocity with time. This means that although the shock wave components generated at different times with slowly increasing velocity will start their journey separately, the faster components started later in time will ultimately catch up with the earlier components to form a single strong shock known as *shock front* which is so steep that it is almost discontinuous. This process is known as shock wave *coalescence*⁶⁹ as shown in the Fig. 1.12.

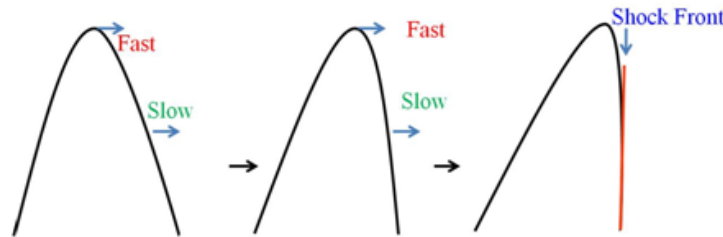


Figure 1.12: Shock wave coalescence forming a shock front

After the peak of the laser pulse, the amplitude of the shock wave at the front surface starts falling with time. This can be viewed as a relaxation (or rarefaction) wave is propagating in

from laser irradiated side to the backside of the target. As the material behind the shock wave is already compressed, effective velocity of the rarefaction wave far exceeds the shock wave preceding it. So sometime later, this rarefaction wave will reach and weaken the shock wave amplitude.

1.8 Conclusion

A brief introduction to laser produced plasmas is given. The initial plasma formation is due to processes like multi-photon ionization in the case of long duration laser pulses, and tunnel ionization and over the barrier ionization in the case of ultra-short laser pulses. After the initial ionization, different absorption mechanisms occurring in the corona region of the plasma transfer the laser energy towards colder denser region for further ablation. These mechanisms have been discussed for long pulse as well as ultra-short pulse regimes. Two main areas of laser plasma viz. self generated magnetic fields, and generation of high dynamic pressures in different materials are also briefly discussed, as two experimental investigations reported in the thesis have been carried out in these areas.

Chapter 2 : Lasers for Plasma Experiments

2.1 Introduction

The experimental work reported in this thesis has been mainly carried out using two different types of laser systems. The first one belongs to Master Oscillator Power Amplifier (MOPA) type of laser systems delivering laser pulses of nanosecond duration^{70,71,72}. This is an indigenously developed high power Nd:glass laser system. In a MOPA type laser system, a clean pulse from an oscillator is passed through : 1) a set of image relay systems to expand the beam and relay it up to the next amplifier stage, 2) Power amplifiers with gradually increasing cross section at each stage, and 3) Faraday isolators to block the reflected component. Some of image relay systems also act as spatial filters to remove any hot spots in the laser beam profile. The RRCAT high power laser system has two commercial oscillators a) a SBS pulse compression system (EKSPLA, Lithuania) that can deliver laser pulses of ~20 mJ of energy with pulse duration variable from 500 ps to 1500 ps, and b) a tunable wavelength femtosecond Ti-sapphire laser oscillator (Chameleon Ultra II, Coherent Inc., USA) delivering 140 fs, nJ laser pulses at repetition rate of 76 MHz. These femtosecond laser pulses are for further amplification using optical parametric chirped pulse amplification (OPCPA) scheme and then using existing conventional Nd:glass MOPA type of amplifiers to produce a 50-TW 25-J 500-fs pulse at 1053 nm. Details about the high power laser system are covered in Section 2.2.

The second type of laser system used for experiments belongs to a class known as Ultra Short Ultra Intense (USUI) table top 10 TW Ti:sapphire laser system (Thales Optronique, France) delivering laser pulses of 45 fs pulse duration, with energy ~ 450 mJ, at 800 nm, with maximum 10 Hz repetition rate. This system consists of a mirror-dispersion controlled Ti:sapphire oscillator (20 fs) coupled to an amplifier system at 10 Hz repetition rate to amplify ultra-short pulses based on chirped pulsed amplification (CPA) scheme⁴. It employs an Offner type all reflective pulse stretcher⁷³ for temporally stretching the 20 fs laser pulse to 200 ps duration, amplify it, and use a evacuated pulse compressor system to compress the stretched pulse back to 45 fs duration. Details about the 10 TW, 45 fs laser system are covered in Section 2.3.

2.2 High Power Laser System

The high energy, high power (HEHP) laser systems based on Master Oscillator Power Amplifier scheme are widely used for laser plasma studies viz. equation of state, inertial confinement fusion (ICF), and generation of intense thermal x-ray radiation etc. Even after the arrival of ultra-short, ultra-intense (USUI) femtosecond laser systems delivering powers beyond several petawatts, the importance of long pulse lasers has not diminished. This can be seen from the fact that world-wide many laboratories are vigorously pursuing several multi-kilojoule to megajoule projects for laser plasma interaction studies. National Ignition Facility (NIF) is a large laser-based inertial confinement fusion research facility, located at the Lawrence Livermore National Laboratory at Livermore, California, to conduct ignition experiments on fuel pellets at 500 TW of power, with its 192 beams.

As mentioned earlier, in MOPA architecture^{70,71,72}, a laser pulse from the master oscillator is amplified in a chain of power amplifiers. It is important to get a clean laser pulse of desired temporal profile with a TEM₀₀ mode. As the energy of the laser pulse increases after each amplifier, the cross-section of the beam has to be increased to keep the laser intensity within safe limits to avoid damage to the optical components. The oscillator pulse with a typical pulse duration of sub-ns to few ns is amplified using these amplifiers to several hundreds of joules to few kJ. In general, Nd:phosphate glass is used as a laser amplifier medium due to its small value of nonlinear refractive index and higher cross-section of stimulated emission coefficient. The details about the high power laser system at Laser Plasma Division, RRCAT are given here. A photograph of the system^{71,74}, is shown in Fig. 2.1.



Figure 2.1: *A photograph of the two beam high power laser system at RRCAT*

The schematic diagram of the two arm high power laser system at Laser Plasma Division, RRCAT is shown in Fig. 2.2. This system can deliver ~ 200 J per arm, in a pulse of

~1.5 ns. in one of the arms (Arm-A). The other arm (B) is for amplifying a chirped laser beam of 650 ns for the higher peak power experiments at 40 TW.

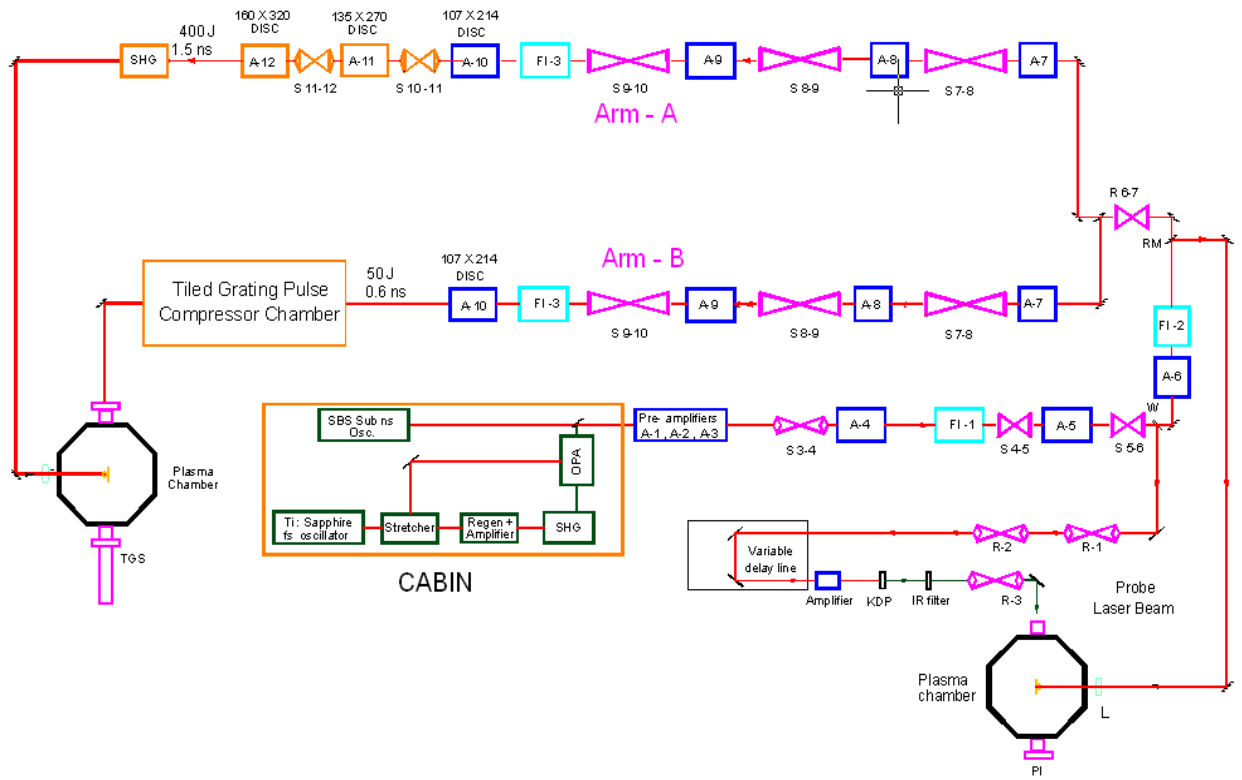


Figure 2.2: A schematic diagram of the two arm high power laser chain at RRCAT

There are two oscillators coupled to this laser system. The first oscillator is SBS pulse compression oscillator (SL223, EKSPLA) providing laser pulses with a duration selectable between 500 ps - 1500 ps and a TEM₀₀ mode with a typical energy of ~20 mJ and a contrast factor of $\sim 1:10^5$. The other oscillator (Chameleon, Coherent Inc.) belongs to a different configuration. This oscillator provides ~140 fs duration pulses at a tunable wavelength. For this system, the wavelength is set at 1054 nm. The fs laser pulses are temporally stretched to 650 ps using a diffraction grating based pulse stretcher and amplified first in a regenerative amplifier

and then finally using the high power laser system. The output from any one of these two oscillators can be coupled to the high power laser system for further amplification. Details about these two oscillators and other important systems follows here.

2.2.1 Oscillator 1 : SL-223

This oscillator consists of a master oscillator, a pre-amplifier, and an amplifier. This is a diode pumped solid state active Q-switched laser providing output at 1053 nm. The master oscillator is pumped by a diode laser through an optical fibre. The active Q-switching is done through a 2-stage Pockels cell. Fabry Perrot etalon is used to control the longitudinal mode selection along with a section of the Q-switch and a photo-diode providing negative feedback.

The output from the master oscillator is amplified in a double pass pre-amplifier consisting of an Nd:YLF rod pumped by a flash lamp. This pre-amplification stage also consists of a pulse compressor. The pulse compressor works on a pulse compression mechanism based on the stimulated Brillouin scattering (SBS). It consists of two lenses, a quarter wave retardation plate ($\lambda/4$) and SBS cell filled with CCl_4 liquid and a polarizer. By adjusting the position of the lens, the duration of the compressed pulse can be varied. A Faraday isolator kept between the oscillator and the pre-amplifier, blocks the reflected light to protect the oscillator. The output of the pre-amp is boosted up by another amplifier and then directed towards the high power laser system.

No	Parameter	Value
1)	Model (Ekspla laser)	SL223
2)	Max Pulse Energy at 1053 nm	20 mJ ($\pm 4\%$)
3)	Pulse Duration	500-1500 ps
4)	Repetition Rate	0.25 Hz
5)	Medium	Nd:YLF
6)	Beam Profile	Close to Gaussian
7)	Beam Divergence	< 1 mrad
8)	Contrast ratio	$10^5:1$
9)	Optical pulse Jitter	0.5 ns (int sync) ; 1 ns (ext sync)
10)	Polarization Ratio	$>100:1$
11)	Beam Diameter	4 mm

Table 2.1: *Technical Specifications EKSPLA SL-223 Oscillator*

2.2.2 Oscillator 2 : Chameleon Ultra II

The Chameleon Ultra II is a widely tunable, mode locked Ti:sapphire laser oscillator delivering 140 fs laser pulses with a repetitions rate of ~ 80 MHz. The output wavelength is tunable from 680- 1080 nm. The detailed specifications of this laser are given in Table 2.2. The system has an on-board spectrograph with simple USB interface which displays the laser wavelength.

No	Parameter	Value
1	Model	Chameleon Ultra II (Coherent)
2	Output peak power	> 3.3W
3	Wavelength tuning range	400 nm (680nm to 1080 nm)
4	Power in the tuning range	0.6 W @ 680 nm; 1.5 W @ 700 nm; 3.3 W @ 800 nm; 1.5 W @ 920 nm; 0.5 W @ 1020 nm; 0.2 W @ 1080 nm
5	Pulse Width	140 fs
6	Output Power Stability	< ± 0.5 (%)
7	Spatial Mode	TEM ₀₀ ($M^2 < 1.1$)
8	Pulse Repetition Rate	80 MHz
9	Polarization (Horiz. contrast)	> 500:1
10	Beam Diameter	1.2 \pm 0.2 mm
11	Beam Ellipticity	0.9 to 1.1
12	Astigmatism	< 10%
13	Pointing	< 0.5 (μ rad/nm)
14	Noise	< 0.15(%)

Table 2.2: *Technical specifications the Chameleon ULTRA II oscillator*

The main laser system has three pre-amplifiers (A1 to A3) of small diameters, seven laser glass rod amplifiers (A4 to A10), and three disc amplifiers (A-11 to A-13)⁷⁴. In the experiments reported in the present thesis, the laser beam only up to the amplifier A6 was used. The probe beam was generated by splitting a portion of the laser beam after A5. The laser system has a set of image relay cum spatial filters and Faraday isolators, as described below.

2.2.3 Image Relays / Spatial relays

In order to relay the laser beam from one amplifier stage to the next stage, Image Relays (IR) are used. They also act as beam expanders to increase the beam size as required by the next amplifier stage. There are two types of optical schemes for expanding the size of a beam. A Galilean type of beam expander (using one convex and another concave lens, with separation

equal to the *difference* of their focal lengths) is used after the SL223 oscillator. Rest of the beam expanders after the amplifier A2 onwards, are Keplerian type (in which both lenses are convex, with separation equal to the *sum* of their focal lengths). Similar image relays were used in the probe beam path as well. These are designed for relaying a plane at the input amplifier rod (mid-point) to the next amplifier rod (mid-point). The image relay system is designed such that

$$f_1 + f_2 = m \cdot D_1 + (D_2 / m) \quad \text{.....2.1}$$

Here, m is magnification, f_1 , f_2 are the focal lengths of object, image lenses respectively, D_1 is the distance between object-plane to the first lens and D_2 is a distance from second lens to the image plane. The lenses in each image relay stage are matched with requirements of the magnification required there. These beam expanders are in rotary vacuum condition (10^{-2} mbar) to avoid breakdown of the surrounding air which results in degradation of the laser quality.

The spatial non-uniformities present in the laser beam are amplified as at each stage of amplification. As they are amplified, two kinds of problems arise : 1) The small-scale ripples amplified beyond a intensity limit will lead to self-focussing of the laser beam, damaging the optical materials, and 2) On focussing, these will lead to large focal spots. Some of the image relay systems are designed to act as spatial filters, by placing a small pin-hole aperture at the common focal plane of the two image relay lenses. A spatial filter is always designed to allow only lower order spatial frequencies (i.e. Intensity variations in the beam profile) to pass through (low pass filter). The fine ripples in the spatial profile of the laser beam correspond to higher spatial frequencies and they get filtered out by the aperture (as they get focussed away from the axis). The size of the aperture decides the range of the frequencies being transmitted. This aperture is normally placed on a 3-axis translational stage to optimize the transmission and keep

it at the focal plane. The radial distance where a spatial frequency f_x will be focussed is expressed as

$$X_f = \lambda * f * f_x \quad \dots\dots\dots 2.2$$

where X_f is the radial distance from centre where it will be focussed (for order $m = 1$), and λ, f, f_x are the wavelength of laser, focal length of the lens and the spatial frequency respectively.

2.2.4 Faraday Isolator

In the case of experiments conducted using high power laser systems at high intensities, some part of the laser energy is reflected due to two non-linear scattering processes known as Stimulated Brillouin Scattering (SBS) and Stimulated Raman Scattering (SRS). While the SRS can be diverted into other direction by placing the plasma target at a small angle with respect to the laser incidence, the SBS reflection can not be avoided as it traces the path of laser incidence in the backward direction irrespective of target orientation. This can lead to catastrophe unless the reflected component is suppressed. The power amplifiers are pumped by flash lamps and the duration of the pump pulse is in hundreds of μs . Secondly, since the image relays expand the beam in the forward direction, they compress the back-reflected beam. Moreover, the reflected laser beam also gets amplified as population inversion persists over tens of μs . So the reflected beam intensity increases after each amplifier which can damage the optical components like laser rods, lenses etc. In order to isolate the reflected component, Faraday isolators are used between the amplifier stages. A schematic diagram of a Faraday isolator is shown in Fig. 2.3.

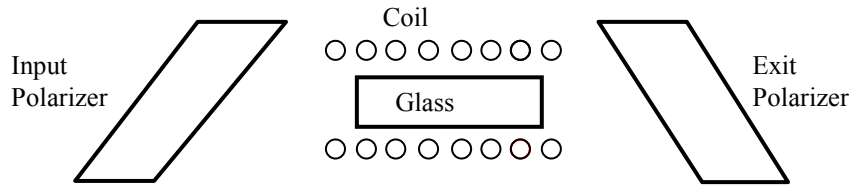


Figure 2.3: *A schematic diagram of a Faraday isolator*

The Faraday Isolator (FI) works on the magneto-optical effect in which the polarization plane of a laser beam is rotated when it is passed through a medium placed in the external magnetic field along the laser propagation direction. A Faraday isolator consists of an input polarizer, Faraday rotator (consisting of a Faraday glass kept in either permanent or pulsed magnetic field), and exit polarizer with its orientation at 45° with respect to the input polarizer. The magnetic field is adjusted so that the plane of polarization of the laser beam gets rotated by 45° in single pass. So, in the forward direction, the exit polarizer placed after the Faraday rotator fully transmits the laser beam. When the reflected component reaches the FI, it further rotated by 45° in same direction, as the sense of rotation of the polarization depends only on the direction of the magnetic field and not on the direction of the laser beam. The polarization plane of the back-reflected beam is thus at 90° w.r.to the input polarizer, which blocks the back-reflected beam.

Usually for small beams, permanent magnets are used. As the beam size increases, the magnetic field is generated by passing pulsed electrical current through a solenoidal coil in which the Faraday glass is placed. The Faraday rotation angle is expressed as

$$\theta = V \cdot B \cdot L \quad \text{.....2.3}$$

where θ is the rotation angle (minutes of arc), V is the Verdet constant of the glass, B is the magnetic field (tesla) and L is the length of glass (meters). A material with a large value of

Verdet constant is chosen as Faraday rotator to reduce the thickness of the Faraday glass. The leakage depends on the contrast factor of thin film polarizer (large size) which is usually between 100 - 400. In our high power laser system, four Faraday isolators are used.

2.2.5 Control System

A dedicated control system handles the timing of charging and firing various sub-systems in the high power laser system. All the flash lamps in the amplifiers are connected to capacitor banks. As the SL223 oscillator used in plasma experiments is a repetitive system, the control system takes the signal from the oscillator pulse to synchronize the oscillator output with the flash lamps. Similarly, in order to block all the other oscillator pulses, a mechanical shutter is also triggered just before firing the laser system. In addition, the laser system also has many current monitors for the flash lamps, laser alignment systems, and energy monitoring systems. The control system also provides trigger pulses for plasma diagnostics like CCD camera.

2.3 10 TW femtosecond laser system

A commercial Ti:sapphire laser system (M/s Thales, France) working on the scheme of chirped pulse amplification was used in the chirped pulse diagnostics to study plasma expansion (discussed in Chapter 4). Fig. 2.4 shows a photograph of the laser system and the pulse compressor. The system starts with a Ti-Sapphire oscillator (Femtosome Scientific Inc.) which generates laser pulses of < 20 fs duration, with > 4 nJ energy per pulse at a repetition rate of 76 MHz (average power > 300 mW). Kerr-lens mode-locking technique is used for generating such small duration pulses⁷⁵. The spectral bandwidth of the oscillator pulse was > 40 nm. The oscillator is pumped by the second harmonic of an Nd:YVO₄ laser. The oscillator pulses are temporally stretched using a pulse stretcher and then amplified in the laser amplifier system

(Alpha 10) consisting of a regenerative amplifier (pumped by the second harmonic output of an Nd:YAG laser), a multi-pass pre-amplifier, and another multi-pass amplifier pumped by two Nd:YAG lasers, as shown in the schematic diagram of the laser system shown in Fig. 2.5. All the three amplifiers provide a combined gain of about 10^9 . The amplified output is compressed back nearly to original ultra-short pulse duration using a pulse compressor. The technical specification of the 10 TW femto second laser system are given in Table 2.3.

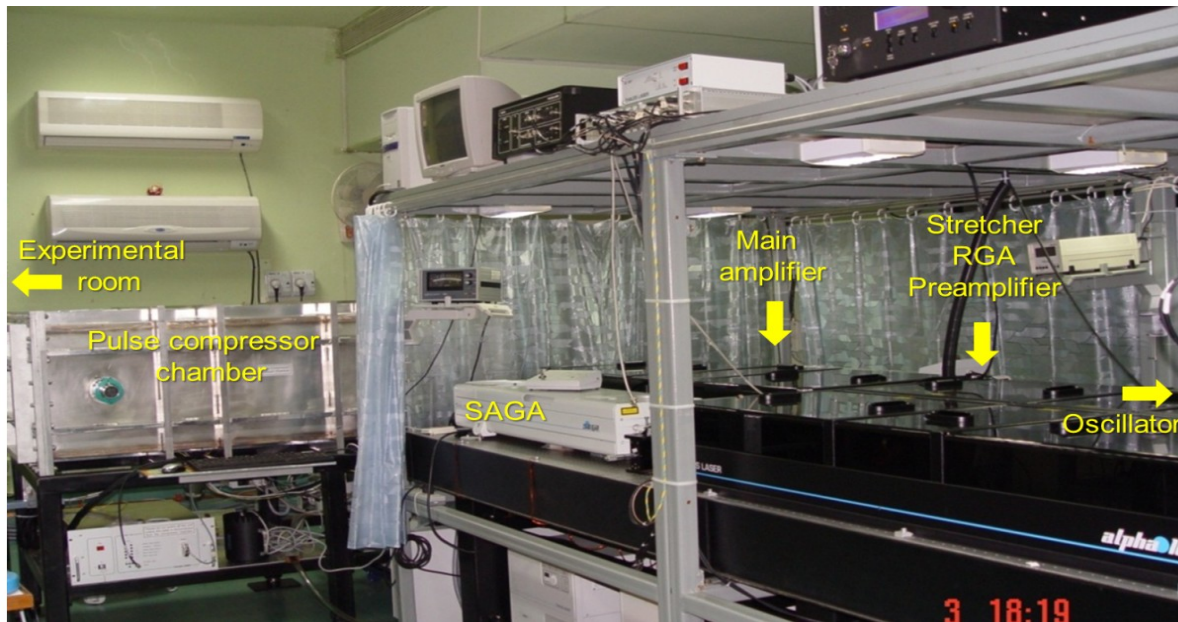


Figure 2.4: A photograph of the 10 TW Ti:sapphire laser system at RRCAT.

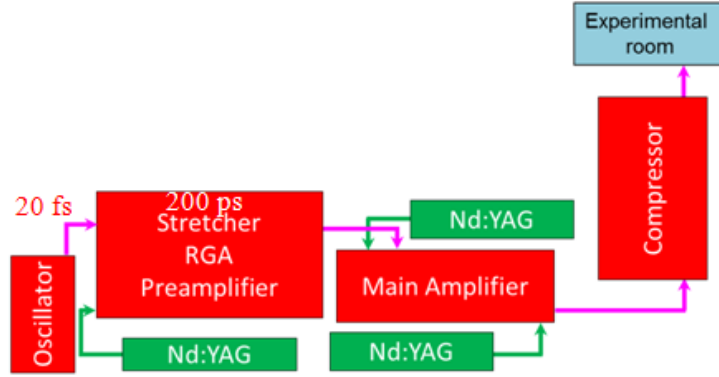


Figure 2.5 : Overall schematic layout of the Ti:sapphire laser system.

Parameter		Value
Pulse duration	τ_0	45 fs
Central wavelength	λ_0	800 nm
Spectral width	$\Delta\lambda$	20 nm
Pulse energy		upto 450 mJ
Pulse power	P	≤ 10 TW
Repetition rate		10 Hz
Pre-pulse contrast (ns level)		10^6

Table 2.3 : Parameters of the 10 TW Ti:sapphire laser system.

2.3.1 Kerr lens mode locking

It is known that by inducing fixed phase relationship among the longitudinal modes of a laser resonator, it is possible to get laser pulses of extremely short duration ranging from few picoseconds down to tens of femtoseconds. This process of inducing fixed-phase is known as phase locking or more popularly mode-locking. The minimum possible time duration ' Δt ' for a

laser pulse with Gaussian time profile and bandwidth $\Delta\nu$ is $0.441/\Delta\nu$. The time-bandwidth product for a laser pulse with a hyperbolic-secant-squared (sech^2) profile is 0.315 (instead of 0.441 for a Gaussian pulse). Thus, for a Ti:sapphire laser medium with 128 THz bandwidth, the minimum possible duration turns out to be 3.4 fs. In reality, other factors like actual pulse shape, overall dispersion of the cavity etc. decide the minimum attainable pulse duration. In the case of femtosecond laser systems, Kerr lens mode locking (KLM)⁷³ is the most common method of mode locking lasers. It uses the non-linear optical property of the medium known as *optical Kerr effect* which relates the effect of electrical field strength of an electromagnetic wave (light) on the refractive index of the medium. The refractive index (n) for an electromagnetic wave with a Gaussian spatial profiles will be greater at the axis compared to the edges, as it depends on the intensity ($n = n_0 + n_1 I$). Thus, a lasing medium itself acts as a Kerr lens at higher intensities which leads to self-focussing of the beam. So compared to low intensity (long duration) pulses that do not experience any focussing, the cavity would be more favourable to high intensity pulses if one places an aperture allowing only these focussed beams. Earlier laser systems used hard apertures to attenuate other modes. Present laser systems use a soft aperture determined by the overlap between the pumped beam and the laser beam. In the case of cavities with flat end mirrors and laser crystal acting as a thermal lens, the beam size on the mirrors become small. This effect becomes more prominent in the case of Kerr lens (at high intensities). A scheme of soft aperture Kerr-lens mode locking is shown in Fig. 2.6.

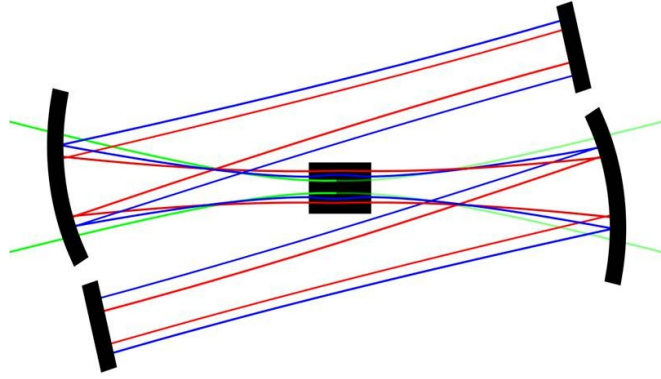


Figure 2.6: *Soft aperture Kerr-lens mode locking. Within crystal from inside to outside: Green=pump, blue, red are shorter and longer pulses (Courtesy: Wikipedia : Arnero)*

The generation of femtosecond laser pulses starts after the laser cavity is disturbed externally by kicking the end mirror of the cavity (through piezo mounted end mirrors). This process known as ‘coherent spike’ is used to generate very short duration laser pulses. In order to reduce the pulse distortion or stretching due to dispersion in crystal and in air, optical elements like prism pairs and chirp mirrors are used in the cavity. This way, a stable femtosecond laser pulse is obtained.

2.3.2 Chirped Pulse Amplification

If a short pulse (whose intensity is already high) is amplified, its increased intensity can damage the medium. So, the duration of laser pulse is decided such that the intensity (after amplification) is within the safe margins, keeping in view the damage threshold values for the amplifiers. One way to draw more energy operating within safe intensity limits is to stretch the pulse duration. This is done in the "Chirped Pulse Amplification" technique⁴ shown in Fig. 2.7 to amplify femto second laser pulses.

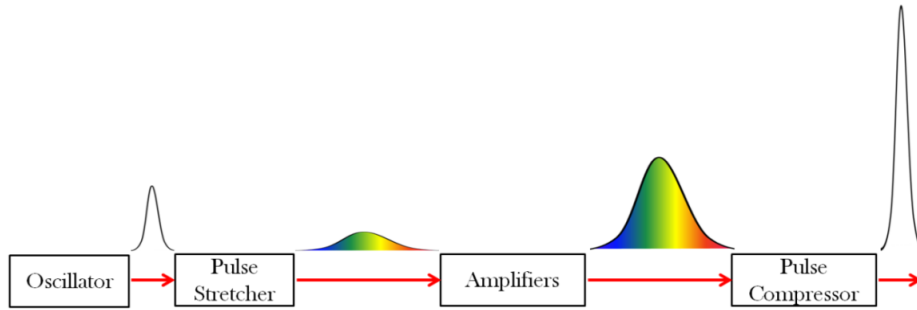


Figure 2.7: *The principle of laser chirped pulse amplification.*

Longer the stretched pulse, higher the amplified pulse energy one can reach without damaging the optics. Typically the fs pulse is stretched by a factor between 1000- 5000 times using a special single grating stretcher to reduce the peak power. In earlier days, the ps pulses were temporally stretched using bundles of long optical fibres. The fibres also increase the laser pulse bandwidth by self-phase modulation, which is a non-linear effect, which is not reliable as its is intensity dependent. The important requirement for temporal stretching is that it must be reversible after amplification. The standard method to stretch a fs laser pulse is using the dispersion properties of gratings (or prisms). The main idea here is to make different wavelengths travel different optical paths so that they will be at different points on the temporal profile of the stretched pulse. Figure 2.8 shows a standard configuration of a pulse stretcher using a grating pair and a lens pair (Martinez configuration), which is easy to understand. In our 10 TW Ti:Sapphire laser system, the stretching is realized using a single grating as discussed later⁷³.

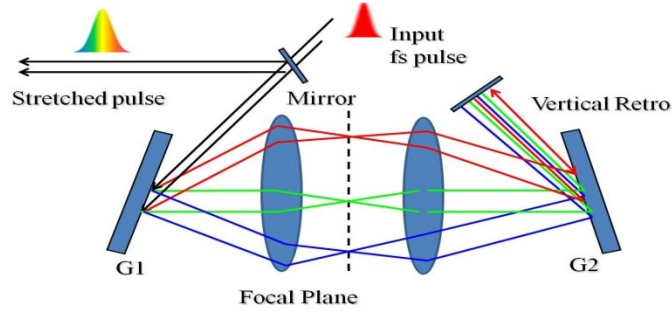


Figure 2.8: *Pulse stretcher configuration using two gratings and an afocal telescope system.*

2.3.2.1 Martinez Pulse stretcher

In Fig. 2.8, the plane reflection grating G1 disperses difference frequency components of femtosecond laser beam incident on it. After G1, they are incident at different points on the grating G2 (through the lens pair) as shown above. The distance between lens 2 and G2 is less than focal length of lens 2. It can be seen that the optical path between the G1 and vertical retro mirror is varying with location. Here the blue components are travelling longer optical path compared to their red counterparts and hence delayed (i.e. temporal chirp, which is desirable). In addition, they are also spatially separated (i.e. spatial chirp, which is *undesirable*). To remove this spatial chirp, the collinear output is folded back into the system by the vertical retro mirror at a height which is different from the incident one. The reflected beam follows the path G2, G1 and then incident on the plane pick-up mirror. This mirror directs the chirped pulse into the amplifier stages for further amplification.

2.3.2.2 Offner Pulse stretcher

In the 10 TW system used in some of the experimental work reported in this thesis, an all reflective variation of this configuration known as Offner type (Fig. 2.9) is used for stretching the 20 fs oscillator pulse to 200 ps duration⁷³. A single pulse selected from the 76 MHz pulse

train at every 100 ms (10 Hz) is amplified to few micro joules using a regenerative amplifier (Regen). A Faraday isolator separates the stretcher and regenerative amplifier.

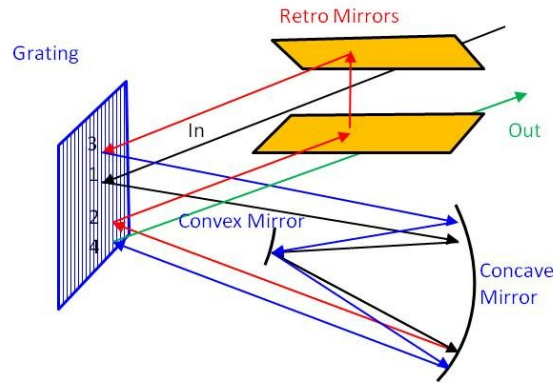


Figure 2.9: *Offner type Pulse Stretcher*

2.3.3 Regen and Pre-Amplifiers

The first amplifier after the stretcher output is a regenerative (regen) amplifier operating in a TEM₀₀ laser resonator mode to deliver diffraction-limited beams. A *Twin Peaks* Pockels Cell (MEDOX system) is used to feed the oscillator pulse inside and also dump the cavity output pulse from the regenerative cavity. It is a low gain multi-pass amplifier working in small signal amplification regime. The regen and the following pre-amplifiers are pumped by a Nd:YAG laser (Make : Compact). The gain of this regenerative amplifier in single pass is ~ 2 and overall gain is $\sim 10^5$. The cavity geometry is optimized to generate large Gaussian beams using a relatively short cavity. The output of the regen is then further amplified, first in a 4-pass pre-amplifier and then the main amplifier, to achieve final energy of ~ 600 mJ in 200 ps. The main amplifier is also a 4-pass Ti:sapphire amplifier pumped by second harmonic output of two Nd:YAG lasers (SAGA1 & 2). The overall gain of the amplifier system is about 10^9 .

The repetition rate of the laser pulse can be varied by changing the injection and ejection frequency of the pulses. Due to the finite contrast factors of polarizing optics, the output has laser pre-pulses before the actual 600 mJ pulse. These pre-pulses include : a) Amplified Spontaneous Emission (ASE) component introduced in the regenerative amplifier and the two multi-pass amplifiers, and b) replica pre-pulse. The second one is generated due to leakage of part of the mode-locked pulse train just before the actual pulse is switched out by the Pockels cell and polarizer combination. By using a pulse cleaner incorporating a fast Pockels cell (about 1 ns rise time) to rotate the polarization of the main pulse alone, the pre-pulse content can be reduced. Depending upon the switching speed of the Pockels cell and contrast factor of polarizers, the output laser pulse has a contrast of 10^6 for ns level pre-pulse. Output from the pulse cleaner is compressed in time using a pulse compressor to pulse durations ~ 45 fs duration with energy ~ 450 mJ.

2.3.4 Pulse Compressor

The pulse compressor⁷⁶ is to reverse the additional path differences introduced in different wavelength components in the pulse stretcher. By employing a pair of parallel gratings with a groove density of 1500/mm and a retro mirror, the positive chirp of the 200 ps laser pulse is compensated as shown in the Fig. 2.10. The first grating disperses different wavelengths and they are made to travel different optical paths opposite to the stretcher. They are incident on the retro mirror and trace back the path.

The second order auto-correlator output corresponding to shortest pulse duration and its line profile are shown in Fig 2.12(b) and (c)

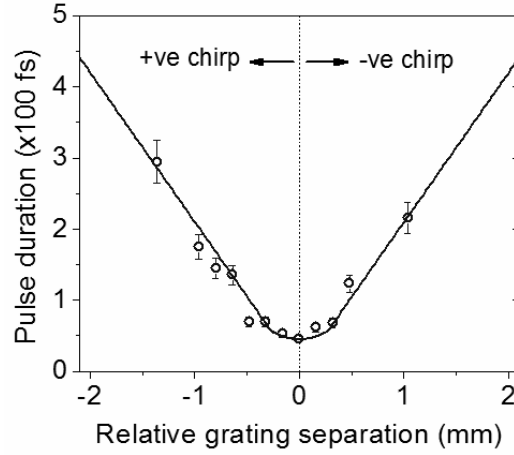


Figure 2.11: Relation between the laser pulse duration and the grating separation

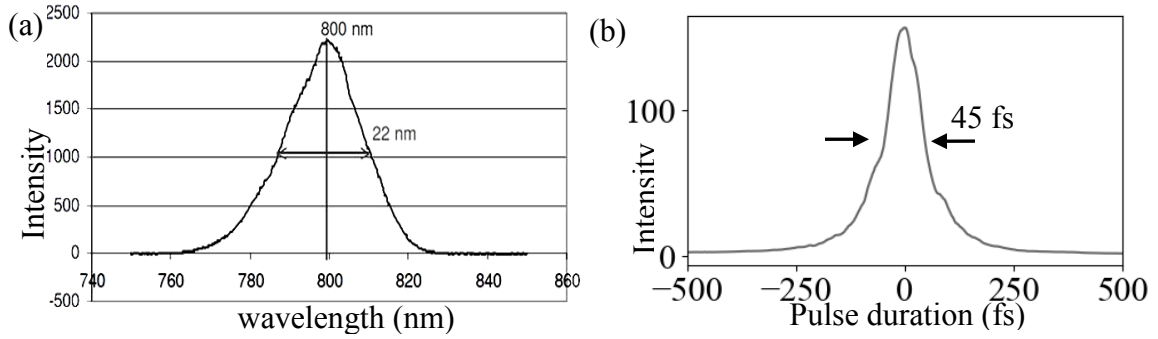


Figure 2.12: (a) spectrum and (b) corresponding pulse duration after pulse compressor

The femtosecond laser beam is transported using an evacuated beam line up to the plasma chamber. This is required as its transportation in air would distort its wavefront quite severely due to its high intensity. The laser intense beam is generally focussed by using an off-axis parabola (OAP) for high intensity laser - plasma experiments. However, the experiments presented in this thesis were conducted by focussing the laser beam using a lens, since the intensities were lower in our case. Those experimental details are presented in Chapter 4.

Chapter 3 : Diagnostics for Laser Produced Plasmas

3.1 Introduction

For plasma generated by irradiating a target with an intense laser beam of the pulse duration typically below few nanoseconds, the duration of the plasma is also in nanoseconds. Since to generate high intensities the laser beam is generally focussed to a focal spot of few tens of microns, the spatial extent of the plasma is also quite small. Due to these two factors viz. short temporal duration and small spatial dimensions, the laser produced plasma also has a steep density gradient. As these properties are quite different from those of magnetically confined plasmas, completely different diagnostics are required for understanding the laser-plasma interaction. The overall objective of any plasma diagnostics is to obtain information about the state of the plasma at different times during the laser-plasma interaction and later. The small duration of the laser produced plasmas which does not exceed few ns (limited by the hydrodynamic expansion and radiation losses) thus poses many challenges in developing diagnostics.

The typical temperature of the laser produced plasma varies from few eV to hundreds of eV. At these high temperatures, the plasmas have strong emission in the optical and x-ray wavelength range which can be used for diagnostics purpose. In addition, these plasmas can also be probed using external radiation in the form of either a laser (optical diagnostics) or x-rays generated from another laser produced plasma (x-ray backlighting). Depending on whether the plasma is probed by an external radiation or the emission from the plasma is being analyzed, it is called external / internal probing. The external probing includes techniques like shadowgraphy, interferometry, polarization studies etc. Similarly, studies based on plasma emissions use

intensity ratios of emission lines, slope of Bremsstrahlung radiation spectrum, imaging of plasma using pinhole camera with different absorption filters, to obtain information about plasma parameters like temperature and density. The information provided by these different types of diagnostics, which in general, are complimentary to one another, forms a complete picture of laser plasmas. For example, the x-ray diagnostics can be used to probe dense, high temperature plasma regions, to study lattice dynamics^{79,80,81} etc. Similarly mono-energetic proton radiography has been used for measuring the electric and magnetic fields generated in laser produced plasmas and studying the implosion dynamics^{82,83}.

The present chapter briefly describes different optical diagnostic techniques to get time resolved information and compares their advantages and disadvantages. The next section starts with discussion of the snap shot approach in which a short duration probe beam is passed tangentially to the laser produced plasmas and the transmitted beam profile is recorded using detectors like CCD, DSLR cameras. In order to obtain the temporal evolution, several shots at different delays between the heating pulse and probe pulse are required under identical conditions, which is quite difficult to achieve. As an alternative to this, multi-frame snap shot diagnostics were developed wherein multiple probe beams are passed through the interaction region at different angles at different time delays. As the information is integrated over the probe pulse duration, one has to keep the probe pulse duration as short as possible. The second approach is to use a long probe duration and obtain the temporal information by using a time dispersing instrument like an optical streak camera. In this case, continuous temporal information with 1-D space resolution, can be obtained in a single shot.

With the advent the chirped pulse amplification (CPA) technique, amplification of femtosecond laser pulses has become a standard method in which the pulse is stretched in time,

for further amplification. In this technique, the temporal stretching is done using diffraction gratings which together introduce a linear chirp in the frequencies. With this well defined wavelength ' λ ' vs time ' t ' relation, these laser pulses can be used as a diagnostics tool to obtain time resolved information, simply by recording the spectrum of the transmitted probe beam. This is a simpler alternative to an optical streak camera and offers temporal resolution of few picoseconds and lower. These chirped pulse diagnostics will be briefly discussed in this chapter. The discussion will conclude with a relative comparison of the different techniques. Since some of these techniques are described in more detail in the subsequent chapters, the present chapter is used to review the scope / strengths of these techniques, by discussing the works carried out in different laboratories.

3.2 Time resolved studies using snap shot / multi-frame approach

Probing of laser produced plasmas by using a short duration laser pulse as an external probe, is a useful technique for studying the evolution of the plasma in space and time. In most of the cases, the probe laser beam is derived from the main laser system itself, since this offers ease of synchronization. Alternately, one can use a laser pulse from a different laser system, but in that case one has to synchronize these two lasers accurately. The exact information one obtains from these studies depends on the configuration in which the diagnostics is carried out. For example, by constructing an interferometer around the laser produced plasma and using a short duration laser pulse, one can obtain the two dimensional density profiles^{84,85,86} of the plasma at different times. Interferometry has also been used to measure nanometre level movements of the laser irradiated target⁸⁵. Similarly, by recording the changes in a polarized probe beam, depolarization studies and information about the self generated magnetic fields in

the laser plasmas can be obtained⁸⁷. For example, Stamper *et al* had measured the of spatial profiles of self generated magnetic fields in nanosecond laser produced plasmas⁸⁸. This was accomplished by placing the plasma between two crossed polarizers and recording the spatial profile of the transmitted probe beam after the second polarizer. By performing the shadowgraphy experiments using an external laser probe, one can study the plasma dynamics, shock wave propagation in transparent media, and particle velocity measurements shock wave experiments⁸⁹. So in essence, by using a short duration laser pulse as an external probe, different types of studies can be performed in the laser produced plasmas.

A schematic diagram showing the setup of snap shot interferometry diagnostics using a short duration probe is shown in Fig. 3.1. The probe passes through the interaction region and

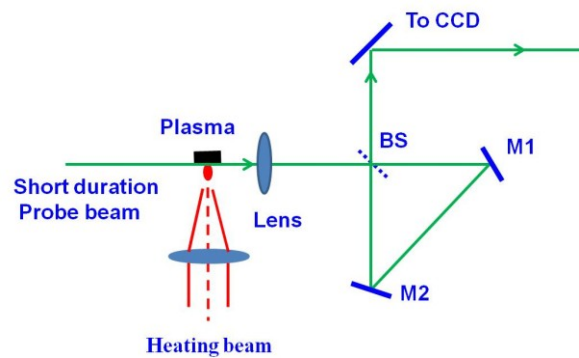


Figure 3.1: A schematic diagram of a typical setup used for snap shot interferometry

the transmitted beam is imaged on to the detector by an imaging lens. In the case shown in Fig. 3.1, a cyclic interferometer setup after the lens generates lateral shearing between the reflected and transmitted components to generate interference fringes. In this configuration, a probe of larger cross section is passed through the laser plasma. By overlapping non plasma region of the wave front with the wave front containing plasma, interference fringes are generated and plasma density is estimated from the fringe shifts. Unlike a Michelson type interferometer, the

cyclic type offers exactly identical path to both the arms which is important for reducing the difference in their optical paths. This becomes crucial for short duration probe pulses due to coherence length issues.

3.2.1 Generation of the probe beam

In the case of high power lasers, the simplest solution is to split a portion of the main laser beam (which produced plasma) after appropriate amplifier stage and use it as probe the beam. In this case, since both the probe and heating laser pulse are derived from the same source, there is no issue of jitter between the two pulses. Then depending on the distance the heating pulse propagates before it is incident on the target, the probe beam has to propagate over similar distance for synchronization. By using a variable delay line consisting of either a retro mirror or pair of mirrors, the delay between the two pulses can be varied. The synchronization between the two pulses is achieved to the desired accuracy by detecting the two pulses using either a photo diode or an optical streak camera.

3.2.2 Duration of the probe pulse

Ideally, the duration of the probe pulse should be as short as possible for snap shot approach. In most of the cases, the detector used in these experiments is a simple CCD camera which has microsecond to millisecond exposure time. So the information is integrated over the probe pulse duration. If the phenomenon to be studied is much faster than the probe pulse duration, information will be smeared over the probe pulse duration. So depending upon the phenomenon under investigation, one has to choose the probe pulse duration. For example, for a phenomenon like plasma expansion, where the typical velocities are 10^{5-6} cm/s, ns duration pulses are quite acceptable. However, when the laser- plasma interaction processes are to be

studied with a better time resolution, shorter duration probe is required. In the case of generating the probe beam by splitting a portion of the main laser, the probe pulse duration cannot be varied. In such cases, one can use a short duration laser pulse from another laser system which is well synchronized with the main laser.

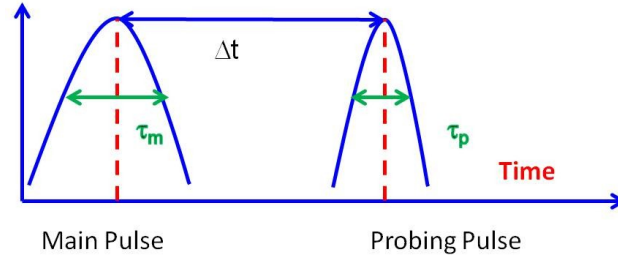


Figure 3.2: *Time separation between the main and probe pulses*

In the case of long probe pulses, the calculation of experimental parameters like plasma expansion velocity or shock / particle velocity in the shock wave experiments can yield erroneous results unless the temporal separation ' Δt ' between the heating and probe pulse is properly identified. In Fig. 3.2, ' Δt ' is the separation between the peaks of the main pulse and the probe pulse, as shown, and τ_m , τ_p are the durations (FWHM) of the main and probe pulses. Once the plasma is generated by the main pulse, it will start expanding. The detector continues to record the transmitted probe even after the peak of the probe pulse is over. Moreover, the plasma generation is not occurring just near the peak of the main pulse. So one has to take the temporal profiles of the main and probe pulses into consideration and not just the separation between the two peaks.

3.2.3 Wavelength of the probe beam

The propagation of the probe beam is modified by the presence of free electrons in the plasma. The dispersion relation expressing the variation in the wave number ' k_L ' and the frequency ' ω_L ' of the probe beam on the plasma frequency ' ω_p ' is given as

$$k_L^2 c^2 / \omega_L^2 = 1 - \omega_p^2 / \omega_L^2 \quad \text{.....3.1}$$

$$\omega_p^2 = 4\pi n_e e^2 / m_e \quad \text{.....3.2}$$

where the plasma frequency ' ω_p ' depends on the electron density ' n_e '. From this, it can be seen that, as the probe laser propagates towards higher electron densities the refraction effects become stronger and at the critical density ' n_c ' where the frequencies of probe laser ' ω_L ' and plasma ' ω_p ' become equal, the laser light can no longer propagate. Even at densities $< n_c$, the probe beam gets strongly refracted away from the propagation direction and many not reach the detector. This also depends on the size of the imaging optics (i.e. the collection angle). An important point to note is that the wavelength of the probe beam determines the electron densities up to which one can probe. Thus, in order to probe higher and higher density regions, shorter wavelengths are always preferred for the probe. In order to do this, nonlinear optical techniques like second harmonic generation (2ω) are used to down-convert the laser wavelength. The harmonic generation also helps in reducing the pulse duration to some extent. In second harmonic generation of ns laser pulses, the pulse duration is reduced 0.7 times for Gaussian profiles. In the experiments at high laser intensities, strong plasma emission occurs at 2ω and $3/2\omega$ frequencies. In this case, if one uses the harmonics as probe, it becomes really difficult to suppress the plasma emission forming background in the experiments. One way to solve this problem is by shifting the 2ω laser frequency using a Raman up converter to slightly higher frequencies and

then use it as a probe. Pressure cells filled with helium gas at higher pressures (20 bar) have been used for this purpose⁹⁰. In this case, optical interference filters allowing only a small $\Delta\lambda$ around the Raman wavelength, are used to suppress the plasma emission allowing only the probe to pass through, thus blocking all other wavelength including scattered light at ω and 2ω . Kaluza *et al* have recorded two picosecond-separated images of the plasma evolution by temporally separating the 1ω and 2ω components using a dispersive medium⁹¹. Joshi *et al* have reported a novel scheme in which by probing simultaneously with two wavelengths, the density and magnetic field information can be obtained without interferometry⁹².

Pump-probe polarimetric experiments have been performed to detect spontaneous magnetic fields generated due to highly directional hot electron jets at laser intensities of 10^{16} W/cm² with a temporal resolution of sub picoseconds⁹³. In this case, both the heating and probe pulses were of fs duration. By varying the delay between the pump and probe using a high resolution translational stage, the onset and evolution magnetic fields has been studied (Fig 3.3).

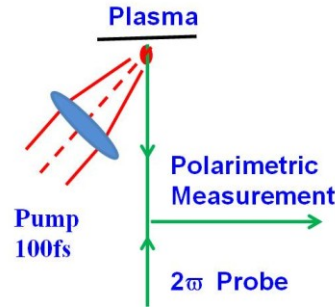


Figure 3.3: Pump probe experiments with sub picosecond resolution

Thus it is possible to obtain a good temporal resolutions by using probe of suitable duration. It may be noted is that one should know *a priori* what kind of temporal resolutions are desirable for the phenomenon being studied.

3.3 Time resolved studies using multi-frame diagnostics

Another important point to be noted is that when the phenomenon under study is occurring for a longer duration, many shots are required at different pump-probe delays to reconstruct the complete temporal evolution, if short duration probes are used. Multi-frame diagnostics has been developed⁹⁴ for addressing this issue. In this approach, the probe beam is split in to multiple components and passed through the laser plasma interaction regions at different delays with respect to the main beam. A schematic diagram of a typical setup used of three-frame shadowgraphy, is shown in the Fig 3.4.

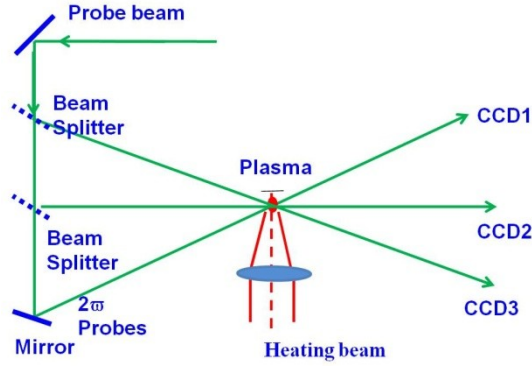


Figure 3.4: A schematic diagram of a typical setup used of three-frame shadowgraphy

Fedosejevs *et al* have reported use of multi-frame interferometry to study the self-steepening of the density profiles of CO₂ laser-produced plasmas⁸⁴. Meyer *et al* have studied the correlation between the temporal variation in the density scale lengths and the two plasmon instability by simultaneous use of multi-frame interferometry and Thomson scattering⁹⁵.

3.4 Time resolved studies using streak camera, chirped probes pulses

Laser plasma diagnostics based on the snap shot approach and multi-frame approach to study the temporal evolution of the plasma has been discussed in the previous section. It is seen

that the temporal resolution is decided by the pulse duration of the probe pulse as the information is integrated over the probe pulse duration. On the other hand, if too short duration pulses are used for probing the laser plasmas, large number of shots are required to reconstruct the temporal evolution. Another important thing to note is that the experimental conditions being not exactly identical over all these shots, the reconstructed information may have errors. A solution lies in using detectors like optical streak camera which provide time resolved information in a single shot. Although it is possible to use detectors like streak camera, framing camera, gated ICCD etc., to obtain time resolved information by recording the self emission (optical / x-ray) from the plasmas, the discussion here is restricted to the external probing techniques. With the advent of femtosecond laser systems using chirped pulse amplification technique, another simple option has become available for probing the laser produced plasmas using the chirped probe pulses. Both these techniques are discussed here.

3.4.1 Time resolved studies using Streak Camera

Instead of using a short duration pulse to probe the plasma and record the images with simple CCD cameras, one can use a long duration probe pulse and use gated detectors like ICCD cameras or framing cameras with integration times in picosecond to nanosecond range. This way, the time evolution can be obtained at discrete time steps. In order to obtain continuous temporal information in a single shot optical streak cameras are used. More details about the streak camera are given in Appendix A at the end of this report. In this case, a long duration probe pulse is passed through the laser plasma interaction region. The transmitted probe beam is made incident on the entrance slit of the streak camera, which disperses this information in time, and displays the spatial and temporal variation of transmitted probe beam.

As described in the previous section, this approach (long probe pulse and streak camera) also can be used in different configurations e.g. shadowgraphy, interferometry, and polarimetry. Prasad *et al* have coupled a cyclic lateral shearing interferometer to an optical streak camera to obtain time resolved interference fringes from which temporal evolution of the electron density was estimated⁹⁶. The experimental setup is shown in Fig 3.5.

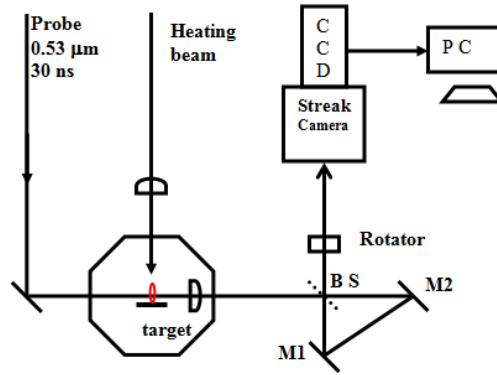


Figure 3.5: Schematic diagram showing the experimental setup¹

The results from the time resolved interferometry experiments are shown in Fig. 3.6. Figure 3.6a shows a reference interference fringe pattern in time domain. Here the vertical direction gives

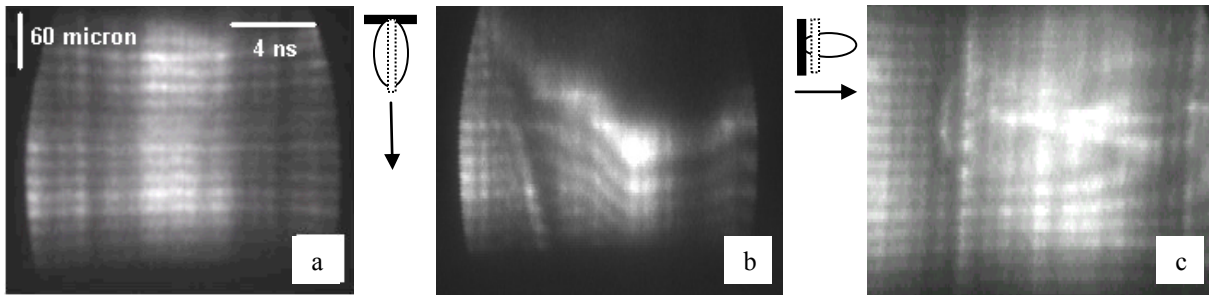


Figure 3.6: Interferograms recorded for aluminium plasma; (a) in the absence of plasma, (b) with streak camera slit (dotted lines) parallel to plasma expansion direction (arrow), and (c) with slit perpendicular to plasma expansion direction.

the spatial variation along the entrance slit of the streak camera. Figure 3.6b shows the shifts in these interference fringes with time. In this case, the plasma plane was imaged onto the entrance slit of the streak camera such that the plasma expansion is along the slit direction. An image rotator was used for this purpose. Figure 3.6c shows the case where the slit is perpendicular to plasma expansion direction. The typical time resolved density profiles obtained using this approach are shown in the Fig.3.7⁹⁶. Although the figure shows experimental points at discrete times and the curves drawn are for guiding purpose, it is possible to get the actual evolution (continuous experimental points) of the density by using automated fringe tracking software.

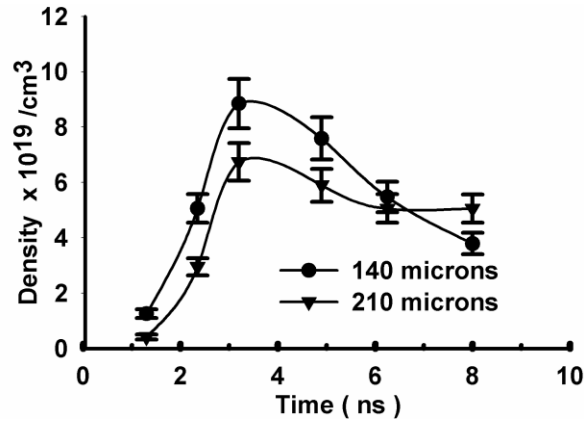


Figure 3.7: Temporal variation of the electron density for aluminium plasma at two axial distances¹.

By measuring the self generated third harmonic of the laser, propagating through the laser plasma, using an optical streak camera, Gopal *et al* have made a quantitative study on the temporal evolution of the self generated magnetic fields^{97,98}. These plasmas were generated using a 100 fs laser pulse at $9 \times 10^{18} \text{ W/cm}^2$. They had also detected a magnetic field of $340 \pm 50 \text{ MG}$ using cut-off method for higher order harmonics ($2^{\text{nd}} - 4^{\text{th}}$) in these experiments, at a laser intensity of $10^{18-20} \text{ W/cm}^2$.

In order to study the continuous temporal variation of the shock velocity in quartz glass in a single shot, Ng *et al*⁹⁹ had recorded the transmitted component of long duration probe pulse using an optical streak camera. Thus, it is possible to obtain the time resolved information using a long duration probe pulse and an optical streak camera or other devices like ICCD camera and framing camera. However, all these have few limitations associated with them. The temporal resolution of these devices varies from tens of picoseconds to few nanoseconds. Secondly, they are also quite expensive. An attractive alternative came up with the femtosecond lasers in the form of chirped pulse diagnostics that can provide down to tens of femtosecond time resolution if required. This technique is discussed below. Details of our work about chirped pulse diagnostics to obtain the various plasma parameters like expansion velocity and plasma density are discussed in Chapter 4. The discussion presented here is aimed to highlight the strengths of this approach.

3.4.2 Chirped pulse diagnostics

As the technology of generating femtosecond lasers evolved, the chirped pulsed amplification became a standard technique to amplify the femtosecond laser pulses. In this technique, the femtosecond duration laser pulses from the oscillator are stretched in time by spectrally dispersing them using a pair of diffraction gratings. This temporal stretching needs to be done to keep the laser intensity below the damage threshold of the optical elements in the path of the laser propagation. The stretched pulses are further amplified in “regenerative” and “bow tie” type amplifiers. The diffraction gratings in the stretchers are arranged so that the long wavelength components of the laser pulse travel a shorter path compared to the short wavelength components. This makes the laser pulse a positively chirped, one in which the higher wavelength components precede the shorter wavelength components. As the gratings introduce a linear

dispersion between different spectral components, this also leads to a well defined wavelength ' λ ' and time ' t ' relation. So by using a chirped pulse as a probe, one can obtain the temporal information simply by recording the spectrum of the transmitted probe pulse. By adjusting the grating parameters one can adjust the chirp factor, stretched pulse duration etc. This approach is much simpler in nature, does not involve expensive ICCD or streak cameras.

By using a pair of chirped probe pulses to probe the laser plasmas, Chein *et al* have reported single shot spectral-interferometry studies to measure the femtosecond ionization dynamics of the air, with a temporal resolution of few femtoseconds¹⁰⁰. Of the two probe pulses acting as a reference, passed through the setup before the plasma formation, and the another one passed through the plasma. Geindre *et al* have extended work on similar lines to study the femtosecond breakdown of laser plastic targets. The temporal resolution possible by using a chirped probe pulse of duration ' t_c ' , generated from laser pulse of duration ' t_0 ' is given by¹⁰¹

$$\Delta t \sim (t_c t_0)^{1/2} \dots\dots\dots 3.3$$

Batani *et al* have used chirped pulse shadowgraphy as a diagnostic technique to study the propagation of fast electrons in a gas medium¹⁰². Another very interesting application of the chirped pulse diagnostics was reported by Benuzzi-Mounaix *et al* who have used the chirped pulse reflectometry to obtain shock parameters with ~ 1 ps resolution which was difficult to obtain using a streak camera. In these experiments, a chirped pulse was reflected from the rear side of the laser irradiated target (see Fig. 3.8) and the sudden fall in the reflected signal indicated the exact shock wave breakout time with high precision. By knowing the time separation between the heating pulse and probe pulse, the exact shock arrival times and thus the shock velocity could be estimated¹⁰³. This technique can also be used to study the shock

movements in bulk transparent targets as the ionization induced by the shock front leads to formation of good reflecting surface.

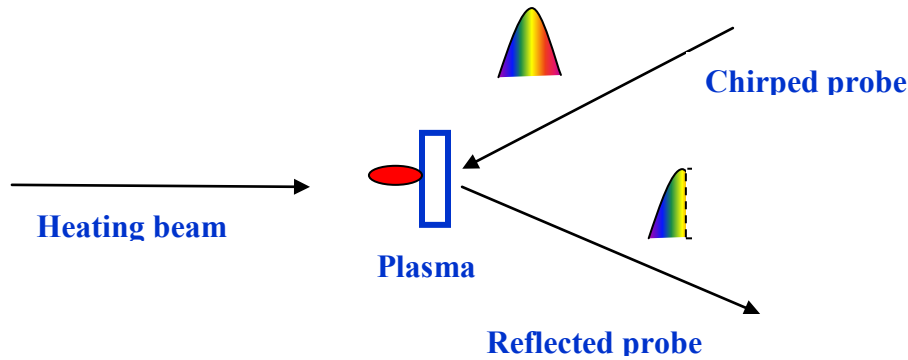


Figure 3.8: *A schematic diagram of the setup used in chirped pulse reflectometry*

3.5 Conclusions

Different probing techniques like the snap shot approach using short duration probe pulses, obtaining continuous temporal evolution using a long duration probe coupled with devices like streak / framing camera, ICCD camera etc., or by using chirped laser pulses to probe, have been discussed in this chapter. Many of these techniques are complementary to each other. Two important points to be considered are : 1) the time resolution needed for the phenomenon being studied, and 2) the available resources. In high power lasers, the laser pulse duration is usually fixed and consequently the duration of the harmonics. In the case of strong emissions from the plasma, use of Raman shifted harmonic appears to be an ideal solution. Under these conditions, if one requires temporal resolution of tens of picoseconds, use of devices like streak / framing camera or gated ICCD, is the solution. Expensive framing cameras or gated ICCDs can provide two dimensional time resolved (discrete) information, whereas streak cameras can provide one dimensional continuous time resolved information. However, in the case of femtosecond laser systems using chirped diagnostics like chirped pulse reflectometry,

shadowgraphy, and interferometry are more attractive, as they can provide temporal resolutions down to sub-picosecond level.

Permissions for reprinting figures

¹ Reprinted from *Simple interferometer for space and time resolved density measurements of laser produced plasmas* by Prasad, Y. B. S. R., Naik, P. A., Kumar, A. and Gupta, P. D., Review of Scientific Instruments 77, 093106 (2006), DOI:<http://dx.doi.org/10.1063/1.2349596>, with the permission of *AIP Publishing*.

Chapter 4 : Chirped Pulse Diagnostics for Laser Plasmas

4.1 Introduction

In order to study the evolution of laser produced plasmas in space and time, diagnostics with good spatial and temporal resolutions are required because of the special nature of these plasmas i.e. short period of existence (few nanoseconds) and small spatial extents (few hundreds of microns). This becomes very important while studying energy transport¹⁰⁴ which is crucial in generation of strong magnetic^{87,105,106} and electric fields and various high energy charged particles like electrons^{107,108,109} and protons^{109,110,111,112,113}. In order to understand the generation mechanisms behind these processes, one needs a knowledge of the space and time resolved profiles of plasma parameters like density, temperature, expansion velocity etc. Some optical diagnostic methods for probing laser produced plasmas have been discussed in Chapter 3. A technique discussed there viz., snap shot diagnostics^{114,115,116} employs a short duration laser pulse to probe the plasmas and the temporal evolution is reconstructed by taking multiple shots at different delays between the heating and the probe beams. Accuracy of this approach is limited by shot to shot variation in laser beam parameters which in turn results in change in the parameters of the plasma produced. Another drawback of this approach is that the information is integrated over the duration of the probe pulse. If very short duration probe pulse is used, several shots will be required to construct the complete picture of temporal evolution. This problem could be solved to some extent by using multi-frame diagnostics¹¹⁷ discussed in Chapter 3. However, the latter involves complicated optical alignment and the number of frames is also limited by practical considerations. One can overcome this problem by using an optical streak camera⁹⁶ with a long duration probe pulse to obtain continuous temporal evolution of the plasma

information as described in the previous chapter. However, this approach has two limitations. The first one is that the temporal resolution possible with a streak camera is limited to tens of picoseconds, and secondly, sensitive and expensive streak cameras are required. A novel and easier solution offering better temporal resolution in a single shot is reported in this chapter.

With the advent of ultra-short ultra-intense femtosecond laser systems employing the chirped pulse amplification method, a new solution to this problem could be found. Typical energy in the Kerr lens mode locked laser pulses is few tens of nanojoules with tens of femtosecond pulse duration. As the laser pulse duration is very small (10^{-14} s), any increase in the energy will cross the damage threshold of optical elements like mirrors, laser rods etc. Even below the damage threshold, there is severe phase distortion of the laser wavefront, which spoils focussability of the laser beam. In order to overcome this problem, the laser pulse is stretched in time by several orders of magnitude (hundreds of picoseconds to nanoseconds) before amplification and then compressed back to femtosecond time scale. Longer the duration of the stretched pulse, higher can be the amplified energy without damaging optical elements. In the early days of femtosecond laser systems, the stretching was accomplished using optical fibres. However, due to other problems associated with the fibres, this temporal stretching and compression was achieved using gratings by Gerard Mourou and Donna Strickland at the University of Rochester in 1985⁴. This technique is popularly known as *Chirped Pulse Amplification* (CPA). In a pulse stretcher, usually gratings are used to introduce a linear chirp, by making different wavelengths travel different distances. This also leads to temporal stretching of the pulse. This laser pulse, after amplification, is compressed back using another grating based pulse compressor (placed in high vacuum conditions) to femtosecond duration. We have used these chirped laser pulses to probe the laser produced plasmas for obtaining time resolved

information. The chirped pulses have been used for retrieving the phase information of femtosecond irradiated plastic targets with 50 fs time resolution¹⁰¹. Similarly, laser shock experiments had been performed in which shock parameters have been measured with 1 ps resolution¹⁰³. This approach is extended by us to obtain plasma parameters like expansion velocity and density information for the first time. The details of these techniques used and the results obtained are discussed in the subsequent sections of this chapter. The organization of the present chapter is as follows. Section 4.2 describes more details about the pulse stretching and characterization of the stretched pulses. Section 4.3 is about experimental setups used for chirped pulse shadowgraphy and interferometry measurements to estimate the plasma expansion velocity and electron density. The results from these experiments are presented and discussed in Section 4.4. Finally section 4.5 discusses the advantages and limitations of the chirped pulse diagnostics.

4.2 Generation of Chirped Pulses and Their Characterization

As mentioned in Chapter 2, chirped pulse amplification is a state of the art technique to amplify ultra-short femtosecond laser pulses by stretching them temporally before amplification. The temporal stretching is done in order to keep the peak intensities of the laser pulses below the required limits of a few GW/cm^2 (e.g. for a germanium window $94 \text{ GW}/\text{cm}^2$) above which the optical elements like laser rods will get damaged due to nonlinear processes like self-focussing. The concept of temporal stretching and compression is shown schematically in Fig.4.1.

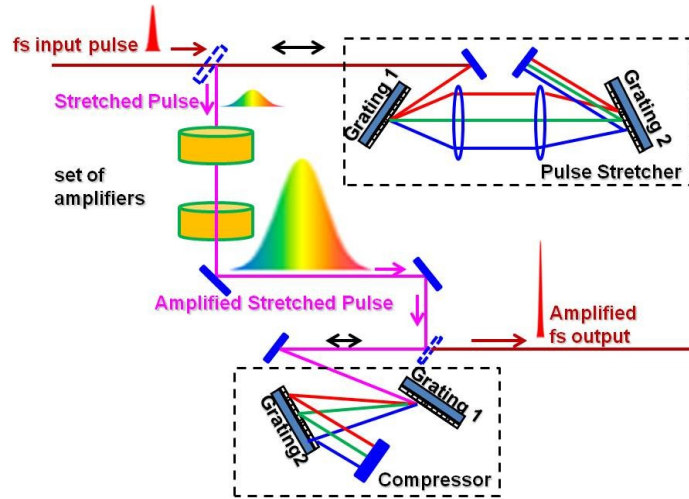


Figure 4.1: *A schematic diagram showing laser chirped pulse amplification*

The temporal stretching is achieved by spectrally dispersing different frequency components using a reflection grating and propagating them along different optical lengths and then combining once again for collinear propagation. A typical configuration of a pulse stretcher is shown in Fig. 4.2 below in which a low frequency component (red) travels a shorter path compared to a high frequency component (i.e. negative chirp).

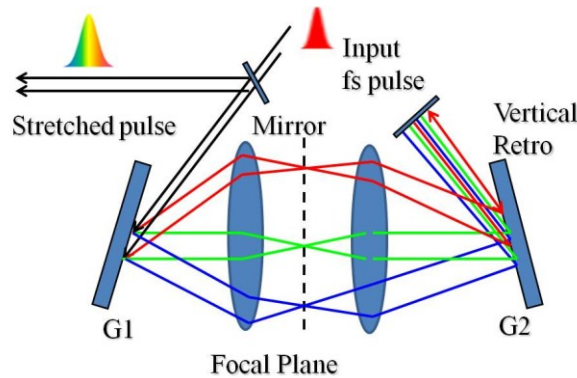


Figure 4.2: *A schematic diagram of a Laser Pulse Stretcher*

The working principle of the pulse stretcher is illustrated in Fig. 4.2. The input femtosecond laser beam is dispersed by the plane reflection grating G1. As seen in the Fig. 4.2,

different frequency components travel different path lengths between G1 and the vertical retro mirror and hence delayed relative to each other (blue component takes a longer path compared to the red component). In addition, they are also spatially separated. To remove this spatial separation (i.e. spatial chirp), these collinear outputs are folded back into the system by the retro mirror at a height which is different from the incident one. The reflected beam follows the path G2, G1 and then incident on the plane pick-up mirror. This mirror directs the chirped pulse into the amplifier stages for further amplification. The mirror is kept at a different height compared to the path of the input beam and thus does not block it. The amplified ps/ns laser pulse is compressed back using a pulse compressor, as described in Chapter 2. The schematic configuration of the stretcher described here is simpler to visualize the operation and uses achromatic lenses. In the Alpha-10 TW system used for the present set of experiments, an all reflective variation of this configuration, known as Offner stretcher, is used and explained in Chapter 2. Since our focus is on to use the chirped laser pulse to probe the plasmas to obtain time resolved information, the temporal and spectral characteristics of the probe pulse has to be measured accurately, which is described below.

4.3 Temporal Characterization of the probe pulse

In order to characterize the laser pulse which is to be used to probe the laser produced plasmas, one needs the wavelength ' λ ' vs. time ' t ' information. Although it is known that the gratings introduce a linear dispersion in the spectral content of the incident short femtosecond laser pulse, it had to be ascertained independently from experimental measurements, for instance using an optical streak camera coupled to a spectrograph. A typical spectral output of the laser is shown in Fig. 4.3.

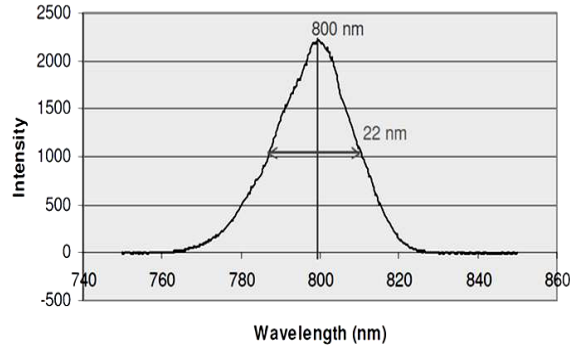


Figure 4.3 : *A typical spectrum of the stretched laser pulse*

From the spectral measurements, it is seen that the laser emission is centred around ~ 796 nm, with a bandwidth of 20 - 22 nm. The pulse duration (FWHM) of the stretcher output is ~ 200 ps. From this the dispersion factor was estimated as ~ 10 ps/nm. In order to experimentally determine the λ -t characteristics of the probe laser pulse, the spectrograph output was coupled to an optical streak camera, as shown in the Fig. 4.4 . Since the streak camera has a finite built-in delay, it was pre-triggered using the output from the master clock of the laser (D18) system.

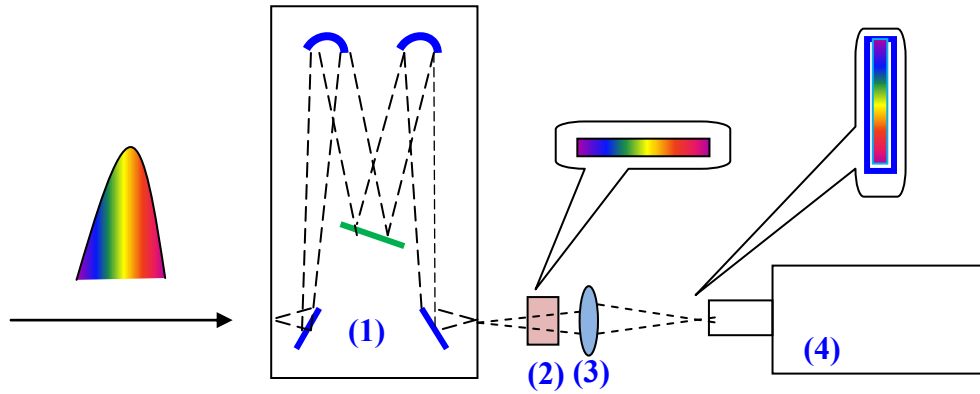


Figure 4.4 : *Setup to characterize the probe beam : (1) monochromator, (2) image rotator, (3) imaging lens, and (4) Streak camera with a CCD camera.*

The probe pulse was derived by splitting a portion of the laser beam using a pellicle beam splitter ($R=16\%$) just before the laser pulse compressor. This beam was focused onto the entrance slit of a spectrograph (after suitably reducing the energy of the beam by using absorption filters). A monochromator (CVI DigiKröm DK 480 1/2 meter) was used for dispersing the probe beam. To record the full spectrum, the exit slit of the monochromator was removed. As the dispersion was in the horizontal plane, an image rotator was used to rotate the dispersion plane by 90° before making it incident on the entrance slit of the streak camera. Different wavelength components arriving at different heights at different times on to the entrance slit of optical streak camera were swept horizontally in time. The streak camera was calibrated by varying the temporal delay between the femto second laser heating pulse and the pico second probe pulse by a known amount using an optical delay line. From the two recorded images, a sweep rate of the streak camera of 46 ps/mm (~ 1.3 ps / pixel) on the phosphor screen was obtained in the streak mode-1 used in the experiments. The pictures to calibrate the sweep rate are shown in Fig 4.5 (a) and (b) below. An additional path difference of 2 cm was introduced between the heating and the probe beams in fig 4.5(b).

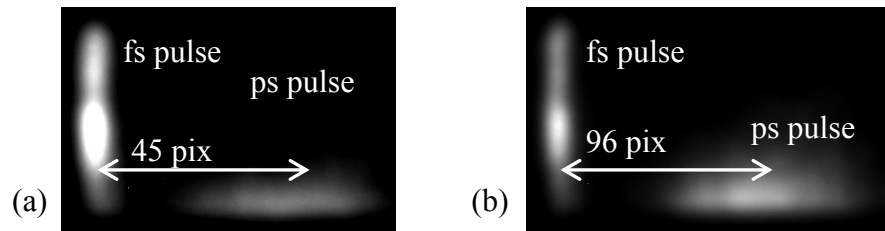


Figure 4.5 : (a) Calibration of the streak camera using fs heating and pico second probe pulses
(b) additional 2cm path difference between fs and ps pulses

Similarly the spectral dispersion along the vertical direction is measured experimentally as 6.7 nm/ mm(0.2 nm / pixel) by recording the position of a He-Ne laser spot at different spectrograph settings. The phosphor screen output of the streak camera was recorded using a Pixelfly CCD camera which was also pre-triggered by using another output of the same master clock of the laser system. The resultant time resolved spectrum is shown Fig. 4.6. From the slope of this streaked image, a chirp factor of ~ 10 ps/nm was calculated. As stated before, the streak camera measurements were used only to cross-check the linearity of the chirping and the dispersion factor. The details and calibration procedure of the streak camera are given in Appendix-A.

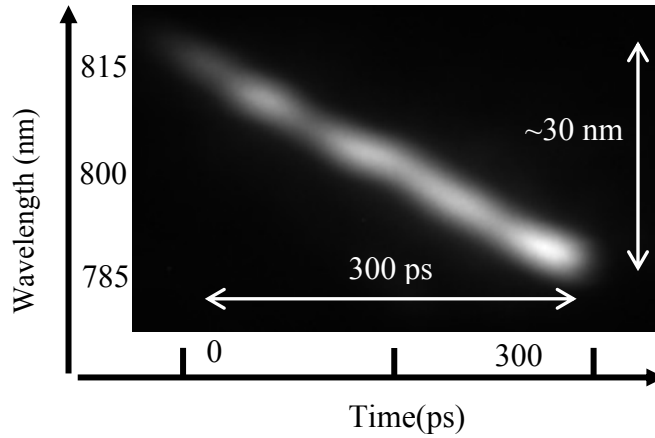


Figure 4.6 : *Streaked image of the probe beam spectrum showing a liner chirp^a*

4.4 Experimental Setup

Experiments using Chirped Pulse Shadowgraphy (CPS) technique and Chirped Pulse Interferometry (CPI) technique were carried out on the Alpha-10 TW Ti:sapphire laser system (Thales Optronique, France) delivering laser pulses of 45 femtosecond duration at a central wavelength of 796 nm. This laser system is based on chirped pulsed amplification technique and

provides a pulse energy ~ 450 mJ after the pulse compressor stage. However present set of experiments were carried out at around 150 mJ of energy. The evacuated beam transport line following the pulse compressor has the provision for varying the polarization of laser pulse and beam positioning measurements. The laser pulses were focussed on thin solid aluminum slabs placed at the center of an evacuated(10^{-4} mbar) octagonal chamber, using an AR coated plano-convex lens with focal length $f = 50$ cm, generating intensities $\sim 10^{17-18}$ W/cm². The experimental setup is schematically shown in Fig. 4.7.

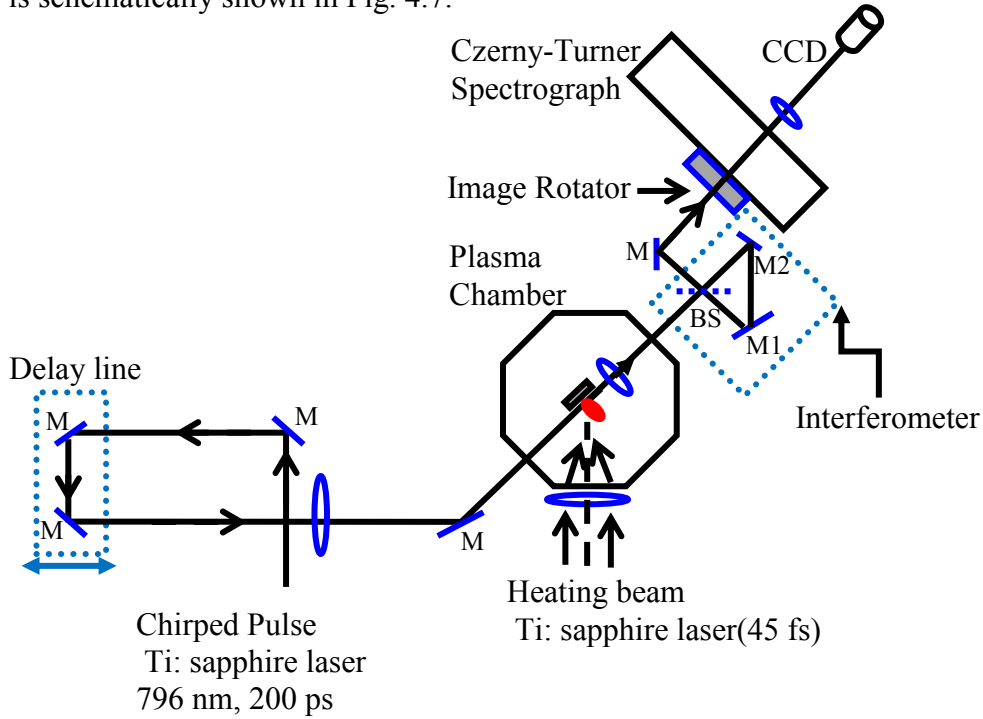


Figure 4.7 : *A Schematic of the experimental setup for the shadowgraphy and interferometry measurements^b*

4.4.1 Setup for Shadowgraphy Measurements

For shadowgraphy experiments, the interferometer setup shown in dotted lines (in Fig. 4.7) and the folding mirror M, were not used. The targets were kept at a small angle away from normal to the heating beam in order to avoid back reflection entering the laser system. The targets were placed on a 4-axes target movement system to provide controlled movement in the

X,Y,Z directions, in addition to rotation of the target in the X-Z plane. This was to ensure that the laser pulse was irradiating a fresh region of the target in each laser shot. This system was controlled from outside using a stepper motor driver. The octagonal plasma chamber was evacuated to $\sim 10^{-6}$ mbar using a vacuum system consisting of a turbo molecular pump backed by a rotary pump. The chamber has demountable flanges for easier installation of different optical elements. A telescope was attached to the plasma chamber to view magnified image of the target interaction region. It also ensured that the target was precisely positioned at the centre of the plasma chamber.

In order to generate a probe laser pulse with well defined chirping, a portion of laser beam was split using a pellicle beam splitter placed just after the last amplifier i.e. before the pulse compressor. The probe laser pulse duration was ~ 200 ps (FWHM). The reflectivity of this pellicle was around 16%. The wavelength ' λ '- time ' t ' relation of this probe pulse was obtained from the streak camera, as described in the previous section. The chirp factor was estimated as 10 ps/nm. In order to observe the plasma evolution at different time delays, one must introduce known temporal delays between the probe pulse and the main pulse. This was achieved by first calibrating the optical streak camera as described in the previous section and then set up the delay line for different delays. The probe beam was passed tangential to the target surface. By using the rotational movement of the target holder it was always ensured that the probe beam is always tangential to the front surface of the target. As an additional caution, only thin aluminium slabs of small width (~ 1 mm) were selected as targets to ensure minimum blocking of the expanding laser plasma by the shadow of the front surface.

In the shadowgraphy experiments, the aim was to observe temporal evolution of the plasma expansion to estimate the plasma velocity. In an expanding plasma, strong density

gradients are present in the radially outward direction. It is known that the refractive index of the plasma varies with the density, and also a laser pulse of wavelength $\lambda_L(\mu\text{m})$ can propagate only up to a plasma region with density known as the critical density (n_c) expressed as $n_c = 1.1 \times 10^{21} \lambda_L^{-2} (\mu\text{m})/\text{cm}^3$. Thus the movement of the over dense region generates a shadow moving with time across the cross-section of the transmitted probe beam. In the case of the snap shot shadowgraphy technique, the recorded two dimensional image will provide a time integrated (over the duration of the pulse) shadow at that delay, smearing all the temporal evolution information. However, in the case of a chirped pulse, since the wavelength of the probe pulse is changing with time throughout the duration of the laser pulse, one can get time resolved information by spectrally dispersing the beam using a spectrograph. This was achieved by imaging the plasma plane with a plano-convex lens ($f = 2 \text{ cm}$, $f/1$) on to the entrance slit of a Czerny-Turner type spectrograph. Although the CVI DigiKröm 480 1/2 m is a monochromator, by removing the exit slit, it was operated in the spectrograph mode. The magnification of imaging setup was $\sim 50X$. In order to record the movement of the shadow region in the plasma, it was necessary to image the plasma such that expansion was in a direction parallel to the entrance slit ($100 \mu\text{m}$ wide, 1.5 cm height). For this, the plasma image was rotated by 90° using an image rotator (consisting of 4 prisms). The output spectrum was recorded using a CCD camera with a demagnification factor of $2.2X$. In the recorded spectrum, the temporal information is along the direction of spectral dispersion, whereas the spatial information of the plasma expansion is along the height. A grating of 600 grooves/mm was used in the spectrograph for the present shadowgraphy experiments providing a linear dispersion of 3.2 nm/mm .

4.4.2 Setup for Interferometry Measurements

The experimental setup for the Chirped Pulse Interferometry (CPI) measurements is mostly similar to the shadowgraphy setup described in the previous section. An additional element, a cyclic lateral shearing interferometer was introduced in the path of the transmitted probe beam between the plasma and the spectrograph. This facilitates electron density measurements from the interference fringe shifts.

Different optical schemes are available for generating interference fringes from a probe beam passing through the plasma. In many of these schemes, the probe beam is split into two components and one of these acts as a reference beam and the other component is passed through the plasma and then made to interfere with the reference beam by overlapping them. However, one may face difficulty in generating a good interference fringe pattern in view of the short temporal coherence length of the Ti-sapphire laser probe beam due to its large spectral width. Alternately, interferometers based on the principle of polarization, for example, a Wollaston prism interferometer may be used which offer equal path lengths for the two components. However, they are not flexible in varying the parameters like fringe spacing and orientation. We have used another type of cyclic shearing interferometer which is simple to construct, offers flexibility in adjusting fringe spacing and orientation, and also makes both the components travel exactly the same optical path. At the same time, overlap of the two components should provide the shift in fringe pattern due to the presence of plasma. This can be accomplished by ensuring that the region of the probe beam containing the plasma is made to interfere with some other plasma-free region (a region away from plasma). This plasma free region acts as reference wave front interfering with the region of wave front modified by the plasma. This results in a fringe

shift from which electron density of the plasma can be estimated. In order to satisfy this condition, sufficiently large (compared to the plasma dimensions) lateral shear needs to be given.

A cyclic interferometer consists of three optical components a beam splitter and two 100% reflecting mirrors as shown in Fig. 4.8. A pellicle beam splitter BS (50/50) splits the incident beam into two beams of equal amplitude. These two components are incident on mirrors M1 and M2. The transmitted component (T) follows the path M1, M2 and is then incident on the beam splitter. 50% of this component is again transmitted by beam splitter BS (component labelled as TT) towards a spectrograph. Similarly, the reflected component (R)

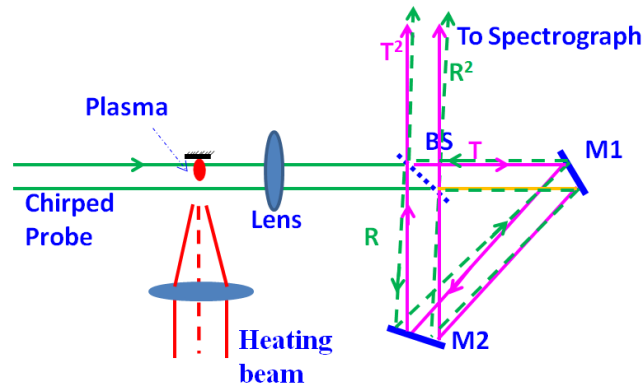


Figure 4.8 : *A schematic diagram of a cyclic interferometer*

follows the path M2, M1, and 50% of this is reflected by BS once again (RR), which then travels towards the spectrograph. Thus both the components trace a cyclic path, as shown in Fig. 4.8. It can be seen that tilting any mirror (M1 or M2) will affect both the components of the probe beam, whereas any tilt of the beam splitter BS deflects only the reflected component. Secondly, the angular tilt and the lateral shear are related to each other and cannot be varied independently. The angular tilt of the beam splitter BS will change the angle between the two

beams and generate the interference fringes with the fringe width inversely related to the angle between the two beams. Initially both the components are made parallel to each other. This is done by adjusting the beam splitter angle continuously in a direction such that the fringe width increases. Finally when both the wave fronts are parallel to each other, the fringes will disappear and constant intensity all over the beam cross-section will be seen. Starting from this, the angle of the beam splitter is varied only in horizontal (or vertical) direction until suitable lateral shearing and fringes of suitable width are achieved. The orientation of the fringes is perpendicular to the direction of the angular tilt and the interference maxima (minima) will occur whenever the path difference between the two wave fronts is equal to an integral multiple of the wavelength λ (an odd multiple of $\lambda/2$). The lateral shearing can be estimated by placing a sharp object (say a small straight pin) at the plasma plane. The direction of the fringes is chosen based on the direction of the entrance slit of the spectrograph.

Like in shadowgraphy experiments, in these experiment also, a small portion of the interferogram was imaged onto the vertical entrance slit of the spectrograph with an optical magnification of $\sim 80X$ to get higher spatial resolution. The width of the generated interference fringes was $\sim 2.6 \mu\text{m}$ (at the plasma plane). In order to record the temporal evolution of the fringe shift (and thus change in the plasma density), the fringes should be in the horizontal direction i.e. perpendicular to the entrance slit of the spectrograph. In addition it is also desired to obtain density profiles at different distances from the target surface. In order to meet both these requirements, the interferometer was set up to generate fringes parallel to the target surface (vertical). Then an image rotator was used to rotate this by 90° so that plasma expansion is in the downward direction, i. e. along the entrance slit of the spectrograph, and the interference fringes are perpendicular to this.

4.5 Results and Discussion

4.5.1 Shadowgraphy Measurements

These experiments were carried out by producing plasma with a femto second laser pulse of 150 mJ energy and 45 femtosecond duration. The laser pulses were focussed onto thin (~ 1 mm wide) aluminium slab targets using an AR coated plano-convex lens with focal length $f = 50$ cm. The typical laser intensities on the target were $\sim 1 \times 10^{17-18}$ W/cm². The vacuum in the plasma chamber was $\sim 10^{-4}$ mbar. A typical spectrum of the chirped probe beam passing through the target region is shown in the Fig. 4.9. The probe beam is positively chirped and thus the direction of decreasing wavelengths (from right to left) indicated the increase in time i.e. the left part of the figure indicates later part of the probe pulse compared to right part. The direction of the plasma expansion (i.e. along the target normal) is downwards along the entrance slit of the spectrograph and the target surface is closer to the top edge of the shadowgram.

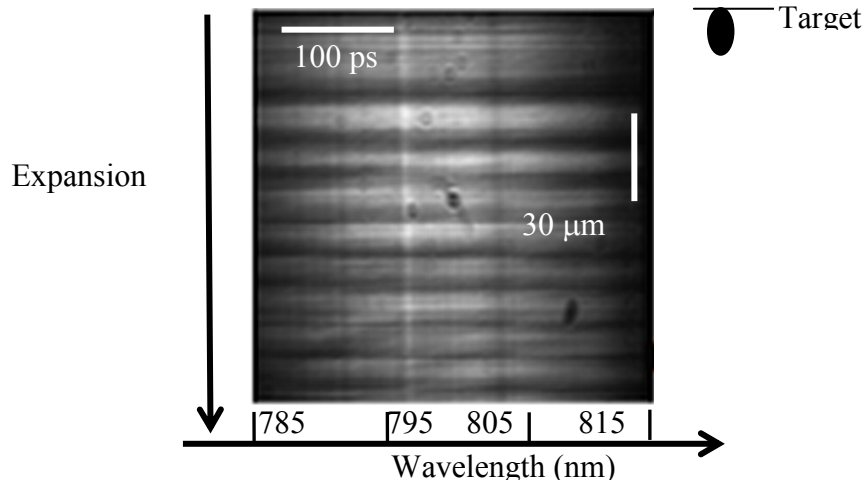


Figure 4.9 : *Shadowgram (spectral domain) of probe pulse in absence of plasma^a*

The shadowgram in Fig 4.9 comprises of wide horizontal fringes which appear due to edge diffraction effect. Under ideal imaging conditions, when these fringes are absent, the

spectrum of the probe beam after the target region will contain a dark region (shadow) in the top portion and a bright (transmitted) region in the lower portion. As the present setup uses a lens of short focal length (2 cm) to image with high magnification factor (50X - 80X), these diffraction fringes will appear due to the finite extent (lateral) of the plasma. However, these diffraction fringes do not pose any problem in measurement of the plasma expansion. In fact, as shown later in the interferometry experiments, the shift in these fringes can also be used to estimate plasma expansion velocities simultaneously.

When the laser irradiates the target surface, a rapidly expanding plasma is generated. This outwardly expanding plasma will have a density gradient which will evolve with time. As described in section 1.3.1, the refractive index μ of the plasma decreases with increasing plasma density [$\mu = (1 - n_e/n_{cr})^{1/2}$] where n_{cr} is the critical density. For the present probing wavelength (800 nm), the critical density is $\sim 1.7 \times 10^{21} \text{ cm}^{-3}$. In fact, even before the critical density, the probe beam will get strongly refracted by the plasma and as the refraction increases, less amount of light corresponding to that density region will reach the detector, depending upon the collection solid angle of the imaging lens. Thus, even in the sub-critical density regions, shadow will be formed as only a small fraction of the refracted light will be collected. As the plasma expands outwards, this shadow region moves forward. Different components of the spectrum will see opaque region at different distances from the target surface, so that the spectrum of the transmitted probe beam will show the movement of this opaque region. Thus, by recording the spectrum, the plasma expansion information can be obtained in a single laser shot. A typical spectrum of the transmitted probe beam recorded in the spectrograph is shown in Fig. 4.10.

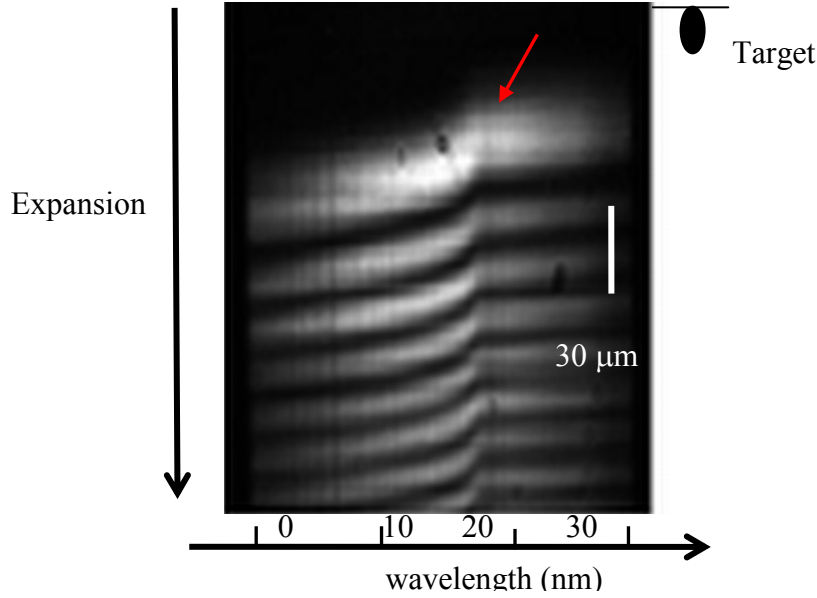


Figure 4.10 : *Shadowgram (spectral domain) of the probe pulse in presence of plasma^a*

As discussed in the previous paragraphs, the fringes present are generated due to diffraction. In the absence of the plasma only horizontal fringes are recorded indicating a stationary target (Fig 4.9). When the laser plasma is produced, the position of the fringes was also moving in time as the critical density surface (acting like a knife edge) moves forward in time as shown in Fig. 4.10. The interface between the shadow and bright region will give information about the movement of shadow which is in turn related to the movement of the outwardly expanding plasma. We have tracked the position of the upper edge of the first fringe at the top (indicated by a red arrow in Fig. 4.10) at different points along the spectrum. By using an imaging software PROMISE (developed at RRCAT) the (x, y) coordinates of the top edge are recorded manually (moving the cursor to different points on this edge). The x coordinates are converted to probe delay in pico seconds by knowing the pixels to time conversion factor. This factor is estimated by recording the spectrum of the chirped laser pulse (FWHM : 20 nm corresponding to 200 picoseconds FWHM in time). A conversion factor 0.51 picosecond per

pixel was arrived at. Similarly in the orthogonal direction, a conversion factor of $0.24 \mu\text{m}$ (plasma plane) per pixel was estimated by moving the target surface and recording the images.

Fig. 4.11 shows the spatial coordinates of the moving shadow region of the laser produced plasma with time. The curve joining these points represents the trajectory of the plasma edge. The slope of the trajectory at each point provides the instantaneous value of the expansion velocity. In order to obtain points at regular intervals cubic spline interpolation was used. The slope is expressed as $\Delta(\text{spatial expansion}) / \Delta(\text{time})$ at each point and its preceding point. The evolution of the plasma velocity with time at some discrete points was thus calculated. The observed time window (not FWHM) for our experimental conditions is ~ 300 ps.

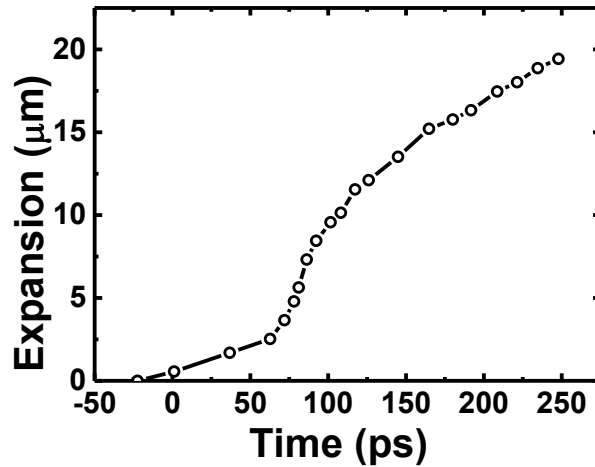


Figure 4.11 : *Temporal variation of the plasma expansion^a*

Figure 4.12 shows the variation of the expansion velocity with time. The horizontal axis denotes the delay between the probe and the heating laser pulses. It is seen that the expansion velocity first increases with time and after reaching a maximum value of $\sim 1.8 \times 10^7$ cm/s, it starts falling and reaches a steady value.

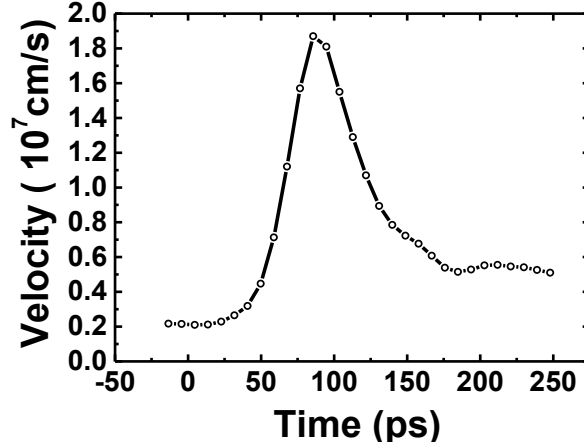


Figure 4.12 : Temporal variation of the plasma expansion velocity^a

The fast variation in the expansion velocity in Fig 4.12 may be qualitatively understood as follows. The femtosecond heating laser pulse has a small ns pre-pulse appearing approximately 2 ns before the 45 femtosecond laser pulse. This pre-pulse creates a background plasma which expands slowly. After the femtosecond laser pulse is incident, this pre-plasma gets rapidly heated and a sudden variation in the plasma expansion velocity as observed in the Fig. 4.12 above. The time resolution of the measurement was ~ 8 ps, limited by the slit width ($\sim 100 \mu\text{m}$) of the spectrograph, dispersion of the grating, and the bandwidth of the probe pulse.

4.5.1.1 Scaling of plasma expansion velocity with laser intensity

In order to study scaling of plasma expansion velocity with laser intensity, the focal spot size was varied in steps, keeping the laser energy fixed. The focussing was optimum when the lens was placed at 19 mm (relative) on the movement system. From this position, the lens was moved by 2mm, 5mm and 10mm (towards the target). The focal spot sizes $\omega(Z)$ at these displaced positions Z was estimated from $\omega(Z) = \omega_0 \{1 + (Z / Z_R)\}^{0.5}$ where Z_R is the Rayleigh length ($\pi \omega_0^2 / \lambda$) and ω_0 is the beam waist. In earlier experiments the beam waist was measured to be $\sim 18 \mu\text{m}$. The corresponding laser intensity on the target were $\sim 9 \times 10^{16} \text{ W/cm}^2$, 2×10^{16}

W/cm^2 and $5 \times 10^{15} \text{ W}/\text{cm}^2$ respectively compared to the peak laser intensity of $3 \times 10^{17} \text{ W}/\text{cm}^2$ at the best focus position.

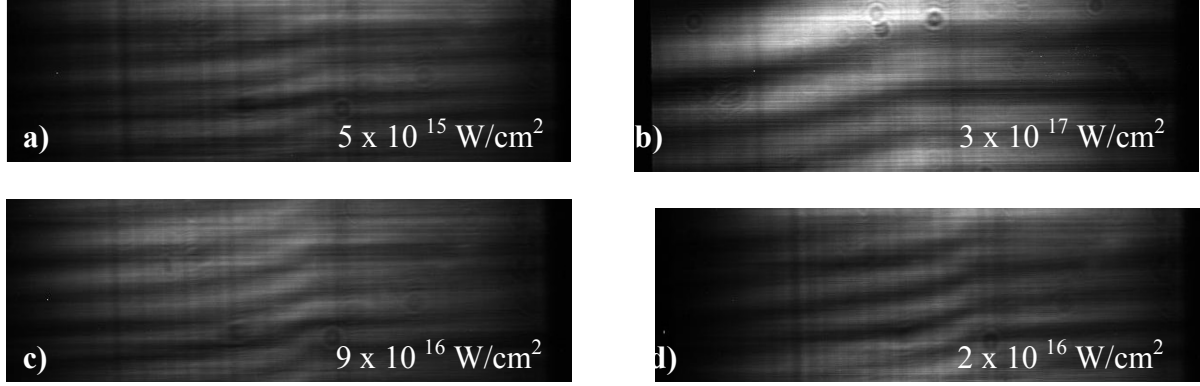


Figure 4.13: *Shadowgrams recorded at different laser intensities on the target*

The shadowgraphs taken in different focal conditions are shown in Figure 4.13. The expansion velocity profiles obtained from these shadowgrams are shown in Figure 4.14(a). The variation of the peak expansion velocity with the laser intensity is shown in Fig 4.15(b). The data is fitted with a scaling law of peak plasma expansion velocity v_{ex} with laser intensity I_L of the form of $v_{\text{ex}} \sim I_L^\alpha$. The scaling exponent α is observed to be ~ 0.2 from the results.

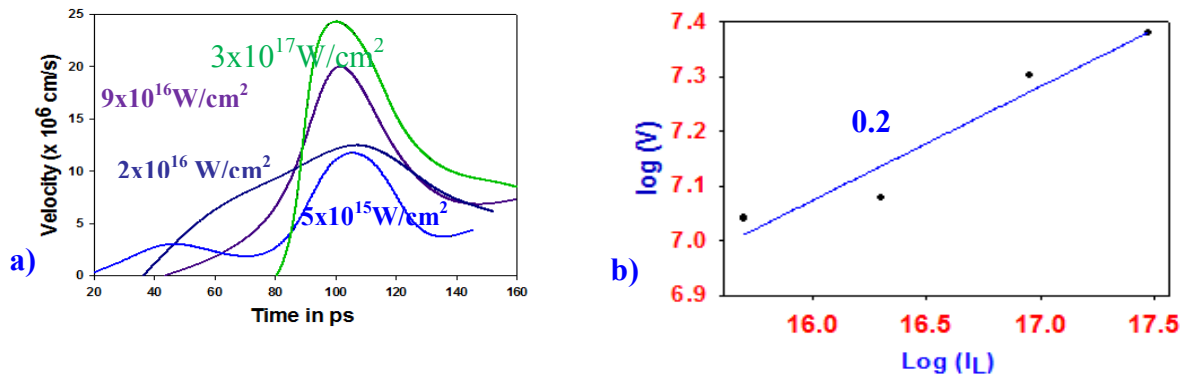


Figure 4.14 : (a) *Temporal profiles of the plasma expansion velocity for different laser intensities and (b) the scaling between peak expansion velocity and laser intensity*

The observed scaling agrees well with that expected from physical considerations. It is known that in case of femto second laser plasmas, the plasma temperature has scales¹¹⁸ with laser intensity as $(I)^{1/3}$ and the blow off velocity of the plasma is roughly at sound speed expressed as

$$C_s = \left(\frac{Zk_B T_e}{m_i} \right)^{1/2} \quad \text{--- -- 4.01}$$

In effect the plasma expansion velocity should scale with laser intensity as $\sim (I)^{1/6}$ which is close to the experimentally observed value of $I^{0.2}$.

The reproducibility of the results depends on the stability of the heating laser pulse and spatial quality of the heating and probe laser beams. The results shown in Fig 4.11 and Fig 4.12 were qualitatively highly reproducible, for instance from occurrence of peak of expansion velocity after ~ 100 ps delay (Fig 4.14), the temporal profile of the expansion velocity (Fig 4.14), and scaling behaviour of the velocity with laser intensity (Fig 4.14) described before in this section. Quantitatively there was some variation in the value of the expansion velocity over different laser shots. The expansion velocity showed a variation up to $\pm 20\%$ in different laser shots for which the laser energy was kept fixed (variation within $\pm 10\%$) and using the same focussing conditions. This may be due to shot to shot variation in the intensity distribution in the focal spot and spatial intensity profile of the probe beam.

4.5.2 Interferometric Measurements

Electron density measurements were carried out by adding a cyclic interferometer to the shadowgraphy setup. The plasma was produced using the 45 fs laser pulse at 150 mJ energy. The typical laser intensity on the target was $\sim 1 \times 10^{18} \text{ W/cm}^2$. By adjusting the pellicle beam splitter, fine vertical fringes were generated. The plasma plane was imaged on to the entrance slit of the CVI DigiKröm DK480 monochromator (used as spectrograph by removing the exit slit) and the image was rotated by 90° such that the orientation of the fringes was horizontal i.e. parallel to the spectral dispersion direction. Typical interference fringes generated with this setup in the absence of plasma are shown in Fig 4.15 below.

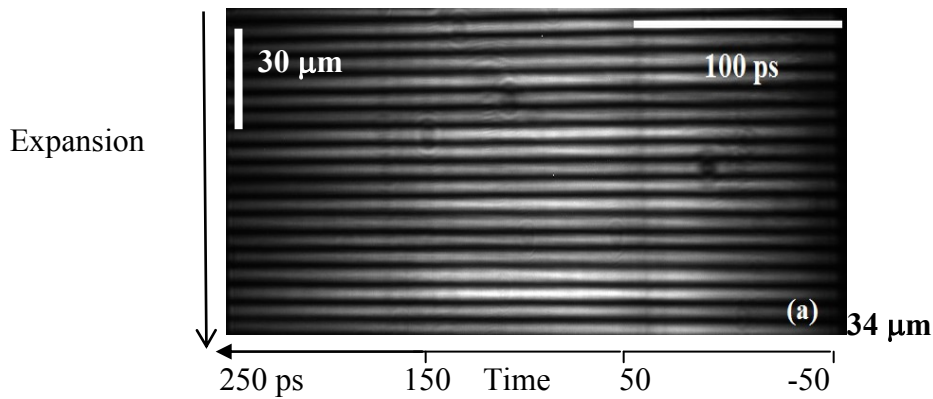


Figure 4.15 : *Interference fringes in the absence of plasma (reference)^b*

As discussed earlier in the case of shadowgraphy, with a chirped probe beam having a positive chirp the longer wavelengths (red component) will appear earlier in time compared to the shorter wavelengths (blue). Thus in these interferograms, the temporal evolution is seen from right to left. Using the measured chirp factor of $\sim 10 \text{ ps/nm}$, the recorded spectrum containing interference fringes (Fig 4.15) corresponds to $\sim 300 \text{ ps}$ in time with a probe pulse of 200 ps (FWHM).

Fig 4.16 shows the interference fringes recorded in the presence of plasma during different time intervals. The femtosecond heating beam producing the plasma serves as the zero time reference. Fig 4.16 (a) shows the interference fringes recorded for a time interval of -50ps to +250 ps. It can be seen that upto a time ~ 75 ps w.r.to the heating laser beam, the fringes are straight and fringe shift can be seen only after this. The shift in the interference fringes starts appearing only when the plasma reaches the rectangular spatial observation window which is imaged onto the spectrograph entrance slit.

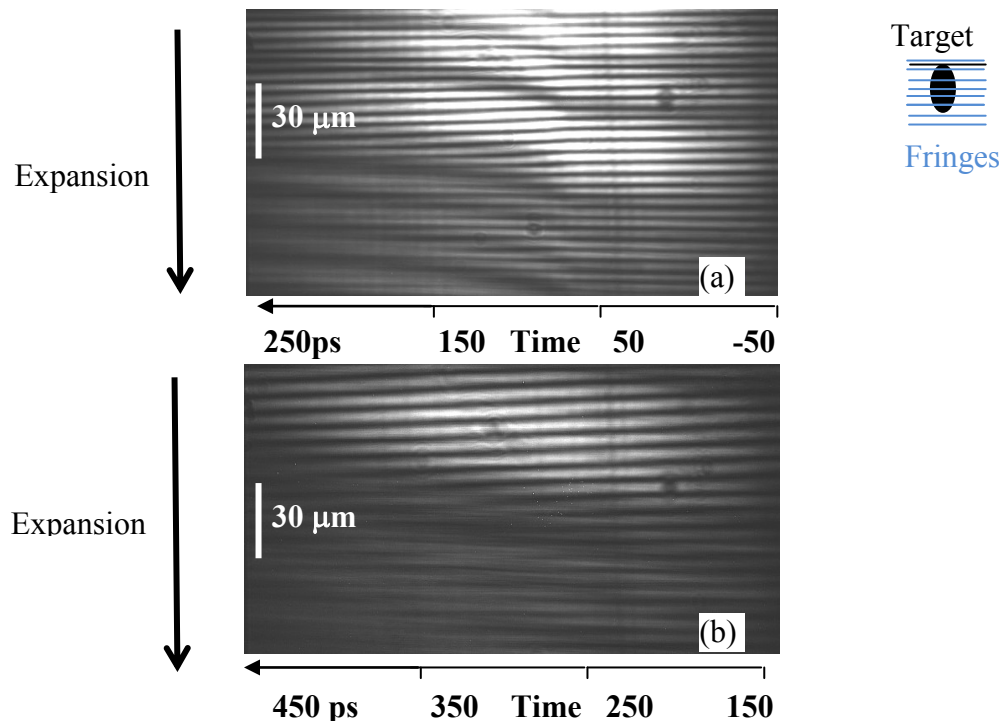


Figure 4.16 *Interference fringes at two different time delays^b*

Fig 4.16 (b) shows the interference fringes for a different time window i.e. $\sim +150$ ps to +450 ps. This shot was recorded by moving the delay line mirrors to introduce a time delay of 200 ps between the heating beam and probe beam. One can see that while the fringe shift started

appearing in Fig 4.16(a) the same increased in the later time window shown in Fig 4.16(b), as expected.

The shift in interference fringes shown in Fig 4.16 can be used to determine space and time resolved plasma density. Before we move on to the density determination, it may be pertinent to know the spatial and temporal resolutions involved. The theoretical time resolution possible with the chirped pulse diagnostics is expressed as $\Delta t \sim (t_0 t_c)^{1/2}$, where t_0 is the main pulse duration (45 fs) and t_c is the chirped pulse duration (200 ps)¹⁰⁰. Here the pulse duration after the compressor is considered and not the oscillator pulse duration, as some bandwidth is lost during amplification due to gain narrowing, thereby lengthening the compressed pulse. In the present case, the theoretical time resolution is ~ 3 ps, but due to other limiting factors like slit width of the spectrograph (100 μm in present case), the actual time resolution was ~ 8 ps. By optimizing different experimental parameters like grating and slit width etc., one can approach the theoretical resolution. The width of the interference fringes limits the spatial resolution in the plasma plane to 2.6 μm .

The plasma electron density ' n_e ' can be estimated from the variation in the observed shift ' δ ' in the interference fringes as

$$n_e = \frac{(2\pi mc^2)}{L\lambda e^2} \left[\frac{\delta}{\Delta x} \right] \quad \text{..... 4.1}$$

where Δx is the fringe width and λ is the probe wavelength. Since the fringe shift is chord integrated, the calculated values of electron density are average values assuming cylindrical symmetry which is generally applicable for laser produced plasmas. A typical electron density

variation in time is shown in Fig. 4.17. The plotted density profiles at 54 μm and 67 μm away from the target surface, for a time window of +150 ps to +450 ps (w.r.to heating laser pulse). It can be seen that at a distance of 54 μm from the target surface, the electron plasma density is continuously increasing in the window of observation. Compared to this, the electron density at a farther distance, i.e. 67 μm remains very small upto a time of 250 ps and thereafter starts increasing. As a general trend observed over several shots, the electron density closer to the target surface initially increased and then starts decreasing after certain time. In the present setup, the time window was ~ 300 ps.

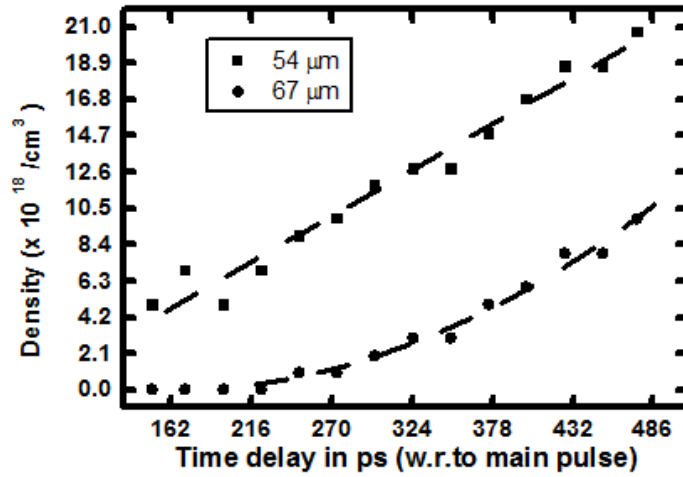


Figure 4.17 : *Temporal profile of the density at two distances from the target surface^b*

As described in the chirped pulse shadowgraphy experiment, a broad diffraction pattern could be seen in the present case also. The fine interference fringes are superimposed on this diffraction pattern which was due to diffraction from the front edge of the target surface or the moving high density front in the case of plasma^{119,120}. The movement of the diffraction pattern is nearly identical to that seen in the shadowgraphy experiments. As the plasma expands, the diffraction pattern also moves in space. From the movement of this diffraction pattern (either

minima or maxima), a continuous temporal variation of the expansion velocity of the plasma was calculated and then compared with the shadowgraphy results. Similarly, a peak expansion velocity of $\sim 1.2 \times 10^7$ cm/s was also estimated from these measurements. These results are shown in Fig 4.19. The temporal expansion velocity profile, calculated from the slope of the diffraction pattern, has a FWHM of 70 ps in time. These results match with our earlier observations from the shadowgraphy experiments, but for the variation in the peak expansion velocity. This may be due to some variation in the energy of the heating laser pulse.

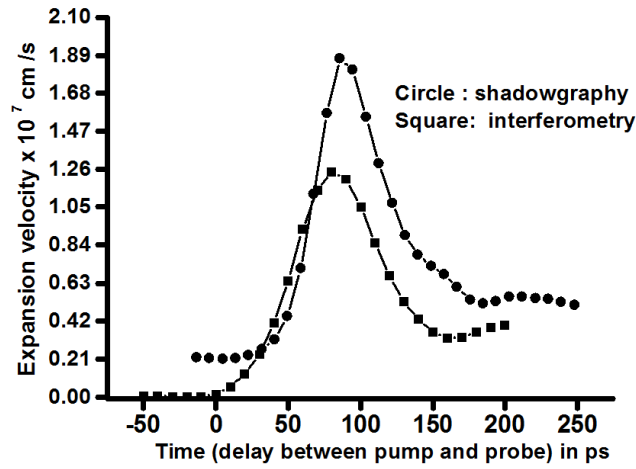


Figure 4.18 : *The temporal profile of the expansion velocity. The circles/squares show experimental data from shadowgraphy and interferometry respectively^b*

4.5.3 Advantages and disadvantages of chirped diagnostics

The chirped pulse diagnostics can provide excellent temporal resolutions compared to the diagnostics based on the streak camera. By using chirped pulses of shorter duration of few tens of ps (compared to 200 ps here) one can easily obtain a temporal resolution of < 1 ps. However, choice of the temporal resolution is to be decided by the phenomenon to be observed

and time scales over which the event is occurring. For very fast phenomena like self generated magnetic fields during laser plasma interaction processes like inverse Faraday effect or ionization processes of helium etc., one can opt for resolutions ranging from hundreds of fs to few ps. However, the time window also becomes short in this case. On the other hand, for hydrodynamic phenomena like plasma expansion etc., the required temporal resolutions can be tens of ps as in the present case. As an optimum condition, a probe pulse of hundreds of picoseconds can be used to cover longer time window and by improving the experimental conditions like entrance slit width of the spectrograph, the resolution can be improved.

Secondly, one has to use very high magnification factors in the imaging systems (like 80X used in our case of interferometry) to observe slower phenomena. A plasma expanding with a velocity of 10^7 cm/s moves only by $\sim 1 \mu\text{m}$ in 10 ps and $\sim 20 \mu\text{m}$ in 200 ps time window. So to observe this kind of spatial movements with good resolution, it is necessary to use high magnifications. However, increasing magnification has a disadvantage also. With such high magnification factors, the typical slit height of 1 cm correspond to very a small distance ($12 \mu\text{m}$) in the plasma plane. So unless the heating beam energy is quite stable, one may usually encounter either a fully shadow region or fully transparent (as the plasma would not reach the window being observed / imaged) most of the times. Thus the energy stability of the laser system is a crucial factor here. One possible solution is to use a variable stretcher different from the one used as part of femtosecond laser system and vary the chirping factor during the experiments.

It would also be interesting to compare the time resolved diagnostics using chirped pulse measurements with the ones using optical streak cameras. While using the streak cameras, there is a requirement for a long duration laser pulse to probe the plasmas. For this, one may have to synchronize two different laser systems, one for the heating beam and another for probing. Then

one can use different sweep speeds of the streak camera to study the plasma evolution with the desired time resolution. However, when one uses a longer time window, the time resolution does suffer. For illustration, the results from earlier experiments carried out for time resolved plasma densities using an optical streak camera are shown in Fig 4.19 below. Figure 4.19 b shows the

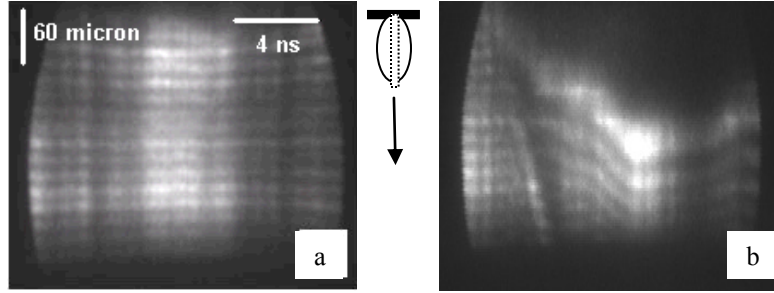


Figure 4.19 Time resolved interferometry with an optical streak camera (a) without and (b) with plasma^c

change in the interference fringe shift with time and (a) shows the reference fringes in absence of plasma. It can be seen that as the plasma is forming i.e. at the transition point between the straight line fringes and shifted fringes, the tracking of the fringe shift becomes difficult at times. In comparison, the chirped diagnostics cannot offer long time windows but the temporal resolution are much better here down to sub ps if required. Only the main differences between the diagnostics using chirped pulses and optical streak camera are given here without going into details. More details about the diagnostics using the streak camera can be found in reference⁹⁶.

4.6 Conclusions

Chirped pulse diagnostics has been developed for shadowgraphy and interferometry to study the temporal evolution of the plasma expansion velocity and plasma densities. A peak expansion velocity of 1.8×10^7 cm/s, with the velocity profile of 70 ps FWHM has been

observed. The scaling between laser intensity and expansion velocity have been obtained as $(I)^{0.2}$ by changing the focal spot size. The chirped pulse interferometry experiments using a cyclic interferometer have been carried out to obtain the temporal evolution of the plasma density, at different distances from the target surface. It is also seen that one can use the diffraction pattern superimposed on the interference fringes to obtain the peak plasma expansion velocity and the temporal velocity profiles simultaneously. These velocity values obtained from interferometry match quite well with the results obtained from chirped pulse shadowgraphy experiments.

Permissions for reprinting figures

^a Reprinted from *Chirped pulse interferometry for time resolved density and velocity measurements of laser produced plasmas* by Prasad, Y. B. S. R., Barnwal, S. , Naik, P. A., Chakera, J. A., and Gupta, P. D., Journal of Applied Physics 110, 023305 (2011), DOI:<http://dx.doi.org/10.1063/1.3610792>, with the permission of *AIP Publishing*.

^b Reprinted from *Chirped pulse shadowgraphy for single shot time resolved plasma expansion measurements* by Prasad, Y. B. S. R., Barnwal, S., Naik, P. A., Chakera, J. A., Khan, R. A., and Gupta, P. D., Applied Physics Letters 96, 221503 (2010), DOI:<http://dx.doi.org/10.1063/1.3442510>, with the permission of *AIP Publishing*.

^c Reprinted from *Simple interferometer for space and time resolved density measurements of laser produced plasmas* by Prasad, Y. B. S. R., Naik, P. A., Kumar, A. and Gupta, P. D., Review of Scientific Instruments 77, 093106 (2006), DOI:<http://dx.doi.org/10.1063/1.2349596>, with the permission of *AIP Publishing*.

Chapter 5 : Detection of Self Generated Magnetic Fields

5.1 Introduction

Large scale magnetic fields (several kG to MG) are generated during laser-plasma interaction at high laser intensities⁸⁸. The physical mechanisms for generation of these spontaneous magnetic fields differ with laser pulse duration. In the case of laser pulses of nano - picosecond (ns-ps) duration, phenomena like thermo-electric effect¹²¹, resonance absorption³³, and target discontinuities¹²² play dominant role in magnetic field generation. However, in the case of femto-second (fs) laser plasmas, phenomena like inverse Faraday effect^{26,123}, strong hot electron generation³⁶, relativistic channel formation³⁶, and self focussing¹²⁴ play major role in generation of such large scale magnetic fields. This is the precise reason why many experiments were conducted to detect exact location of these fields as signature for these phenomena^{93,125}. It is well known that these fields can greatly affect the laser plasma interaction process by inhibiting thermal conduction¹²⁶, generation of hot electrons^{126,127}, and thereby lead to plasma instabilities¹²⁸. Thus, studying the generation and evolution of these magnetic fields with space and time, is of great importance in the case of laser produced plasmas. Different types of experimental techniques had been used to detect these fields. Drouet *et al* had used a small inductive probe to measure the magnetic fields generated when copper targets were irradiated by 1.7 ns 4 J CO₂ laser pulses¹²⁹. In order to detect the fine structure of these fields, Sakagami *et al* had used the magnetic tape method¹³⁰ at laser intensities of 10^{12} W/cm². Using Zeeman effect, Briad *et al* had detected toroidal and axial magnetic fields of 0.35 and 0.5 MG respectively in carbon plasmas with a 0.25 μ m laser beam¹³¹. It is known that these techniques have some limitations. The current probes and magnetic tapes can only provide space averaged information

about the magnetic fields since they are placed at some distance from the interaction region. Secondly, these techniques were unable to obtain information from the areas closer to the critical density region where these fields are generated. It should also be noted these techniques could only provide time integrated measurements of magnetic fields.

In 1975, Stamper *et al* had used Faraday rotation technique to detect the self generated magnetic fields in laser produced plasmas⁸⁸. In this method, a linearly polarized laser pulse is passed through the laser plasma region. Due to magneto-optic Faraday effect, the plane of the polarization of the electromagnetic wave (probe laser beam) passing through the plasma in which magnetic fields are present, gets rotated by an angle proportional to the local plasma density n_e and the amplitude of magnetic field \mathbf{B} at that location. Only the component of magnetic field along the laser probe propagation direction is to be considered here. The rotation angle is expressed as¹³²

$$\theta(\text{deg}) = 1.5\lambda_p^2(\text{microns}) \int \frac{n_e(\text{cm}^{-3})B_z(\text{MG})dx(\text{microns})}{10^{21} \sqrt{1 - \frac{n_e}{n_c}}} \quad \dots 5.1$$

where ' B_z ' = $\mathbf{B} \cos \phi$ is the component of magnetic field along the probe beam propagation direction (tangential to the target surface), and ' λ_p ' is the wavelength of the probe beam. For a toroidal magnetic field, ϕ varies from 0° at the top and bottom edges of the plasma, to 90° at the level of the axis of the heating beam. Here the n_e is the electron density and n_c is the critical density for the probing beam expressed as

$$n_c = \frac{m\omega^2}{4\pi e^2} \quad \dots\dots 5.2$$

where ω is frequency of the laser. The rotation angle at each point across the cross section of the probe beam depends on the density and the magnetic field at that location. Thus, this technique provides the spatial profile of the magnetic fields. It can be seen that by passing a probe beam tangential to the target surface (i.e. perpendicular to the heating beam) one can detect toroidal magnetic fields. By varying the probe beam direction, it is always possible to detect magnetic fields in different configurations (like axial fields). By using a short duration probe pulse compared to the heating pulse, the temporal evolution of these magnetic fields can also be obtained^{125,126}.

From the above expression, it is clear that with a prior knowledge of the electron density distribution, the amplitude of the self generated magnetic field at different locations in the laser produced plasma can be estimated. Initial experiments had assumed some standard electron density distribution to calculate the magnetic fields. However, since laser plasmas have strong density gradients, this assumption gave only an order of magnitude estimate of the magnetic fields. In order to accurately estimate these fields, simultaneous measurement of the electron density along the propagation direction of the probe beam, is essential. Similarly, any spatial non-uniformities, if present in the probing beam, will lead to corresponding variation in the profile of transmitted beam, which one may wrongly interpret as effect of magnetic fields. Thus it is important to have a knowledge about the spatial profile of the probe beam. This will also help in estimation of losses due to refraction and scattering of the probe beam in the laser plasma. Otherwise these losses lead to erroneous estimation of the magnetic fields. So, simultaneous space resolved measurement of Faraday rotation angle, electron density, and the transmitted probe beam profile passing through the plasma, helps in accurate detection of the self generated magnetic fields. We have carried out experiments in our laboratory to detect these

magnetic fields using a three-channel polaro-interferometer at Laser Plasma Division, RRCAT in collaboration with Laboratory of Plasma Diagnostics, P.N. Lebedev Physical Institute, Moscow, Russia. The results obtained in this experiment are described here. Different mechanisms that can lead to generation of these magnetic fields are described earlier in Chap.1. Section 5.2 describes the optical setup of the three-channel polaro-interferometer generating three different channels for recording the Faraday rotation angle, the plasma density, and the spatial profile of the probe beam, respectively. Section 5.3 describes the experimental setup. The results and analysis of data are given in section 5.4. The rotation angle and the electron density obtained are chord integrated along the propagation direction of the probe beam. ABEL inversion technique was used to obtain space resolved information from these chord integrated fringe shifts, and rotation angles. This technique is described in Appendix B. Two programs have been written in MATLAB to calculate the magnetic fields. These programs and their description are included as Appendix C.

5.2 Optical setup of a three channel polaro-interferometer

In the earlier section we have described the need for simultaneously recording the Faraday rotation, interference fringes and spatial profile of the probe beam in order to estimate the self generated magnetic field accurately. There were some earlier attempts that have generated these channels and recorded using three different CCD cameras. In order to simplify this further and record using a single detector a new optical setup of a 3-channel polaro-interferometer is presented here. In this setup, the probe beam is split into three beams of equal amplitude using a pair of calcite wedges (birefringent) and a pair of Glan prisms. A schematic ray diagram of the 3 channel polaro interferometer is shown in Fig. 5.1.

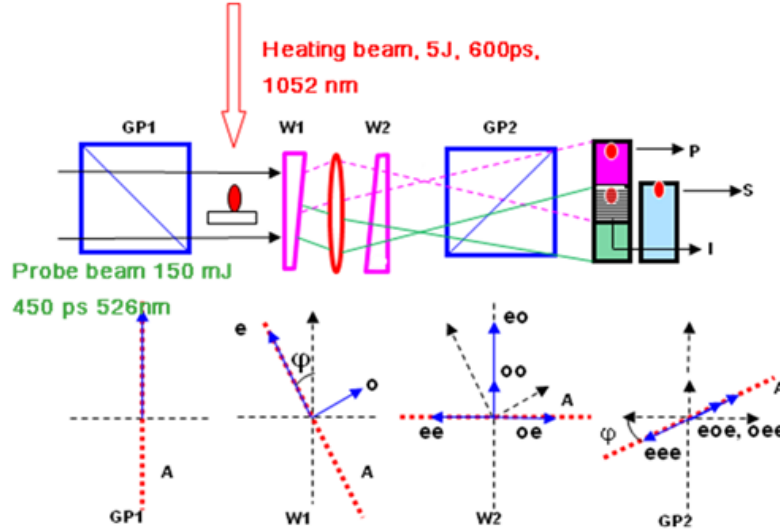


Figure 5.1: A schematic of optical setup of the three channel polaro interferometer¹

The probe beam passes through a Glan Prism (15 mm x 15 mm) GP1 to generate a linearly polarized light. (This will improve the contrast of probe beam even if the input is already polarized). After this, the probe beam passes through the laser produced plasma tangential to the target surface in which mega-gauss order magnetic fields are generated. Now this probe beam is made to pass through a calcite wedge W1 (~ dia 20 mm), which is kept at a small angle ‘ φ ’ called as de-crossing angle ($< 5^\circ$) with respect to the optic axis of Glan prism GP1, to split the beam into two components, extraordinary “e” and ordinary “o” expressed as (see Fig. 5.1)

$$I_o = I \sin^2 \varphi \quad \dots\dots 5.3(a)$$

$$\text{and } I_e = I \cos^2 \varphi \quad \dots\dots 5.3(b)$$

For practical convenience, both Glan prism and calcite wedge are oriented such that these components are split in the horizontal direction. The de-crossing angle ‘ φ ’ is introduced as it helps in determining the direction of the magnetic field and it is kept quite small, as it decides the

sensitivity of the device. Depending upon the direction of the magnetic field, the sign of the rotation angle will change and this will result in either increase or decrease in the intensity of the transmitted probe beam. Secondly, by keeping the de-crossing angle small, the change in intensity of the transmitted beam ($\propto \sin^2(\varphi \pm \theta)$) can be clearly seen with a weak background. On the other hand, if one uses a large de-crossing angle the background itself will be quite strong and it will be really difficult to observe any further change in this due to the presence of magnetic fields.

Now by using another calcite wedge W2 (\sim dia 20 mm) whose optic axis makes 90° w.r.to the GP1, these two components are further split in to “e” and “o” components. The wedge angles were chosen to be $\sim 4^\circ$ and 6° for W1 and W2 respectively. The wedge angles of W1 and W2 are chosen such that there is some finite overlap between the components generated in the horizontal direction (small angle for W1) and well separated images in the vertical direction (slightly higher angle for W2).The wedge angles were chosen by taking into account the distance between the calcite wedges and the detectors, which in turn depends on the plasma chamber size. Additionally, both these calcite wedges are followed by glass wedges with similar wedge angle, in opposite direction to minimize the total angular separation and keeping them within the detector area (i.e., within the CCD Chip area). The intensities of these four beams are :

$$I_{oe} = I \sin^2 \varphi \cos^2 \varphi \quad \dots\dots 5.4(a)$$

$$I_{oo} = I \sin^2 \varphi \sin^2 \varphi \quad \dots\dots 5.4(b)$$

$$I_{ee} = I \cos^2 \varphi \sin^2 \varphi \quad \dots\dots 5.4(c)$$

$$I_{eo} = I \cos^2 \varphi \cos^2 \varphi \quad \dots\dots 5.4(d)$$

Out of these four, the I_{oo} component becomes very weak due to the presence of two $\sin^2\phi$ terms and can thus be neglected as the de-crossing angle ' ϕ ' is usually kept small. In the other three channels, the intensities of the I_{oe} and I_{ee} components are equal but much smaller compared to the third component I_{eo} due to the $\sin^2\phi$ term. Since our aim is to record all the three channels using a single detector, the intensities of all the three channels have to be nearly same. In order to achieve this, a second Glan polarizer GP 2 with its optical axis perpendicular to W1 is used. This will strongly attenuate I_{eo} component whereas the other two components I_{oe} and I_{ee} will pass through with little attenuation. The transmitted intensities of these three components after the Glan polarizer GP 2 are

$$I_{oe} = I \sin^2\phi \cos^2\phi \cos^2\phi \quad \dots 5.5(a)$$

$$I_{ee} = I \cos^2\phi \sin^2\phi \cos^2\phi \quad \dots 5.5(b)$$

$$I_{eo} = I \cos^2\phi \cos^2\phi \sin^2\phi \quad \dots 5.5(c)$$

Now in the presence of magnetic fields generated in the laser produced plasmas, the polarization plane of the input probe beam will be rotated by an angle ' θ ' due to Faraday magneto optical effect. In this case the intensities of the three components after Glan Polarizer GP2 in the above equation gets modified as:

$$I_{oe} = I \sin^2(\phi \pm \theta) \cos^2\phi \cos^2\phi \quad (\text{Channel -1}) \quad \dots 5.6(a)$$

$$I_{ee} = I \cos^2(\phi \pm \theta) \sin^2\phi \cos^2\phi \quad (\text{Channel -2}) \quad \dots 5.6(b)$$

$$I_{eo} = I \cos^2(\phi \pm \theta) \cos^2\phi \sin^2\phi \quad (\text{Channel -3}) \quad \dots 5.6(c)$$

Among these three channels it can be seen that only the first channel with a $\sin^2(\phi \pm \theta)$ term is sensitive for any small change in ' θ '. Hence this channel is referred to as Faraday channel. The other two channels with a $\cos^2(\phi \pm \theta)$ term are insensitive to small changes in ' θ '.

Since the width of the probe beam along the direction of plasma expansion is quite large (4 mm) some part of it will pass through the plasma free region. Through overlap of plasma region of channel 2 with a plasma free region of channel 1, interference fringes are produced which are used for density measurements. With this setup, fringes of $\sim 14 \mu\text{m}$ width (at the plasma plane) were obtained. The channel 3 is used as a reference in comparison with Faraday channel while estimating the magnetic fields to account for any intensity variations in the spatial profile of the probe beam. More details of the optical scheme and the principle of operation of this device can be found here.¹³³

It can also be seen that in the present optical configuration, only rotation due to Faraday effect can be measured as the probe is passing tangentially to the laser plasma. By using obliquely incident probe beam at different angles with respect to the main beam, the polarization changes due to Cotton Mouton effect¹³⁴ can be detected. However, due to experimental constraints this was not carried out in the present case.

5.3 Experimental Setup

The experiments were conducted using the high power Nd:glass ($\lambda = 1053 \text{ nm}$) laser system whose detailed description is given in Chapter 2. The commercial oscillator (EKSPLA) uses SBS-pulse compression technique and provides a laser pulse with duration adjustable from 500 ps -1500 ps. This oscillator output is further amplified using a set of amplifiers, image-relay cum spatial filters, and Faraday isolators. For the present experiments, the output was taken after the amplifier A6 stage. The present experiments were conducted at a laser energy of $\sim 5 \text{ J}$ in 600 ps. A photograph of the plasma chamber is shown in Fig. 5.2.

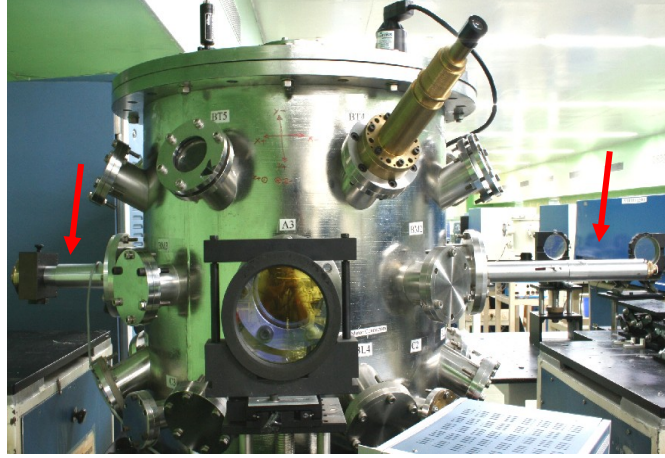


Figure 5.2: *A photograph of the plasma chamber. Arrows show the polaro-interferometer mounted on the side ports*

The long horizontal tube (shown in Fig. 5.2) connected to the side port on the right side contains some imaging optics and the Glan prism. This tube holds a rotatable rectangular aperture of size 10 x 5 mm (at the right extreme), which is imaged onto the plasma plane ($\sim 4\text{mm} \times 2\text{mm}$). This acts as a reference frame in which the plasma region is to be contained. By illuminating with a collinear He-Ne laser and this aperture as visual guiding frame, other optical elements like wedges, Glan prism, and CCD detector can be precisely aligned. While aligning these optical elements, a fine pinhole was placed at the entrance plane on the face of this rectangular aperture. The tube on the right side contains the calcite wedges (W1, W2), Glan prism (GP2) and a lens to image the plasma plane onto the CCD detector with a magnification of 2.2X. The detector is attached to the filter box shown on the left extreme. The photograph shows only the outer tubes attached to the plasma chamber, but actually they are well extended into the plasma chamber. A glass window separates the outer part from the inner part placed inside the evacuated plasma chamber.

The plasma was formed by focusing the laser beam using a plano convex lens of $f = 50$ cm onto thick (~ 4.5 mm) aluminium slab targets. The typical focal spot size was $\sim 150 \mu\text{m}$ (dia.), resulting in a focussed laser intensity $\sim 5 \times 10^{13} \text{ W/cm}^2$. The probe beam was generated by splitting a portion of the main laser beam after the Amplifier A5 stage and converting into second harmonic beam using a type II KDP crystal. By using the second harmonic of the laser (instead of fundamental), a) the effects due to refraction of the probe beam in the plasma can be reduced, and b) the plasma regions near the critical density can be probed. The typical duration of the probe beam was ~ 450 ps. The heating beam was used after the amplifier A6 stage and it travelled tens of meters distance before it reached the plasma chamber. For synchronization, the probe beam was propagated through a similar distance using three image relay systems and an evacuated spatial filter assembly to improve the spatial quality of the probe beam as shown in Fig. 5.3. The probe beam later passed through a probe amplifier, KDP crystal, and a variable delay line. The probe amplifier was used to increase the energy of the probe beam.

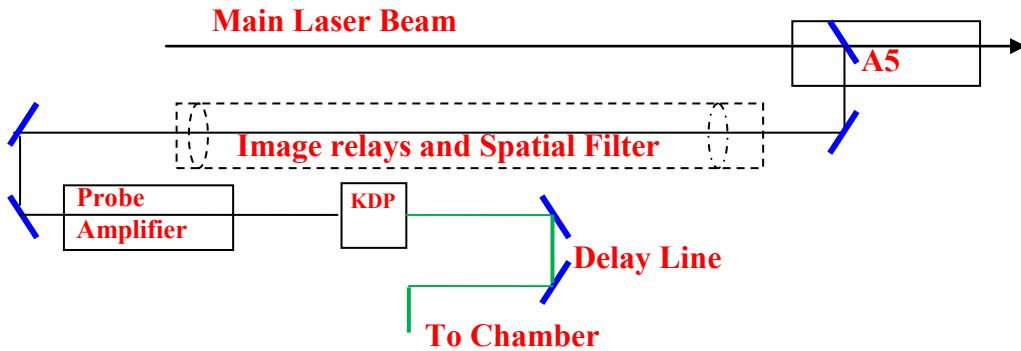


Figure 5.3: A schematic diagram of probe beam generation and propagation

The main beam and probe beam were synchronized to an accuracy of few hundreds of pico-seconds using a Hamamatsu bi-planar photo diode placed near the centre of the plasma chamber. Using a calibrated delay line, the delay could be varied in steps of ~ 100 ps. A He-Ne

laser was initially used to orient different components of polaro-interferometer and then the probe beam was made collinear with this laser. Since the chip sizes of standard CCD cameras are quite small, a digital SLR camera (Canon 350D) with a large format CCD chip ($\sim 22 \times 15$ mm) with pixel size of $6.4 \mu\text{m}$ was used to record the three channels. The sensitivity of this camera decides the accuracy to which the Glan prism (GP2) can be oriented. The camera was connected to the USB port of a personal computer used to control different parameters in the manual mode, and also do the remote recording. The camera was operated in the manual mode with a ~ 3 -4 sec exposure time and suitable ISO setting. To record the data, the camera was triggered just before the firing of the laser shot.

In addition to the probe beam, the scattered light from the main laser beam and a portion of the self luminosity of the plasma also reach the CCD detector. These two form a strong background and must be eliminated to be able to record the Faraday channel. In order to suppress this background radiation, an optical band pass interference filter for 2ω (530 nm, with a ± 10 nm bandwidth) was used in front of the CCD camera. During the laser plasma interaction, strong emission at second harmonic wavelength occurs in the plasma, which will pass through this interference filter. In order to suppress the background due to this, neutral density filters with strong attenuation factors were used. It should also be noted that only a small fraction of the probe beam passes through the polaro-interferometer from input polarizer to exit polarizer ($\sin(\theta)$ dependence). In order to be able to record this transmitted probe laser signal passing through the polaro-interferometer and neutral density filters, one needs to have a probe beam with sufficiently large energy. A rough estimate gave around 150 mJ in 2ω as sufficient energy. This

was the reason for adding an additional probe amplifier in the path. For normal shadowgraphy or interferometry experiments, this amplifier may not be necessary.

Targets were placed on a three axes target positioning system controlled from outside using a stepper motor controller. The plasma chamber was evacuated to 10^{-4} mbar using a turbo molecular system backed by a rotary pump.

5.4 Results and the Analysis of data

The experiments were carried out with the laser heating pulse energy $\sim 5-7$ J and a pulse duration ~ 650 ps. The delay of the probe laser pulse w.r. to the heating laser pulse was varied from ~ 1 ns to ~ 4 ns. For the sake of clarity the results obtained at a particular probe delay i.e. 3 ns are presented first and they are analyzed to obtain the spatial profiles of the electron density and magnetic fields. Reproducibility of the results obtained at this delay is also discussed. This is followed by a brief discussion on results at different probe delays and their analysis. An image recorded using the three channel polaro interferometer at a probe delay of 3 ns with respect to the heating laser pulse is shown in Fig. 5.4.

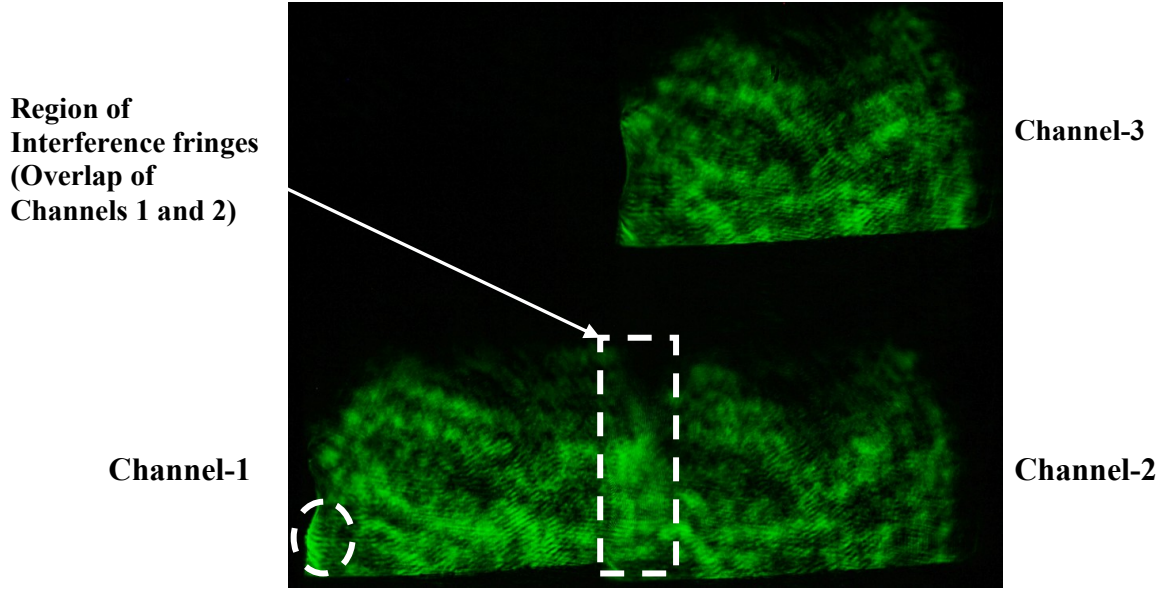


Figure 5.4: Three channel polaro-interferometer image recorded
at a delay of 3 ns for aluminium plasma

The lower left channel referred to as channel -1 is used for Faraday rotation angle measurements as discussed earlier. The bright region in this channel (shown as dashed circle) corresponds the area in which magnetic fields are generated in the laser plasmas. The top right channel referred to as channel-3 is used as reference shadowgram channel while calculating the magnetic fields. It can be seen from this channel that the spatial profile of the probe beam is non uniform. The overlapping region between the two channels i.e. channels-1 and 2 (shown as dashed rectangle) is used for generating interference fringes for density measurements. Magnified views of this image showing sections of the image surrounding the laser produced plasma in these three channels are shown. in Fig 5.5.

Figs 5.5a-c show the Faraday channel, region of interference fringes and shadowgraph respectively for a probe delay of 3 ns. The black curved region is the boundary between dense plasma and under dense plasma (for 2ω). The regions of enhanced intensity in the Faraday channel (Fig 5.5 a) can be clearly seen. The enhancement in the lower region (lower dashed circle) was due to Faraday magneto-optical effect, when the component of the self generated magnetic field B_z is parallel to the probe beam direction. Another region symmetrical around the laser axis, corresponding to this, can also be seen (upper dashed circle), where B_z is anti-parallel to the probe beam. In this case, the intensity of the Faraday channel is reduced compared to the reference value. This shows the toroidal nature of the magnetic fields generated in the present case.

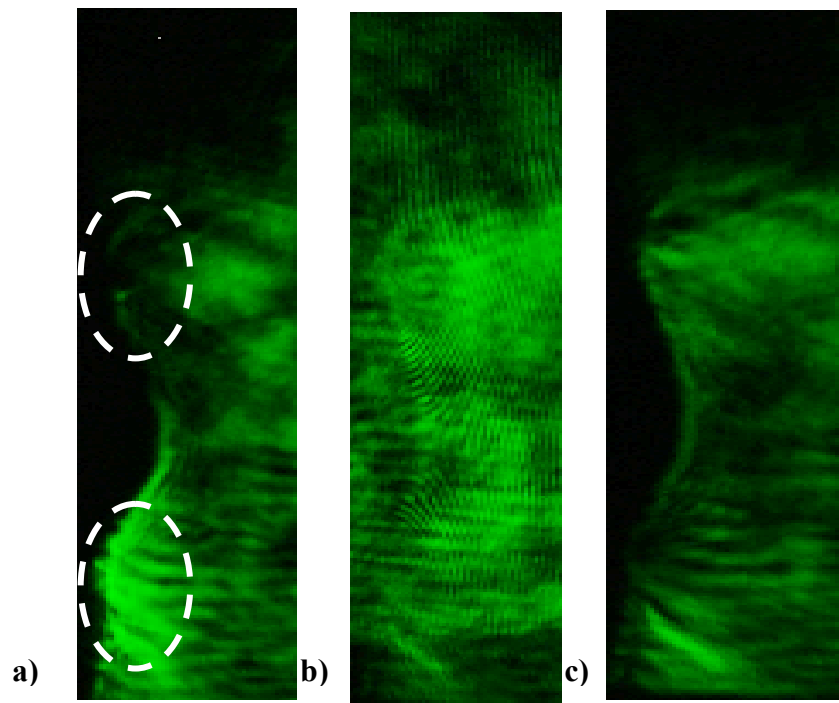


Figure 5.5: *Magnified view of three channels at a probe delay of 3 ns a) Polarogram, b) Interferogram, and c) Shadowgram^l*

Fig. 5.5(b) shows the region of interference fringes. The shift in the interference fringes can be seen to be gradually decreasing as we move radially away from the plasma. The spatial intensity variations in the shadowgram shown as a reference (Fig 5.5c) clearly explains the necessity of recording this channel and importance of taking these variations in to account while calculating the magnetic fields.

The two dimensional spatial profiles of the rotation angle are calculated using a MATLAB program from the ratios of the intensity of Faraday channel and Shadowgraph in the enhanced region. From the eqs. 5.6(a) and (c), the rotation angle is calculated as

$$\theta = \tan^{-1} \left(\left(\sqrt{I_F/I_S} \right) * \tan(\varphi) \right) \pm \varphi \quad \dots 5.8$$

here I_F and I_S are intensities in the Faraday channel and shadowgraph at each point (pixel) in the region and φ is the de-crossing angle ($\sim 2^\circ$) between the Glan polarizer GP1 and the Wedge W1. The corresponding locations in different channels are experimentally measured by imaging a cross wire placed at the plasma plane. The spatial profiles of the rotation angle corresponding the above images (at a probe delay 3ns) is shown as a two dimensional contour diagram on a color scale (black : minimum to red and grey maximum) in Fig. 5.6.

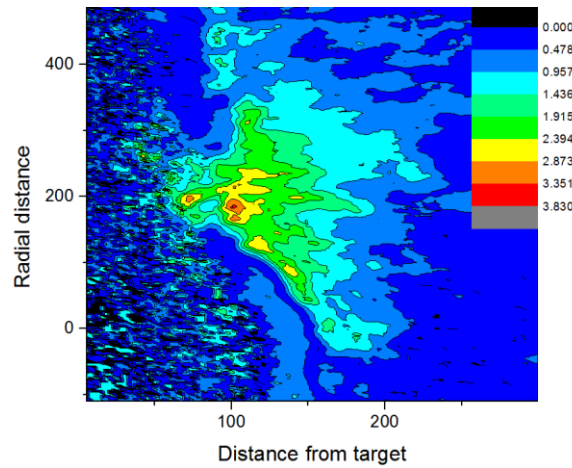


Figure 5.6 : *Rotation angle contours at a probe delay of 3 ns*

From the two dimensional contour of the enhanced region shown in Fig 5.6, it can be seen that at a delay of 3 ns the peak of the rotation angle (shown in orange and red) is located at a distance of 100μm away from the target surface, at a radial distance of 200μm. Now in order to calculate the self generated magnetic fields, the corresponding electron density values have to be estimated first. The region of overlap shown in Fig. 5.5(b) with interference fringes is used for this purpose. The electron density is estimated for fringes at different distances from the target surface. The distance between the target edge and base of an interference fringe where shift is zero is taken as the distance from the target surface. The electron density is calculated from the fringe shift 'δ' as

$$n = \frac{2\pi mc^2 \delta}{\lambda_p e^2 L \Delta x} \quad \dots\dots\dots 5.9$$

where m, λ_p , L, and Δx are the electron mass, wavelength of the probe beam, dimensions of the plasma, and fringe width respectively. Both δ and Δx are taken in units of pixels. The width of the interference fringes ($\sim 14 \mu\text{m}$) also decides the resolution of our measurements. L is taken by measuring the extremes of the plasma region. But this expression gives only an average electron density and not the spatial profile. As laser produced plasmas are radially symmetric around the laser propagation direction, Abel inversion (Appendix B) has been used for obtaining the space resolved density profiles. Using the Abel inversion, with the fringe shifts (in terms of fringes) at equi-distance points as input, the radial profile of the electron density is obtained as¹³⁵

$$n(r) = \frac{f_n(r)}{4.46 \times 10^{-14} L \lambda} \quad \dots\dots\dots 5.10$$

In terms of the Abel inversion output $f_n(r)$. A typical electron density profile calculated after a probe delay of 3 ns is shown in Fig. 5.7.

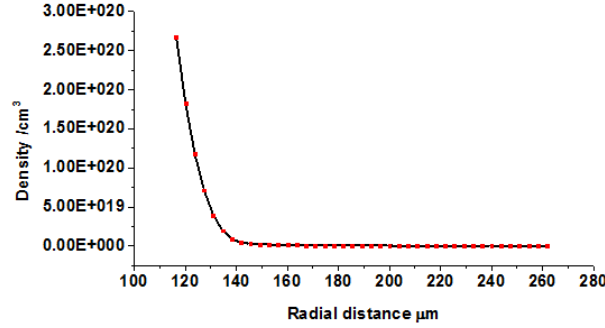


Figure 5.7: *Radial profile of the electron density for a delay $\sim 3\text{ns}$*

Now the corresponding rotation angle ' θ ' had to be estimated at an same distance where the electron density profile has been obtained. This is calculated as described previously while obtaining two dimensional rotation angle contours. The only difference presently is that intensity ratios of the Faraday channel and Shadowgraph along a vertical line are compared. Assuming the symmetry of the Faraday rotation due to toroidal magnetic fields, only one side of the image (brighter) where rotation angle ' θ ' is positive was analyzed. A MATLAB program was used to calculate the rotation angle. The detailed procedure used in terms of the software is given in the Annexure C along with the MATLAB program.

After the calculation of rotation angle, Abel inversion technique has been used to obtain space resolved rotation angle calculated using the expression 5.8. But instead of using rotation angles, normalized rotation angles (θ/y) are used as input to the inversion technique. The radial profile of magnetic field at that axial distance is expressed in terms of the Abel outputs $f_B(r)$ and $f_n(r)$ as¹³⁵

$$B(r) = \frac{29.73 * r * f_B(r)}{\lambda * f_n(r)} \quad \dots 5.10$$

Radial profiles of the self generated magnetic field at different axial distance calculated using this expression is shown in Fig. 5.8.

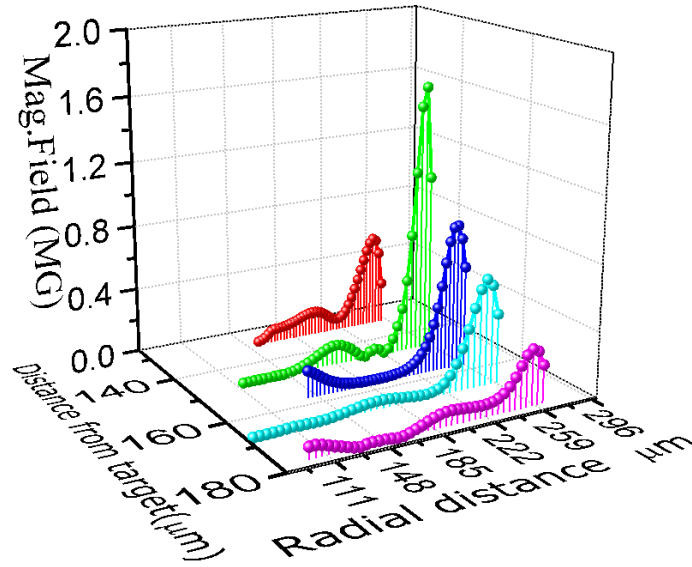


Figure 5.8: Spatial profiles of the self-generated magnetic field at a delay of 3ns.

The profiles shown in Fig 5.8 corresponds to a probe delay of 3 ns with respect to the heating beam. The magnetic fields are generated at a distance of 130 - 180 μm from the target surface and radial distance of 200 - 250 μm . The peak of the magnetic field is located at around $\sim 150 \mu\text{m}$ from the target surface and at radial distance of $\sim 250 \mu\text{m}$. But the two dimensional contour diagram earlier shown in Fig 5.6, the peak of the rotation angle was centred around $\sim 100 \mu\text{m}$ from the target surface and at radial distance of $\sim 200 \mu\text{m}$. This is because, the rotation angle is the integrated effect of the density and the magnetic fields peaks in regions where the

product of plasma density n_e and magnetic field B is maximum. The maximum value of the magnetic field occurs in a slightly lower density region (outer).

The symmetry observed in the enhancement as discussed after Fig 5.5, confirms the assumption that the magnetic fields generated are indeed toroidal in nature. The possible mechanism for generation of such large scale toroidal magnetic fields in general may be either ejection of hot electrons from the focal spot region or due to the $\nabla n_e \times \nabla T_e$ process. But as the laser intensity in the present experiment is only $\sim 5 \times 10^{13} \text{ W/cm}^2$ and as the magnetic fields lasted for few nano seconds after the heating beam is over, it is probably the $\nabla n_e \times \nabla T_e$ mechanism that is generating the magnetic fields.

5.4.1 Reproducibility of the measurements

In order to see the reproducibility of the results, the spatial profiles of the electron density and the self generated magnetic fields estimated from the three channel polaro interferograms recorded under nearly similar experimental conditions are shown in Fig 5.9. These images are recorded for same probe delay $\sim 3\text{ns}$ with respect to the heating laser beam and energy of the heating laser pulse $\sim 6\text{J}$. It can be seen that results are comparable within the experimental errors. The electron density at this location varied from $1 \times 10^{17-20} / \text{cm}^3$ for different radii. A magnetic field of $\sim 1.5 - 2 \text{ MG}$ is estimated at the outer region of the laser plasma at $\sim 250 \mu\text{m}$.

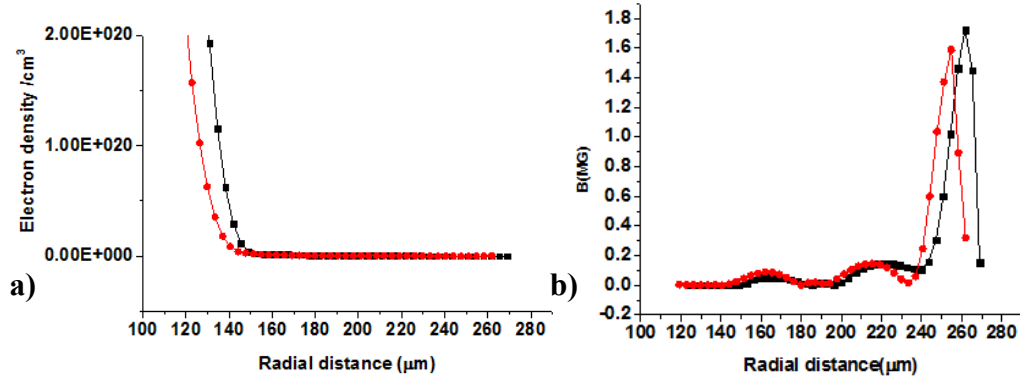


Figure 5.9 : The electron density and magnetic fields in different laser shots for 3 ns delay

The errors in these calculations originate from the error in the offsets between the three channels which is difficult to quantify. Secondly the spatial resolution of the measurements is limited by the width of the interference fringes which is 14 μm in the present case. The spatial profiles in Fig 5.9 have similar uncertainty in determining the distance from the target surface.

5.4.2 Analysis of the images obtained at different probe delays

Experiments were also conducted at different delays between the probe laser pulse and heating laser pulse. These results are briefly discussed below. The images showed in Fig 5.10 corresponds to the probe of delay of 1.6, 1.9, and 2.7 ns respectively.

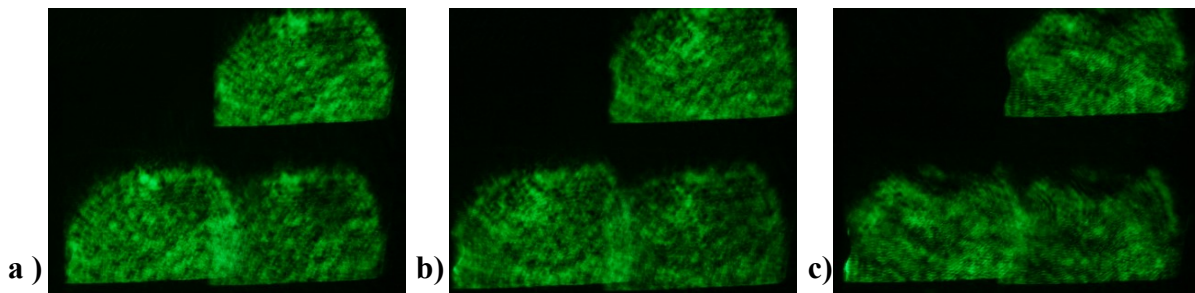


Figure 5.10: Three channel images at probe delays a)1.6, b) 1.9 and c)2.7 ns

It is experimentally seen that the images at smaller delays (~ 1.6 ns Fig 5.10a) did not show any enhancement in the Polaro (Faraday) channel. The possible reason for this may be that the magnetic fields are located in the high density region closer to the target surface at smaller probe delays, which are inaccessible for the probing wavelength due to the high refraction or probably may due to blocking of the probe beam by the front surface of the target (shadow). From Fig 5.10b it can be seen that enhancement is present for delays around 1.9 ns and above. It is experimentally seen that this enhancement is present for the delay over which images were recorded. The spatial profile of the rotation angle at the probe delay 1.9 ns is shown as a two dimensional contour diagram on a color scale (black : minimum to red and grey maximum) in Fig. 5.11.

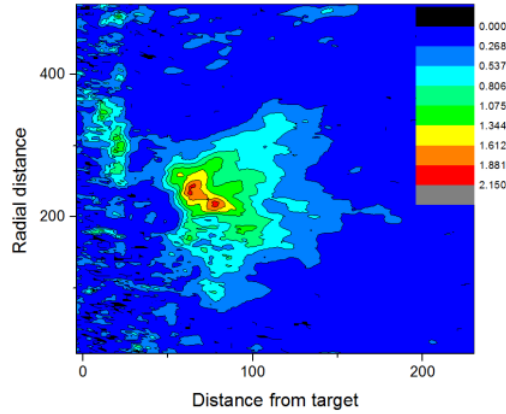


Figure 5.11 : *Rotation angle contour after a probe delay of 1.9ns*

From the two dimensional contours of the enhanced region (shown in orange and red) it can be seen that at a delay of 1.9 ns the peak of the Faraday rotation angle is at 70 μm away from the target surface, at a radial distance of ~ 200 μm . As shown earlier after Fig 5.6, the peak of rotation angle had shifted to ~ 100 μm away from the target surface for a probe delay of 3 ns. There was not much change in the radial distance of this peak at different delays.

In general it is seen that the main issue affecting the estimation of the electron density and the magnetic fields is the spatial quality of the probe beam. It is seen that tracking the interference fringes becomes difficult in certain regions due to the poor quality of the probe beam. This may be due to unequal amplitudes of the overlapped components of the interfering beam in those regions, resulting in poor contrast of the interference fringes. Secondly the fringe shifts in regions closer to the target surface were not measurable at earlier probe delays making density measurements difficult although enhancement is clearly seen. This had restricted the probe delays over which we could estimate the magnetic fields.

5.5 Conclusions

Self generated magnetic fields of order of few MG have been detected using Faraday rotation. A three channel polaro - interferometer has been used which simultaneously records the Faraday rotation, the plasma density information, and the spatial profile of the laser probe beam. In our experiments conducted at a focussed laser intensity of $\sim 5 \times 10^{13} \text{ W/cm}^2$, magnetic fields of $\sim 1.5 \text{ MG}$ have been detected in aluminium plasmas after a delay of 3 ns. These toroidal magnetic fields have been attributed to the thermo-emf effect due to large density and temperature gradients present in the laser produced plasmas. It is seen that peak of the rotation angle and peak of magnetic fields occurred at different distances from the target surface. This is because the rotation angle depends on the product of the electron density and the magnetic fields and peaks in regions of higher electron density. It is also seen that the peak of the rotation angle located at $70 \mu\text{m}$ away from target surface at 1.9 ns delay moved $\sim 100 \mu\text{m}$ after a probe delay of 3 ns. A MATLAB based program has been written to carry out the image analysis and calculations, instead of using multiple computer software to do the same.

Chapter 6 : Shock wave propagation in transparent materials

6.1 Introduction

Understanding the behaviour of different materials under high pressures has been a subject of great interest for mankind, to know about what is happening in the interior of the planet Earth. The typical pressure and temperature in the inner core of Earth are around 3.5 Mbar and 5400°C respectively. Seismologists have been trying to study how the inner and outer cores of the Earth are evolving, by simulating those conditions in laboratory⁴⁰. Such static high pressures can be generated in the laboratory using standard techniques like *diamond anvil cell* (DAC)⁴³. In 2012, Dubrovinsky *et al* had reported highest static pressures upto 6.4 Mbar in rhenium using an improvised version of DAC consisting of second-stage anvils made of nano-diamond micro-semi-balls¹³⁶. The studies at high static pressures help one in creating conditions in the laboratory similar to those encountered in the geophysical areas. Pressures higher than these static pressures are generated by using dynamic techniques like high velocity impacts using light-gas guns^{44,45}, explosive contacts, and laser generated shock waves. Generation of high dynamic pressures using these techniques have also found multiple applications in diverse scientific areas. For example, studying the formation of impact craters by meteorites, micro-meteoroids, and orbital debris on space voyagers^{41,137} in the laboratory conditions is very important for astrophysical studies. In the field of Inertial Confinement Fusion (ICF), the density and temperatures of the fuel pellets irradiated by intense lasers reaches nearly 600 times the liquid density, and several thousands of degrees⁴². Reinhart *et al* have generated impact velocities of 11 km/s using a three-stage light-gas gun also known as

hypervelocity launcher (max 16 km/s) with flyer plates of a titanium alloy Ti-6Al-4V¹³⁸. Similarly, explosive contact methods have also been used to generate dynamic pressures. Each one of these techniques has some advantages as well as inherent limitations. Techniques like DAC and flyer plate impact can generate pressures below tens of Mbar. The explosive contact method cannot be conducted often as they require nuclear explosions for generating higher pressures. As an alternative to the above techniques, laser generated shock waves have become a valuable method^{139,140} to generate dynamic pressures ranging from hundred of kbar to several Gbar^{48,141}, corresponding to laser intensities of 10^{13-15} W/cm².

6.1.1 Basics of high pressure generation using shock wave

A brief introduction to generation of high pressures in materials, mechanism of shock wave generation, scaling of pressures with laser intensity and wavelength and response of the materials to the shock wave propagation are discussed in the introductory chapter 1. A brief discussion about detection methods to obtain properties of laser generated shock waves follows here. In this technique, a high power laser is focussed on a material generating hot, dense and rapidly expanding plasma. Due to the recoil momentum associated with this outwardly expanding plasma, a compression wave is launched in the rest of the target near the interaction region. As this compression wave generated by laser irradiation is dynamic in nature, it is interesting to study how the shock wave evolves in space and time. The shock wave travelling in the medium at supersonic speed leads to formation of a shock front across which a near discontinuity in material properties like density, temperature and pressure exists. Rankine - Hugoniot equations expressed below relate these material properties on either side of the shock front¹⁴²

$$\rho_0 U_s = \rho_1 (U_s - U_p) \quad \text{-----6.1}$$

$$P_1 - P_0 = \rho_0 U_s U_p \quad \text{-----6.2}$$

$$E_1 - E_0 = 0.5 (P_1 + P_0) (1/\rho_0 - 1/\rho_1) \quad \text{-----6.3}$$

Here ρ_0 , P_0 , E_0 , ρ_1 , P_1 , E_1 are the mass density, pressure, internal energy of the material before and after passage of the shock wave, and U_s , U_p are the shock velocity and particle velocity respectively. The above three expressions are essentially based on the conservation laws of mass, momentum, and energy before and after the passage of the shock wave. As the initial conditions (ρ_0 , P_0 , E_0) are known, all the five parameters can be estimated by measuring any two of these parameters and then using these three equations. Usually, in laser generated shock wave experiments, the shock wave velocity U_s and the particle velocity U_p are the parameters measured experimentally. The shock experiments are generally conducted using targets in the form of thin foils of known thickness. When the shock wave reaches the rear side of the foil, the shock wave unloads resulting in a shock luminosity signal. The shock wave velocity is estimated by measuring the time delay between the heating laser pulse and appearance of the shock luminosity signal. Since the time scales involved are in sub-ns range, fast response devices like optical streak camera¹⁴³ are used for detecting the optical luminosity signals. This simple description assumes that the shock wave is travelling with an average velocity U_s in the foil. In reality, the shock wave evolution is much more complicated. As the shock wave velocity is proportional to the amplitude of the wave, during the rising part of the laser pulse, the shock wave velocity increases with time. This means that later parts of the shock wave travel with a higher velocity compared to the earlier parts of the shock wave. As the shock wave travels inwards, this leads to *shock wave coalescence*⁶⁹. After the peak of the laser pulse, the amplitude of the compression wave decreases with time. This can also be visualized as if the front side of the material on which laser is incident has started relaxing from the previous compressed state.

Effectively, a rarefaction wave propagates from the laser irradiated side to the backside in the compressed medium. Since the effective velocity of the rarefaction wave exceeds the shock wave preceding it, the amplitude of shock front would start weakening. In addition to the shock wave coalescence and rarefaction wave weakening the shock wave velocity, some other phenomena may also occur in the shocked material like elastic-plastic deformation and pressure induced phase transitions, as briefly discussed in the section 1.7.3. Since the shock luminosity signal is generated only when the shock wave reaches the rear side of the foil, it gives time averaged velocity and cannot provide information about the temporal evolution of the shock wave velocity. However, in the case of transparent materials like glass, it is possible to study the shock wave propagation by using optical shadowgraphy and Velocity Interferometer System for Any Reflector (VISAR)¹⁴⁴. The present chapter describes our experimental results on optical shadowgraphy of shock wave propagation in the soda-lime glass.

6.1.2 Methods of shock velocity measurements

There are different types of optical diagnostic techniques used for studying the shock wave propagation. They include a) Velocity Interferometer System for Any Reflector (VISAR) b) optical transmission of a long duration laser pulse as probe beam, coupled with an optical streak camera c) multiple snap shot approach¹⁴⁵ using a short duration probe pulse, etc. As the shock wave propagates through the medium, the material near the shock front gets strongly ionized and acts as a transient reflecting surface (moving along with the shock front) for a probe beam incident from the rear side of the target. So using the VISAR technique, the dynamics of a moving shock front can be obtained. However, the time resolution with VISAR technique is limited to several tens of picoseconds. As the shock wave propagates through the medium, the

transparency of the material behind the shock front is strongly affected due to compression and increase in the mass density ρ . Using this, shock dynamics can be studied by sending a probe beam in the perpendicular direction to the heating beam. By using a long duration probe, the temporal profile of the shock wave can be recorded by recording the transmitted probe intensity using an optical streak camera. The shock wave velocity and its variation in time can be obtained by tracking the movement of shadow region created by the shock wave. However, obtaining a synchronized long duration probe pulse is quite difficult due to time jitter related issues. In this case the temporal resolution is limited to several picoseconds by the streak camera.

Based on a technique known as Chirped Pulse Amplification(CPA), table top, ultra-short, ultra-intense femtosecond laser systems delivering pulses of power ranging from tens of terawatts (10^{12} W) to petawatts (10^{15} W) have been built in the last decade. In this technique, the femto second laser pulse from the oscillator is stretched in time to several hundreds of picoseconds to nanoseconds duration by spectrally dispersing the laser pulse (i.e. frequency chirping). This stretched pulse is then amplified further and then compressed back to get an ultra-intense femto second pulse. The advent of CPA¹⁴⁶ technique has also provided a novel solution to study the evolution of the shock wave propagation in a single shot with sub-picosecond temporal resolution. In the CPA technique, diffraction gratings are used to spectrally disperse the input pulse. This introduces a well defined linear relation between wavelength ' λ ' and time ' t '. Thus the stretched chirped pulse can be used as a probe to study temporal evolution of any process or phenomenon. The high temporal resolutions which are possible with the chirped pulse probing technique are better than those possible with streak cameras.

Shock wave experiments were carried out using the high power Nd:glass laser system⁷¹ at Laser Plasma Division, Raja Ramanna Centre for Advanced Technology(RRCAT), Indore,

using mainly the snap-shot technique. The Chirped Pulse Shadowgraphy (CPS) technique was also tried for obtaining time resolved shock velocity profile. Both these techniques have been described in detail in Chapter 3 earlier. The evolution of shock waves in transparent soda lime glass targets has been studied and the temporal variation of the shock velocity has been obtained. The details of these experiments are presented in this chapter. Section 6.2 describes the chirped pulse shadowgraphy experiments conducted and results obtained using this technique. Section 6.3 covers the shock velocity measurements using snap shot shadowgraphy with a short duration laser probe pulse. The results obtained from these two technique are presented and discussed in Section 6.4. In addition, some interesting jet-like structures were also observed in the shadowgraphy experiments. These observations and some important points that need attention have been briefly discussed in the last section.

6.2 Chirped pulse shadowgraphy

6.2.1 Description of experiment

The chirped pulse shadowgraphy experiments were carried out using Chameleon laser pulses (Ultra II, M/s Coherent Inc., USA spectral bandwidth of ~ 13 nm at 1054 nm), stretched to 650 ps (FWHM) using grating based pulse stretcher. These temporally stretched pulses were then amplified first in a regenerative amplifier to few mJ level (gain of 10^7)¹⁴⁷ and then using the conventional Nd: phosphate glass amplifier chain of the high power laser system to energies up to 10 J⁷¹.

The chirped pulse shadowgraphy is shown schematically in Fig. 6.1. The heating beam was focused using a lens of $f = 50$ cm placed outside the plasma chamber. The typical focal spot size was ~ 100 μm , leading to laser intensities of 10^{13-14} W/cm². The laser pulses were focused

on the thin side (1.3 mm) of a commercial microscope glass slide (25 mm x 75 mm). The chemical composition of these slides made from soda lime glass is typically: SiO_2 (73.2), Na_2O (10.6), CaO (9.4), MgO (3.1), Al_2O_3 (1.8), K_2O (1.1), TiO_2 (0.6), and Fe_2O_3 (0.2)¹⁴⁸. These targets were mounted on a three-axes motorized translation stage. This target movement system is connected to a micro controller using which the targets can be moved along X, Y, and Z directions with a precision of a few microns. This is placed outside an evacuated plasma chamber (10^{-5} torr). For evacuating the plasma chamber, a turbo-molecular pump based vacuum system was used. Using the target movement system, a fresh target surface was exposed to each laser shot.

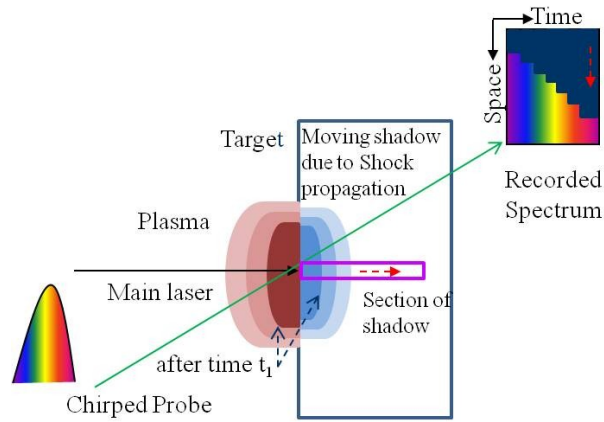


Figure 6.1: *A schematic diagram of the chirped pulse shadowgraphy*

In order to study the temporal evolution of the shock wave propagation in transparent materials, a synchronized probe pulse with well defined chirp was required. This was generated by splitting a portion of the stretched main laser pulse after the fifth amplifier stage (A5) of our high power laser system. The bandwidth $\Delta\lambda$ in the probe beam was reduced to ~ 2.4 nm after it was passed through the amplifier stages. The probe was then passed through three image relays, a spatial filter, and a delay line. A schematic diagram showing the generation of probe beam is

given in the previous chapter (Chapter 5, Fig. 5.3). Three image relay systems were used to relay the probe beam over a long distance before it reached the plasma chamber. The image relays also provided the necessary demagnification of the probe beam (from 40 mm to ~ 15 mm). A variable delay line was used to synchronize the probe beam with the heating beam in steps of 100 ps. A bi-planar diode placed at the centre of the plasma chamber, where the main laser and the probe laser overlap in space was used to measure the temporal delays. A He-Ne laser was made collinear with this probe beam for aligning the optical elements and the CCD detector.

The plasma plane was imaged onto the entrance slit (50 μm) of a Czerny-Turner spectrograph (Digikrom 480 from CVI) with a large magnification factor of $\sim 40\text{X} - 60\text{X}$. The spectral resolution of the spectrograph with a grating of 1200 grooves/mm was 0.3 nm. To study the shock wave propagation in time, the direction of the spectral dispersion (and thus time, in the case of a chirped pulse) must be perpendicular to the direction of the shock wave expansion. Therefore the plasma image was rotated by 90° using an image rotator (based on prisms) placed just before the entrance slit of the spectrograph.

The spectral output at the exit plane of the spectrograph (exit slit removed) was imaged using a charge coupled device (CCD) camera with suitable demagnification. Thus, in the recorded images, the horizontal axis (direction of spectral dispersion) provides the temporal information, whereas the vertical direction gives the spatial information of the shock wave (shadow) movement. The CCD camera was triggered by a signal from the laser control room. As the CCD camera has an integration time of a few microseconds, it was triggered before the laser shot was fired.

Since the target region is being probed tangentially (perpendicular to the direction of heating pulse) even a small angle between the probe and target front surface(edge) will lead to

creation of a shadow which may block the initial stages of the plasma expansion and shock wave propagation. In order to reduce this blocking, back reflection from the sides of glass target was used to ensure that the target was perpendicular to the probe laser beam. In addition, only those targets having flat surface on the sides were chosen for experiment.

6.2.2 Results and discussion

In the shadowgraphy experiments, each plasma shot was preceded by a *probe only* shot in which a reference shadowgram was recorded by blocking the main laser beam. This helped in locating the origin of the shock front movement. A reference shadowgram taken in absence of the heating beam is shown in the Fig. 6.2a. A shadowgram recorded with the probe beam passing through the shocked region is shown in Fig. 6.2b.

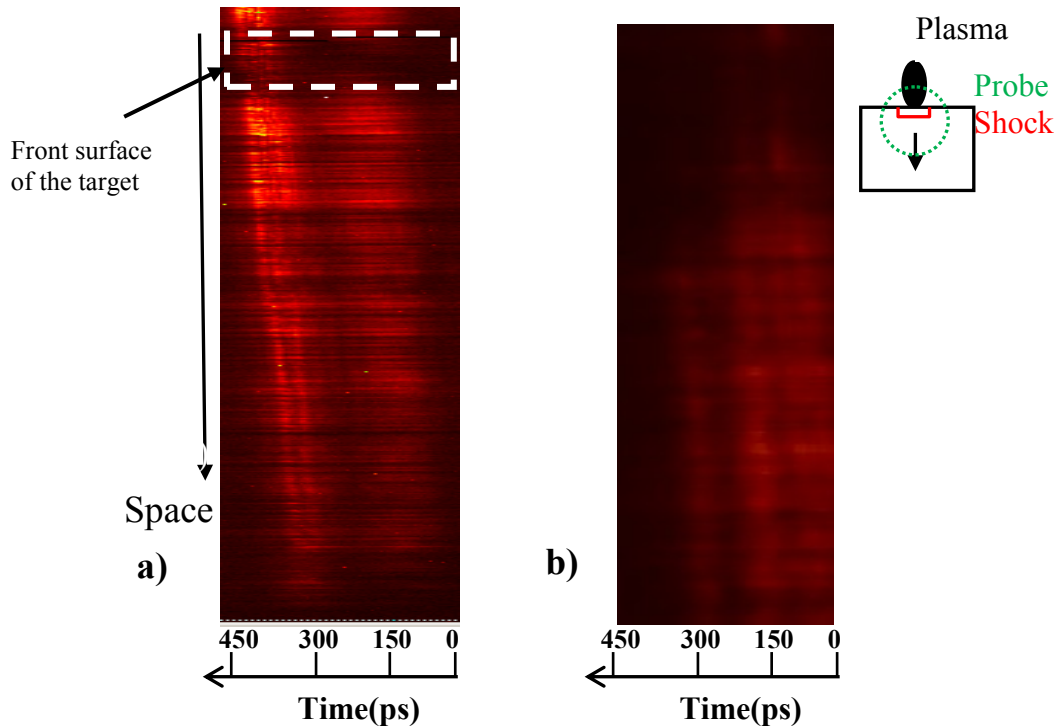


Figure:6.2 Shadowgrams recorded with chirped probe pulse providing temporal evaluation of shock propagation in soda lime glass a) without and b) with shock wave propagation¹

The shadowgram shown in Fig. 6.2(a) is essentially to mark the position of the target surface (shadow boundary) as indicated by the dotted rectangle. Fig. 6.2 (b) shows the shadow boundary moving downwards with time as time increases from right to left on the horizontal axis. The quantitative analysis of the movement of shadow boundary from such shadowgram is used to derive shock velocity at different times as discussed below.

In case of chirped pulse probing, since different wavelengths are passing through the interaction region at different times over the duration of the probe pulse, the trajectory of the interface between the shadow and the bright region will give information about the movement of shadow in time. This in turn is related to the movement of the propagating shock wave in the transparent medium, as the shadow is formed due to densification of the region in the transparent target material immediately after the shock wave crosses it. By tracking the top edge of the bright region at different points of the transmitted chirp beam, the spatial coordinates of the shocked region have been obtained. In order to calculate the shock velocity, the calibration along both x axis (time) and y axis (space) is required. The first one is estimated from the known chirp factor (ps / nm) and number of pixels in the probe spectrum (pixels/nm). The calibration factor (space) is experimentally obtained by moving the target by a known amount and measuring the shift at the image plane. The spatial calibration factor (y-axis) was $\sim 0.1 \mu\text{m}/\text{pixel}$ and the time calibration factor (x-axis) was $\sim 8 \text{ ps}/\text{pixel}$. The space-time graph of the moving shadow is obtained from which the velocity of the shock wave is determined from the slope at different times.

The values of the shock velocity at different times (represented as delay from peak of the heating laser pulse) at a laser intensity of $\sim 1 \times 10^{14} \text{ W}/\text{cm}^2$ is shown in Fig 6.3. It is observed that the values of shock velocity are decreasing with increasing time w.r. to the peak of the heating

laser pulse. A shock velocity of $\sim 7 \times 10^6$ cm/s is estimated after 1.2 ns with respect to the peak of the heating beam. This falls to $\sim 4 \times 10^6$ cm/s after 1.4 ns. The possible reasons for this are briefly discussed in the analysis part in section 6.4. The error in the shock velocity calculation is mainly arising due to the finite width of the entrance slit (50 μ m) of the spectrograph. This results in a ± 13 ps error in measurement of time at different instances during the probe pulse.

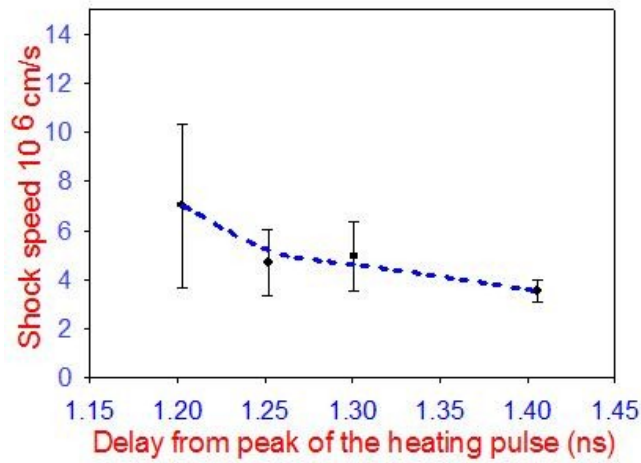


Figure 6.3: Variation of the shock velocity with time at $I_L \sim 1 \times 10^{14}$ W/cm²

6.3 Snapshot Shadowgraphy

In addition to the chirped pulse shadowgraphy described above, snap shot shadowgraphy was also used to study the temporal evolution of the shock waves propagating in the transparent soda lime glass. For this set of experiments, laser pulses of 500 ps duration (FWHM) at 1054 nm from the laser oscillator later amplified to 1-10 J energy were used.

The probe beam generation was identical to that described in the earlier section. The only difference is that probe pulse was converted to second harmonic wavelengths as described in Chap. 5 on magnetic fields. The experimental setup for the snap shot approach was similar to that of chirped shadowgraphy, except that the spectrograph and CCD were replaced by a DSLR

camera (Canon 550 D) with a large size sensor (22.5 mm \times 15 mm) in the present experiment. This is required as the chip size of conventional CCD cameras are quite small and with a large area detector it is easy to align. In order to block the plasma emission (luminosity) and scattered laser light, interference filters for 527 nm ($\Delta\lambda \sim \pm 10$ nm) and neutral density filters were placed before the detector.

6.3.1 Results from snap shot shadowgraphy

Experiments were conducted on the Nd:glass high power laser system at energies below 10 J. The targets used were same as in the chirped pulse shadowgraphy. Laser pulses were focussed on 1 mm side of target. The delay between the heating pulse and the probe pulse was varied in steps of 1 ns, and plasma shots were fired at different laser energies to obtain data at different intensities. Fig. 6.4 shows typical shadowgrams recorded using the snap shot technique. Fig. 6.4(a) shows a reference shadowgram, recorded in the absence of plasma. Fig. 6.4(b) shows a shadowgram with probe beam passing through the shocked region in the target after a delay of 2 ns from the peak of the heating laser pulse.

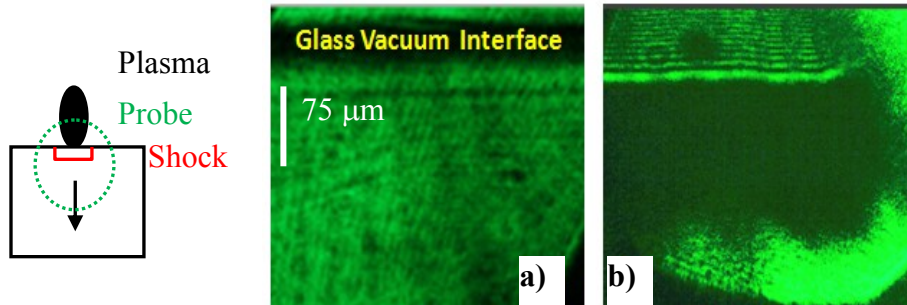


Figure 6.4: Snap-shot shadowgrams a) without shock, b) with shock wave propagation¹ (schematic on left most side)

The glass vacuum interface shown in the Fig 6.4a is shadow of the target front surface. The portion below this interface shows part of the probe beam passing through the transparent glass target. Referring to the shadowgram in Fig 6.4(b), the width of the shadow in horizontal direction corresponds to the laser focal spot size. The length of the shadow (in vertical direction) measured from glass vacuum interface up to the lower edge of the shadow represents the movement of the shock front up to the time probe pulse passed through the shocked region. It is also seen that the lower part of the shadow region is not uniform. This is related to the presence of non uniform irradiation by the heating laser pulse due to presence of hot spots in the spatial profile.

As the shadow is formed due to densification of the medium by the propagating shock wave, the extent of the shadow in the vertical direction represents the distance up to which the laser generated shock wave has reached in the target up to that time of the probe beam. The glass vacuum interface is the origin of the shock wave. The shock wave velocity can be estimated from this measurements. Shadowgrams were recorded at different delays of the probe beam, in different laser shots under similar experimental conditions.

The variation of shock velocity with time with respect to the peak of the heating laser pulse at two laser intensities of $4 \times 10^{13} \text{ W/cm}^2$ and 10^{14} W/cm^2 thus obtained is shown in Fig. 6.5. The measurements were not possible at delays smaller than 1 ns due to the finite width ($\sim 35 \mu\text{m}$ at plasma plane) of the shadow of the target front surface. Hence the graph shown in Fig. 6.5 represents the shock velocity-time variation after the peak of heating laser pulse. The error bars are also related to this uncertainty in locating the origin of shock front due to the finite width of the shadow of target front surface.

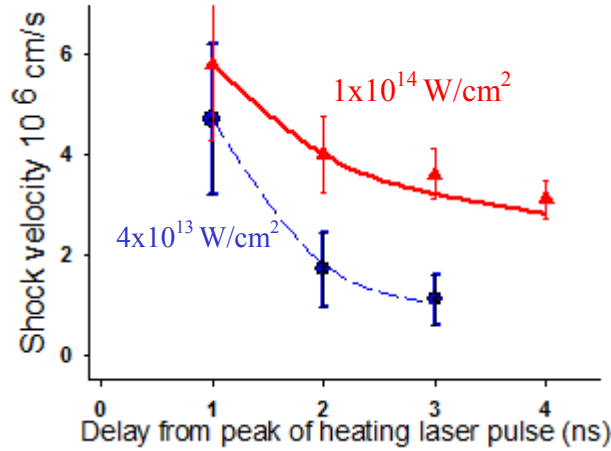


Figure 6.5: Variation of the shock velocity with time at two laser intensities 4×10^{13} (blue) and 1×10^{14} (red) (The curves are only to guide the eyes.)¹

6.4 Analysis of shock wave velocity evolution

As discussed earlier in Chapter 1, the shock velocity is proportional to the amplitude of the shock wave. One can treat the rising portion of a laser pulse as a sequence of several short pulses with continuously increasing intensity, with Gaussian temporal envelope. This will lead to generation of several shock wave components, each having a higher amplitude and hence travelling with increasing velocity compared to the previous one. As they propagate inwards, all these shock components will join one another (i.e. coalesce), forming an intense shock front. During this *growing* phase, formation of a shock front due to shock wave coalescence will occur at different times, at different distances from the target front surface for different laser intensities. Similarly, after the laser peak is over, the plasma ablation rate falls, leading to reduction in the recoil momentum leading to weakening of the compression wave. In other words, this results in the relaxation of the compressed target material from the front side of the target. This can be treated as a rarefaction wave propagating in the compressed material. As this rarefaction wave is

propagating in pre-compressed material as compared to the shock wave travelling in an uncompressed material, the effective velocity of the rarefaction wave exceeds the shock velocity, and it eventually overtakes the shock front. Upon reaching the shock front, this rarefaction wave reduces the amplitude of the shock wave. This leads to a fall in the shock wave velocity (i.e. the '*falling phase*' of the shock wave). Different experimental factors like a) laser pulse duration, b) target material, and finally c) the laser intensity will determine the exact distances and times when these two phases will appear and how long they will last.

The chirped pulse shadowgram shown Fig. 6.2, and the temporal profile of the shock velocity shown in Fig. 6.3, are probably corresponding to a falling phase. This is because the chirped probe beam was passing through the shocked region after a delay of ~ 1 ns from the peak of the heating beam. The chirped pulse shadowgraphy technique was having some intricacies as discussed in sec 6.4.2 later.

Now the results from the snap shot shadowgraphy will be discussed. The shock velocities obtained will be compared with values reported in literature. The scaling of the pressure with laser intensity can be expressed by Batani et al⁵⁶. as

$$P[\text{Mbar}] \approx 15.36 \left[\left(\frac{I(\text{W/cm}^2)}{10^{14}} \right)^{4/5} \left(\frac{1}{\lambda(\mu\text{m})} \right)^{4/15} \left(\frac{1}{\rho_o(\text{g/cm}^3)} \right)^{1/15} \left(\frac{1}{d(\mu\text{m})} \right)^{2/15} \right] \text{--- --- 6.4}$$

where ρ_o is the mass density and d is the average thickness of base and step. Using this expression the approximate value of the pressures for laser intensities of 4×10^{13} and 1×10^{14} W/cm² are ~ 5.2 Mbar and ~ 11 Mbar respectively. The shock velocities corresponding to these pressures can be calculated using a perfect gas approximation expressed as^{149,150}

$$U_s = \left(\frac{(\gamma+1)}{2} \frac{P}{\rho_o} \right)^{1/2} \text{--- --- 6.5}$$

Here the mass density $\rho = 2.5 \text{ gm/cm}^3$ for soda lime glass. For soda lime glass the adiabatic constant γ is taken as 1. The shock velocities estimated using this expression are $\sim 1.4 \times 10^6 \text{ cm/s}$ and $2.2 \times 10^6 \text{ cm/s}$ for laser intensities 4×10^{13} , $1 \times 10^{14} \text{ W/cm}^2$ respectively. The shock velocities estimated from our experiments are $\sim 4.5 \times 10^6 \text{ cm/s}$, $\sim 5.5 \times 10^6 \text{ cm/s}$ respectively after 1 ns. The final velocities in these two cases reduced to $\sim 1 \times 10^6$ and $\sim 3 \times 10^6$ respectively which are closer to predicted values from the above scaling law with in experimental errors. This difference could also be due presence of laser hot spots where the local intensity may be slightly higher. The observation of higher shock velocities at earlier delays in our experiments and deviation from the velocities expected from the scaling laws are probably due to the following two reasons.

The first reason may be the presence of hotspots in the heating beam. Due to the presence of hotspots the local laser intensity in certain areas of the laser focal spot can exceed the laser intensity estimated from the laser energy. Since optical smoothing techniques are not used in the present experiment, it might have produced small-scale hot spots within the focal spot area where the local intensities may be one order larger the average intensity. This can lead increase in the shock velocities.

The second reason may be the phenomena called as *delayed compaction* similar to that observed by Ng *et al*⁹⁹ in other glasses like fused silica, quartz etc., They had observed high transient velocities of $\sim 3 \times 10^6 \text{ cm/s}$ for a laser intensity of $4.4 \times 10^{13} \text{ W/cm}^2$ in fused silica glass. The phenomena of the delayed compaction is described here. As the shock wave progresses in space, this leads to compression of the material and increase in the material density ρ . In many simpler materials like metals this volume compaction and increase in the mass density is occurring near instantaneously or on faster times scales compared to the shock loading

time scales. However, in the case of complex molecules, the response to the shock waves is different. In complex molecules, the compaction is continuous and instantaneous only up to a particular pressure. Above this pressure, the compaction is delayed by a time ranging from hundreds of picoseconds to few ns. In this case when a material is dynamically compacted leading to a final pressure slightly higher than the Hugoniot Elastic Limit (HEL) or phase transition point, the material undergoes firstly through an elastic shock followed by a intermediate or deformation shock before reaching the final shock induced state i.e. Hugoniot state which is in equilibrium. This is shown in the fig 6.6 showing the shock Hugoniot curve in the density, pressure $\rho - P$ plane for a material undergoing through

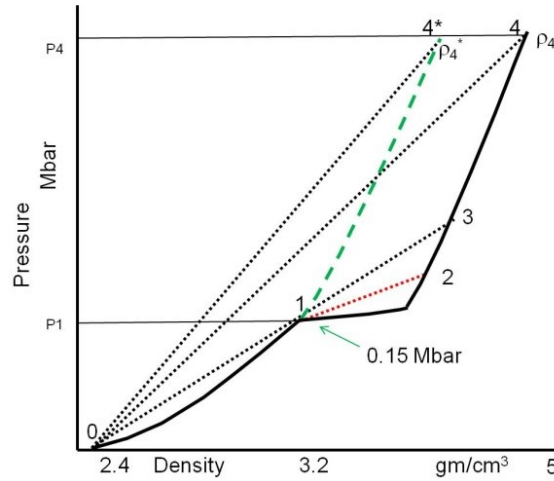


Figure 6.6: Shock Hugoniot diagram in $\rho - P$ plane for a material undergoing phase transition and delayed compaction

elastic-plastic deformation/phase transition during dynamic compaction. An accurate version of this Hugoniot curve $\rho - P$ for soda lime glass is shown by Jeanloz and Ahrens¹⁵¹. The final Hugoniot is shown as solid curve passing through 0-1-2-3-4. The material undergoes a phase transition after reaching state 1 around 100-150 kbar with the density jumping¹⁵¹ from ~ 3.1

gm/cm³ to 3.7 gm/cm³. For states with final pressure upto state 1 (below the phase transition) the state of the shocked material will move along the straight line connecting 0 -1. For the states between 1 and 3, the state of the shocked material will first move along the straight line connecting state (ρ_0, P_0) to (ρ_1, P_1) and a second shock wave taking the material from state (ρ_1, P_1) to (ρ_2, P_2) with slower velocity. This will happen for the final states below 3 corresponding to pressure P_3 .

Now for the states much higher than state 3 the possible response of the of soda lime glass will be as follows. If the material immediately reaches the state 4, one would experimentally observe the shock velocities corresponding to the slope of the Rayleigh line connecting state 0-4. These are the velocities predicted by the simulation codes and the scaling laws. For example for laser intensities around 1×10^{14} W/cm² the predicted shock velocities are around 2.2×10^6 cm/s. If the material did not reach the fully compressed state immediately but reach a low density state around (ρ_4^*, P_4) lying on the dashed line 0-1-4* and then reaching to the denser state indicated by (ρ_4, P_4) after some time. This is the *delayed compaction* as observed in various glasses like fused silica and quartz by Ng *et al*⁹⁹. This will lead to lead to the enhancement in the shock velocity expressed as (from RH equations)

$$U_s^2 = V_o^2 (P - P_o) / (V_o - V). \quad \text{--- -- 6.6}$$

From this it can be seen that a lower value of instant compaction will result in larger than predicted volume V for the applied pressure P and thus higher shock velocities U_s .

Thus the shock wave velocities measured in our experiments could be due to both these effects i.e. presence of small scale hot spots where the laser intensity in speckles will be higher than the average intensity by an order of magnitude and also due to delayed compaction phenomena.

6.4.1 Detection of ionization tracks

During these experiments for studying the temporal evolution of the shock wave velocity, some other interesting observations were made, which are described here. In order to record the complete image of the shocked region, the magnification was reduced to around 20-40X. By imaging the tip of a sharp object (straight pin) through the glass slide, the imaging was improved. When the shadowgrams were recorded under these conditions, long structures like jet streams were visible, at a distance, far away from the shocked region. In the first series of shadowgrams the magnification was set at $\sim 34X$ and shadowgrams were recorded around laser intensities of 10^{13} W/cm^2 . The delay between the probe and heating pulse was 2 ns. The recorded shadowgrams showed the presence of thin structures of $\sim 150 \mu\text{m}$ long (Fig. 6.7a). So to probe it further, the magnification and probe delay were reduced to $\sim 26X$ and 1 ns respectively but laser intensity was increased to 10^{14} W/cm^2 . The length of these structure increased further to $>500 \mu\text{m}$ (Fig.6.7e, f). In addition, the shadowgrams recorded using a He-Ne laser beam after the plasma shot showed the presence of tree-like structures centred around the laser focal spot region (Fig. 6.7c, d). The experimental parameters under which these shadowgrams were recorded are given in Table 6.1.

Sr. #	Image #	E_L (J)	I_L (W/cm ²)	M	Delay (ns)	Remarks
1	Img69	2.2	5.3×10^{13}	34	2	Length of structures $\sim 135 \mu\text{m}$
2	Img70	--	--	34	2	As a reference in absence of plasma
3	Img74	1.2	3×10^{13}	34	N.A	with a He-Ne laser after the shot
4	Img87	--	--	34	N.A	with a He-Ne laser after the shot
5	Img239	5.4	1.4×10^{14}	26	1	Length of structures $\sim 500 \mu\text{m}$
6	Img240	5.7	1.5×10^{14}	26	1	To show shift in the diffraction fringes, and the diverging trend in the structures
7	Img230	--	--	26	1	As a reference in absence of plasma
E_L , I_L : Energy/Intensity of the heating beam; M = magnification						

Table 6.1: Experimental parameters for figures 6.7 a to g¹

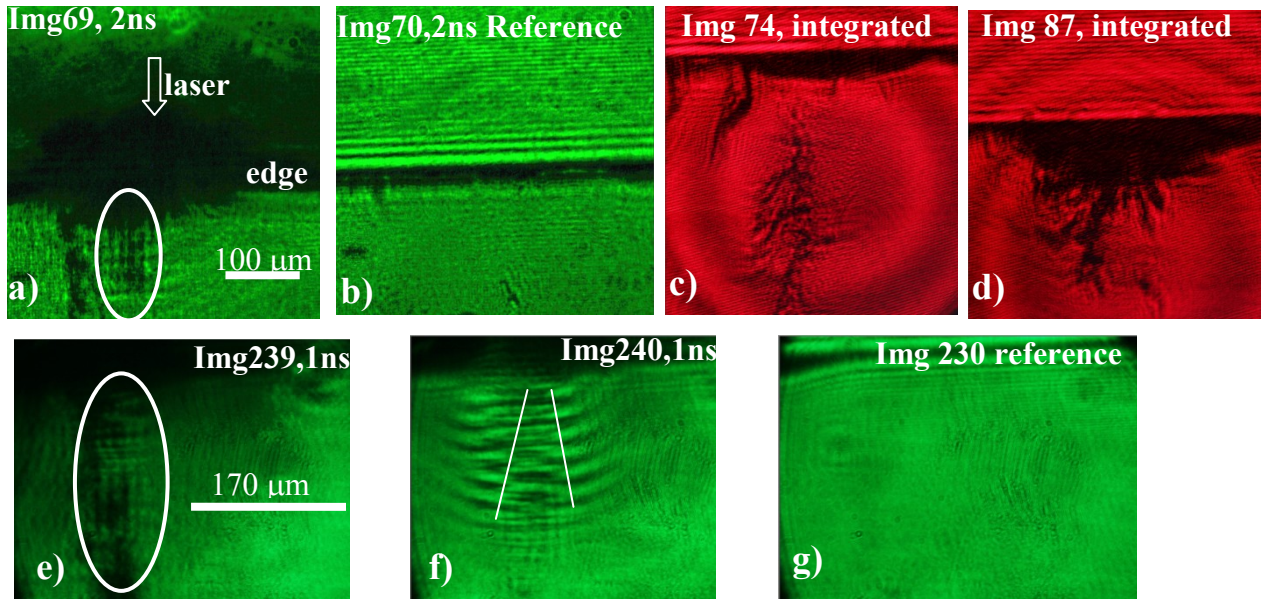


Figure 6.7: (a) Shadowgram recorded showing jet-like structures after a delay of 2 ns (top left) (b) A reference shadowgram taken in absence of plasma (shock) (c, d) Time integrated shadowgrams with a He-Ne laser, much after the experiment (bottom left to right) (e) Shadowgram after 1ns delay (f) Shadowgram showing diverging trend in the structure (g) Reference shadowgram taken in absence of plasma (shock).¹

The possible reasons for the presence of these tree-like structures and long thin structures are discussed here. First the reasons for the generation of the tree-like structures seen in Fig. 6.7 c, d are examined. In the case of laser irradiated plexi-glass targets, similar tree-like structures were reported behind the irradiated region¹⁵² and were attributed to the internal electrical breakdown of the medium due to the intense electrical fields (10^8 V/m). Huge electrical potentials ~ 187 kV were also reported in laser plasmas in similar conditions¹⁵³. For laser intensities around 10^{14} W/cm², the electrical potentials in plasmas was ~ 60 kV.¹⁵⁴ This corresponds to electrical fields of $\sim 6 \times 10^8$ V/cm for typical focal spots of ~ 100 μ m. These electrical fields are higher than the breakdown fields for silica ($E_b \sim 10^8$ V/cm)¹⁵⁵ confirming that the tree like structures are probably due to internal break down of the soda lime glass.

After the explanation of tree-like structures, we consider the possible reasons for the presence of long thin jet-like structures observed in the shadowgrams at delays of 1 and 2 ns. It is experimentally seen that these structures are ~ 130 - 150 μ m long after 2 ns for laser intensity $\sim 5 \times 10^{13}$ W/cm² and when the intensity was increased to $\sim 1.5 \times 10^{14}$ W/cm², their length increased to 500 μ m after 1 ns. In both the cases, the width of channels was < 10 μ m. The presence of ionization is indicated in these shadowgrams in the form of small shift seen in the diffraction pattern (generated due to edge diffraction) at the intersection points. The probable reason for these tracks could either be generation of hot electrons or formation of x-ray hot spots due to the presence of hot spots in the laser beam spatial profile and onset of small scale filamentation instabilities. In the case of filamentation, the local laser intensity can be higher by an order of magnitude and reach $\sim 10^{15}$ W/cm². This can produce upto ~ 10 keV energy. However, range of such electrons is smaller than 100 μ m scale on which the jet-like structures are observed. Next, generation of x-ray hot spots¹⁵⁶ and presence of long thin *collimated* structures in the plasma

corona region have been reported¹⁵⁷. However, it is not clear how x-ray emission can be so directional. Further experiments using laser beams after optical smoothing and different-z targets may be helpful in a better understanding of these observations.

6.4.2 Intricacies in the shadowgraphy experiments

After the analysis of the experimental results, some of the experimental intricacies are discussed here. One question is on the ideal magnification suitable for imaging in these type of experiments. In the case of chirped pulse shadowgraphy experiments, the typical heating and probe pulse durations are sub-ns. The shock front propagates only few μm to tens of μm during this time durations. For example, a shock wave with a velocity $\sim 2 \times 10^6$ cm/s covers ~ 10 μm during 500 ps duration. In order to record movements of this scales, higher magnifications should be used to record the shock front movement properly to be able to estimate the variation in the shock velocity accurately. However, high magnification factor also means very small region at plasma plane is being imaged within the height of the entrance slit of the spectrograph. The dynamics of shock wave can be recorded only when the shock front remains within the entrance slit at that probe delay. However, if the heating beam energy changes from shot to shot, recording the shock front becomes a difficult task. As the laser energy fluctuates the shadow due to shock will be off the entrance slit. So the stability of the laser energy and choosing optimum magnification are crucial issues in these experiments. In our chirped pulse shadowgraphy efforts poor stability of the laser energy was the crucial issue in addition to the spatial quality of the probe beam.

In the case of snap shot shadowgraphy, the shock movement gets integrated during the probe pulse duration. Moreover, as delays used are discrete (1 - 4 ns), the occurrence of the peak

of shock wave velocity around 1 ns is only indicative because the delays are in steps of 1 ns. This means that in reality the peak of the velocity might have occurred between two delays.

6.5 Conclusions

The temporal evolution of shock waves propagating in a transparent glass material (soda lime glass) has been obtained at laser intensities of 10^{13-14} W/cm² using optical shadowgraphy techniques like chirped pulse shadowgraphy (CPS) and snapshot shadowgraphy. Using chirped pulse shadowgraphy temporal profile of shock velocity was obtained over the probe pulse duration. Shock velocities at different delays had been measured using snapshot shadowgraphy for two laser intensities. The measured shock wave velocity had shown a peak value of $\sim 5.5 \times 10^6$ cm/s after a delay of 1 ns for a laser intensity of 1×10^{14} W/cm². This velocity was reduced to $\sim 3 \times 10^6$ cm/s after a delay of 4 ns. The higher transients of the shock velocity observed experimentally was attributed to the generation of small scale hot spots with enhanced local laser intensities and delayed compaction when a compression wave passes through the medium. The presence of jet-like ionization channels seen in these experiments is also interesting phenomena associated probably with the hot spots in the laser beam.

Permissions for reprinting figures

¹ Reprinted from *Shock wave propagation in soda lime glass using optical shadowgraphy* by Y B S R Prasad, S Barnwal, P A Naik, Y Yadav, R Patidar, M P Kamath, A Upadhyay, S Bagchi, A Kumar, A S Joshi and P D Gupta in *Pramana*, 87:9, (2016), DOI: DOI 10.1007/s12043-016-1212-z, with the permission of *Springer*

Chapter 7 : Conclusions and Future Plans

7 Optical probing of laser produced plasmas

Different types of optical diagnostics for studying the laser plasma interaction have been discussed in this thesis. One such diagnostics is time resolved measurements using chirped pulse diagnostics providing few ps time resolution. This technique has been compared with the earlier work carried out using an optical streak camera. The results from a three-channel polaro-interferometer to detect the mega-gauss order magnetic fields generated in ns laser produced plasmas have been discussed. The optical system used in this experiments provides the information about the spatial profiles of the magnetic fields and plasma density in a single shot, and also minimizes the errors due to the non-uniformities in the probe beam. The snap shot shadowgraphy using a second harmonic probe beam to obtain time resolved shock velocity profiles in the soda lime glass has been described. In addition, chirped shadowgraphy has also been tried to obtain continuous shock velocity measurements in a single shot. Discussion about each work along with the future scope is given in the following sections.

7.1 Chirped Pulse Diagnostics

Using a 10 TW Ti:sapphire laser system delivering 45 fs pulses, chirped pulse shadowgraphy (CPS) experiments were conducted to obtain the temporal evolution of plasma expansion velocity. A portion of the output [duration of 200 ps (FWHM), and 20 nm bandwidth] from the pulse stretcher was used as a probe pulse for the CPS experiments. A peak expansion velocity of 1.8×10^7 cm/s, with the velocity profile of 70 ps FWHM was observed.

A cyclic interferometer was used to conduct chirped pulse interferometry to obtain time resolved density profiles at different axial distances. In these interferometry measurements, the presence of diffraction fringes, which were hitherto viewed as unwanted artefacts, was used to estimate plasma expansion velocity. The velocity values obtained from interferometry match quite well with the results obtained from chirped pulse shadowgraphy experiments. Thus, it is demonstrated that by performing the CPI alone, both the density and expansion velocity profiles can be obtained. In both these studies, the temporal resolution was 8 ps.

A future variation of this technique is to use a separate compressor (prism based or grating based), so that the probe beam can be compressed to different pulse durations, keeping the bandwidth intact. Using this compressed probe beam, different diagnostics like chirped pulse interferometry, reflectometry and shadowgraphy can be performed with a much better time resolutions, down to sub-ps if required for the phenomenon under investigation.

7.2 Detection of self generated magnetic fields

Self generated magnetic fields below 1-2 MG have been detected using a three channel polaro-interferometer. These magnetic fields were detected in aluminium plasmas at a laser intensity of $\sim 5 \times 10^{13} \text{ W/cm}^2$, after a delay of 2-3 ns. The magnetic fields were observed to be present even after a delay of 4 ns. These toroidal magnetic fields have been attributed to the large density and temperature gradients present in the laser produced plasmas. Initially, the images were analyzed using different software programs. Later on, a MATLAB program was written a) to carry out the image processing, b) to calculate the spatial profiles of the Faraday rotation angle, c) to estimate the plasma density and magnetic fields.

A future extension of this work could be to study the generation of magnetic fields in two colliding plasmas generated using Fresnel bi-prism. This can be probed with chirped pulse diagnostics to obtain the time resolved information. A continuous temporal evolution of the magnetic fields generated can be obtained by using chirped pulse diagnostics with much better resolution.

7.3 Equation of state studies

Chirped pulse shadowgraphy and snap shot shadowgraphy have been used to obtain the time resolved shock velocity profiles in the soda lime glass at laser intensities of 10^{13-14} W/cm². The higher transients of the shock velocity observed experimentally using the snap shot technique has been attributed to the generation of small scale hot spots and delayed compaction phenomena in the soda lime glass. In addition, jet-like ionization channels were seen in the shadowgraphs at delays of 1 and 2 ns. These have been attributed to x-ray hotspots generated due to small scale filamentation instabilities.

This work can be extended to conduct two-frame optical shadowgraphy experiments to eliminate the errors to due to target's self-shadow problem. Using Fresnel bi-prism, the nanosecond laser beam can be focussed on step targets (Al, Al/Au) and using chirped pulse reflectometry (CPR) the shock arrival at the backside at two different regions can be accurately estimated.

In short, there is a scope to extend the new optical probing techniques developed during this thesis work to many problems of contemporary interest in the field of laser-plasma interaction.

Appendix A : Streak Camera

A.1 Introduction

The conventional optical detectors like bi-planar photo-diode or PIN photo-diodes provide the temporal profile of the light incident on them in the form of an electrical current to be measured on an oscilloscope. Due to the finite inductance in these devices, their typical temporal resolutions are limited to several tens of ps (Hamamatsu R1328U bi-planar photo-tube : 60 ps rise time and 55 ps fall time). Moreover, they cannot provide space resolved information. Streak camera is one such device for high speed photometry to provide 1-D space and continuous time resolution. This Appendix will briefly describe the physical mechanism and various components of a streak camera without going into the electrical circuits. As these are used in laser plasma experiments, triggering mechanisms will also be discussed.

The function of a streak camera is briefly discussed here. The streak camera consists of a streak tube and image intensifier tubes. The light is incident on an entrance slit which is in turn imaged on to a photo cathode. The choice of the photo cathode depends on the wavelength range one is interested to use the streak camera. The following table lists few standard photo-cathode materials and their wavelength range.

No	Photo Cathode	Spectral Range
1	S-20 (Multi alkali)	200 - 850 nm ($\lambda_{\text{max}} \sim 450$ nm)*
2	S1 Ag-O-Cs	450 -1150 nm ($\lambda_{\text{max}} \sim 800$ nm)
3	Au/CsI on Parylene/Nitrocellulose film	soft x-rays 100 eV - 10 keV and UV
* The spectral response depends on the type glass used and cathode material		

Table A.1: *Spectral ranges of different photo-cathodes*

The photo-cathode, as its name implies, generates photo-electrons current, which are proportional to the incident light in both space and time. In case of optical streak cameras the whole streak tube is vacuum sealed. The radiation from the event to be analyzed is imaged on to the entrance slit of the streak camera. These photo-electrons produced are accelerated and imaged on to a phosphor plate. An accelerating grid, placed 1 mm away from the photo-cathode, is used for gating purposes and also for improving the time resolutions ($< 1\text{ps}$). The streak tube also has a focusing electrode to focus the electrons on to the phosphor screen and this decides the spatial resolution of the instrument. The phosphor screen is of aluminized P11 material with peak response at 460 nm. The P11 phosphor and the photo-cathode material are on the inner walls of the sealed glass tube.

The mechanism described till now generates an image of the input slit which is integrated in time. The heart of the streak camera is the sweeping mechanism. For this, the streak tube has two metal electrodes placed in the transverse direction to the path of electrons. By applying a fast ramp voltage on these electrodes, the electrons arriving at different times get deflected by different amount (since voltage at later time will be higher). The mechanism of retrieving temporal information by applying the ramp voltage is shown in the Fig. A-1. The electrons reaching

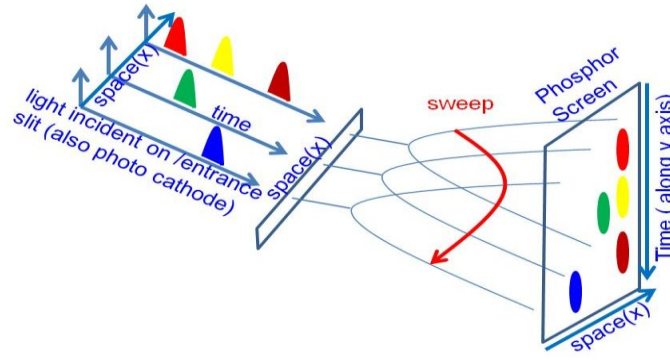


Figure A.1: A schematic depiction of space and time resolved information from a streak camera

at different times on a points along the X-axis(say $x_1, x_2 \dots$) on the slit will be incident on the phosphor at same x_1, x_2 but at different y_1, y_2 (time). The Y-axis is now representing the time information. The separation between these points will depend on the rate of change in ramp voltage with time. Thus the phosphor screen of the streak tube will give a time and space resolved information of the event.

In order to amplify weak light signals, the phosphor output is coupled to an image intensifier tube (optional) through an optical fibre plate placed just outside the streak tube. The image intensifier is a sealed micro-channel plate(MCP). MCP is a bundle of millions of micro-channels ($\sim 6\text{-}10 \mu\text{m}$ dia.) in honeycomb structure made of glass with a semi-conducting inner wall. The inter channel separation is $\sim 15 \mu\text{m}$. When a single incident particle (photon, ion, electron) enters the channel, it generates photo-electrons or secondary electrons that are accelerated towards the rear side maintained at positive high potential (max 1000 V per stage). When the photons from P11 phosphor of the streak tube are incident on the input side of MCP, they generate photo-electrons, which in turn generate secondary electrons. This multiplication factor depends on the voltage applied on MCP. These secondary electrons are then directed

towards another phosphor plate maintained at higher positive potential compared to the output side of MCP (max. ~ 4 kV). This generates a space and time resolved, amplified light output at each point on the phosphor which is proportional to the photons incident on the entrance slit. Typical specifications of the streak camera¹⁵⁸ used in our experiment are listed below in Table A.2.

S.No	Properties	Technical Specification
1	Photo-cathode Type	S-20
2	Photo-cathode spectral response	300-840 nm (S-20)
3	Phosphor area	40 mm dia.
4	Magnification factor	2.2
5	Temporal resolution	5 ps
6	Deflecting plate bandwidth	2.1GHz
7	Spatial resolution	100 μ m
8	Photo-cathode size	25 mm
9	Image magnification	1X
10	Dynamic range	Typically 10-100

Table A.2: *Technical specification of the streak camera*

A.2 Triggering the Streak Camera

As discussed previously, a critical issue in the streak camera to obtain time resolved information is the ramp voltage on a deflecting electrodes. The extremes of the ramp voltage are such that the any information arriving during this time is deflected outside the phosphor region. In fact, a small region of the ramp is chosen such that the rate of change in voltage dv/dt is linear. It is important to ensure that the optical event is occurring during this liner region. The streak

camera also has finite internal delay. So in practice the streak camera is triggered exactly before this internal delay so that optical event can be seen on the phosphor. During the present set of experiments, two methods have been used to trigger the streak camera.

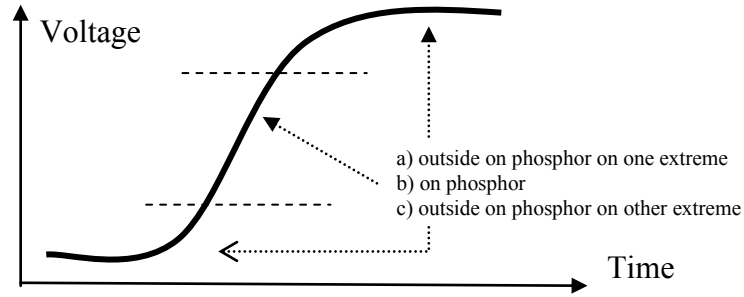


Figure A.2: *Temporal profile of the ramp voltage.*

A.2.1 Using a photo-diode

When the internal delay was within few tens of nanoseconds, a small portion of the main laser beam was detected at an earlier stage of the high power laser system using a bi-planar photo-diode and this signal was used to trigger the streak camera. In order to fine-tune the trigger pulse, a passive delay unit was also used in the path so that one can delay the trigger pulse to streak camera in smaller time steps (0.1 ns - tens of ns).

A.2.2 Using the master clock of the oscillator

To improve the linearity of the ramp voltage, the electrical circuits were replaced by MOSFETs¹⁵⁹. Although this improved the linearity of the voltage pulse, the delay was increased to more than 100 ns. Since using a photo-diode is not practical for delays of this order, another approach was used. The EKSPLA SL223 has a master clock from which it derives the high voltage pulse to control the Pockels cell. It also has a provision for a synchronous output which can be arbitrarily timed. In the present case, a negative delay of 124 ns with respect to the laser output was given to trigger the streak camera. The delay was tuned in fine steps by using a delay generator (DG535 : SRS Stanford Research Systems) with sub ns accuracy. In the case of the 10 TW femto second laser system, triggering for the streak camera was taken from the master clock (D18) of the laser system. This D18 delay could be programmed quite accurately to 1 ns.

A.3 Calibration procedure

The sweep rate of the streak camera was experimentally verified. This was done as follows. As part of the laser plasma experiments, a short duration probe beam was used for diagnostics purposes. This probe was generated by splitting a small portion of the laser beam after amplifier A5. It was relayed upto the plasma chamber using image relay systems. Near the plasma chamber, this probe was converted into its second harmonic wavelength by using a KDP crystal. This second harmonic output was used for calibrating the optical streak camera. The KDP crystal, focussing lens, and the optical fibre holder were all placed on a translational stage.

In order to calibrate the streak camera, the second harmonic output of the probe beam was focused using a plano-convex lens into an optical fibre. The other end of the fibre was placed near the entrance slit of the streak camera which was placed at the rear side of the plasma chamber.

on which the main beam was already imaged. Two streak images were obtained at different heights, one associated with the main laser beam and other one with the probe laser beam. The delay line in the probe beam was adjusted till peaks of these two streak images matched with one another. By moving the translational stage on which the KDP crystal and fibre were placed, by known amount, an additional delay could be introduced between probe and heating beam. By measuring the separation between the peaks of these two laser pulses (in terms of pixels), the calibration factor was calculated.

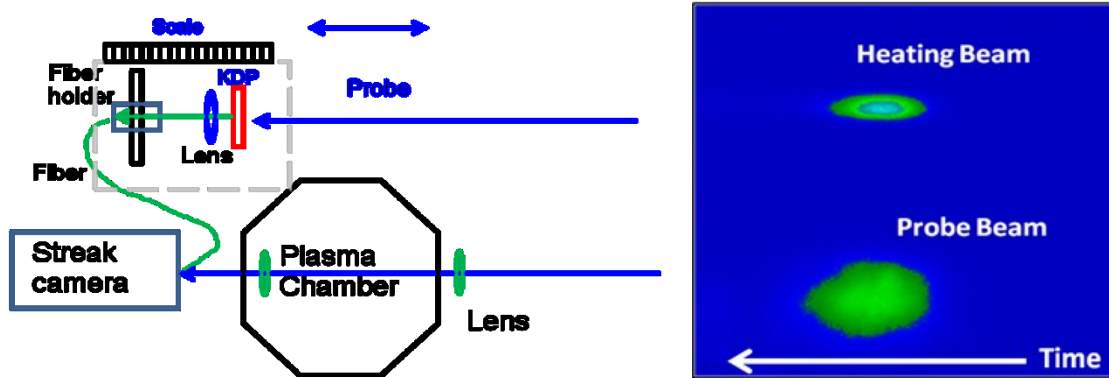


Figure A.3: *Streak camera calibration Procedure*

Appendix B : Abel Inversion

In the case of optical probing of laser produced plasmas, an external probe laser is passed tangentially through the plasmas. The laser plasmas have strong spatial density gradients because of their small spatial dimension. The gradients have a cylindrical (radial) symmetry. As the probe beam passes through the plasma it passes through different regions of plasma density and the effect on the probe will be integrated as it passes through. For example, the phase difference at each point will be accumulated along the propagation direction. In the case of interferometric measurements, the accumulated phase difference will cause a shift in the interference fringe at that point from which a projected electron density can be calculated. Then how to obtain space resolved density information?

The Abel inversion technique is one such method to retrieve the space resolved information, from the *chord integrated* measurements. The important condition in applying the Abel inversion technique is that plasma should exhibit cylindrical symmetry which is satisfied in the case of laser produced plasma. This means the physical parameter being measured, say plasma density only depends on radial distance ' r ', independent of angle ' θ ' for each value of Z distance from the target.

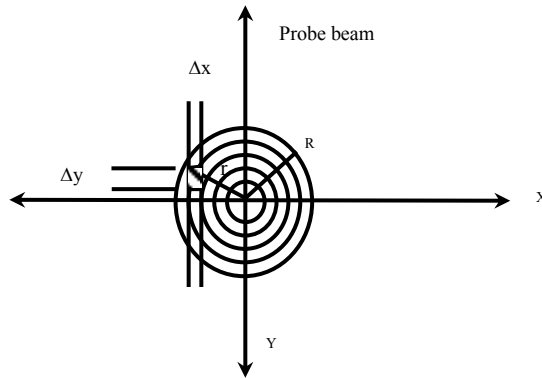


Figure B.1: A schematic diagram of chord integrated measurement^a

In the schematic figure (Fig. B.1), the probe beam is passing along the Y-axis. The heating beam is incident along the Z-axis. Assuming cylindrical symmetry, it can be seen that at each X, the probe beam passes through different volume elements and the changes (phase, attenuation etc.) in the probe beam get integrated along the Y direction.

Let us consider a specific case of measuring the plasma density from the fringe shifts in interferometry. As the probe beam passes through the regions of different plasma densities (corresponding to different refractive indices), the optical path length for the probe beam in the plasma at a distance X from the axis, D(X) can be expressed in terms of the refractive indices as

$$D(X) = 2 \int_0^{y_0} \mu(r) dy \quad \text{--- B-1}$$

By moving from Cartesian to cylindrical coordinate system, the same equation can be rewritten as

$$D(x) = 2 \int_0^{y_0} \frac{\mu(r) * r * dr}{\sqrt{(r^2 - x^2)}} \quad \text{--- B-2}$$

The probe passing through the plasma with this path length is made to interfere with another component of probe beam acting as reference. The change in the path difference between the two beams is caused by the presence of plasmas and this varies for different points across the plasma. This leads to shifts in the interference fringes. The plasma density in the case of homogeneous plasmas can be expressed in terms of the fringe shift δ as follows.

$$n = \frac{(2\pi mc^2)}{L\lambda e^2} \left[\frac{\delta}{\Delta x} \right] \quad \text{--- B-3}$$

where Δx , δ , λ are the fringe width, fringe shift, wavelength of the probe radiation respectively, and L is the length of the plasma column along the probe beam propagation. In the

case of non-homogeneous plasmas, the density estimated from this expression is the space averaged one.

For plasmas with cylindrical symmetry, the projected density can be transformed into radial density profile using the Abel inversion technique. Abel inversion technique inverts the equation (2) by expressing the refractive index $\mu(r)$ in terms of the path length $D(x)$ which can be expressed as

$$\mu(r) = -\frac{1}{\pi} \int_0^R \frac{D'(x)dx}{\sqrt{(x^2 - r^2)}} \quad \text{--- B-4}$$

where $D'(x)$ is $dD(x)/dx$.

The path length $D(x)$ can be expressed in terms of the fringe shift which can be measured from the recorded interference pattern. The equation (4) can be solved using different methods. Solutions using Fourier transformation method or a set of linear equations are common. Expanding the integral equation in terms of linear equations can be expressed as¹⁶⁰

$$\mu(r) = \sum_{i=k}^N b_{ik} D(x_k) \quad \text{--- B-5}$$

This calculation is recursive in nature and starts from the outermost cylinder where plasma is absent and the fringes are undistorted (no shift) and proceeds towards the axis where the fringe shift is maximum. The plasma has been divided into number of mesh cells with equal spatial separation. The coefficients b_{ik} associate a weight factor to each element along the integration. Using this, the radial profile of the refractive index can be estimated. By doing a little mathematical simplification it can be also shown that plasma density can be expressed as

$$n_e(r) = 2\lambda n_c \sum_{i=k}^N b_{ik} \delta(x_k) \quad \text{--- B-6}$$

where n_c and δ are the critical density for the laser with wavelength λ and the fringe shift respectively.

A MATLAB program written in our Laser plasma division is used for this purpose. The set of coefficients is taken from the literature¹⁶¹. This program is used as part of another MATLAB program to calculate the self generated magnetic fields and the details are given as Appendix C.

Appendix C : Calculation of Magnetic Fields

C.1 Introduction

Self generated magnetic fields of order of several megagauss are reported in laser produced plasmas. Depending on the laser pulse duration, intensity, polarization etc., magnetic fields of different nature are generated. In the case of nanosecond plasmas, observations of toroidal magnetic fields are reported from many laboratories⁸⁸. In the case of femtosecond, circularly polarized laser pulses, at intensities up to 10^{19} W/cm² interacting with under-dense helium plasma, magnetic fields of 7 MG (< 3 ps) have been reported by Najmudin *et al*²⁶. These fields are attributed to the Inverse Faraday Effect (IFE) generated by fast electrons spiralling around the axis of the channel created by the laser field.

To detect magnetic fields generated in laser plasmas, Faraday rotation method is the standard technique used. In this method a linearly polarized laser probe beam is passed through the interaction region and the plane of the probe beam is rotated by an angle ' θ ' which depends on the local plasma density and the magnetic field expressed as

$$\theta(\text{deg}) = 1.5\lambda_p^2(\text{microns}) \int \frac{n(\text{cm}^{-3})B_y(\text{MG})dz(\text{microns})}{10^{21}\sqrt{1-n/n_c}}, \quad \text{..... C-1}$$

where λ_p is the probe beam wavelength, n is the plasma electron density, and n_c is the critical density for the probing beam expressed as

$$n_c = \frac{m\omega^2}{4\pi e^2} = \frac{\pi mc^2}{e^2 \lambda^2}. \quad \text{..... C-2}$$

$B_y = B \cos \phi$ is the component of the magnetic field along the direction of propagation of probe beam. For a toroidal magnetic field, ϕ varies from 0° at the top and bottom edges of the plasma, to 90° at the level of the axis of the heating beam.

As it is evident from equation (1), the rotation angle depends on the plasma density also. Hence, interferometric measurements for density are also carried as part of the magnetic field measurements. Experimentally, the rotation angle is measured by detecting the intensity of the transmitted component of the probe beam passing through a plasma placed between a pair of crossed polarizers. Experiments were carried out at Laser Plasma Division of RRCAT to detect the presence of magnetic fields using three channel polaro-interferometer. The details about this experiment are given in Chapter 5 of this thesis. The discussion presented here is about the analysis of the images recorded and retrieval of the space resolved density and magnetic field profiles from the image recorded. Initially this was done using a set of computer programs for Image view and Analysis (PROMISE / TRILOCHAN developed by Shri H.S.Vora, LSED at RRCAT), calculations (spreadsheets), and curve fitting and plotting software. In order to simplify this, a MATLAB program has been written by us. The description of this program is given here. The actual program is given here and also can be downloaded from Researchgate website¹⁶².

C.2 Steps of the program

- a. The output from the three channel polaro-interferometer is a single image recorded using DSLR camera with large format chip (Fig. C.1). The image consists of three channels i.e.

polarogram, interferogram and shadowgram. The image is read from memory and shown on the screen using two MALAB functions : *imread* and *imshow*.

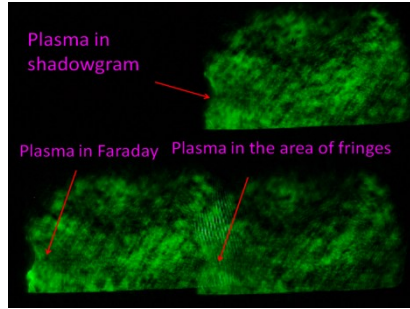


Figure C.1: CCD picture showing the three simultaneously recorded channels : Polarogram (lower right), Interferogram (overlapping region of lower images), and shadowgram (top).^a

- b. The regions where the Faraday rotation is centered is to be identified for estimating the self generated magnetic fields. A rectangular region is selected (shown as two pink dots in the Fig. C.2 below, in the lower left corner) interactively using *ginput(2)* function.

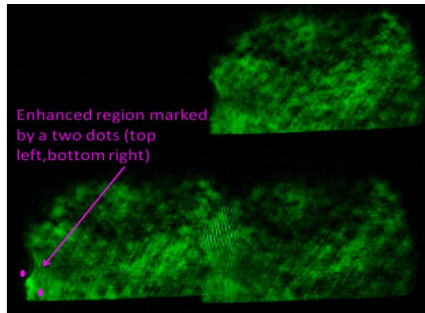


Figure C.2: Selecting a enhanced region in Faraday channel.^a

- c. Once the region is selected in the Faraday channel, the corresponding region of the interferogram is displayed (Fig. C.3 below) with suitable magnification on the screen using the *imcrop*, *imshow* functions with suitable parameters. In order to do this, the offset between the channels is to be known in advance. This is required as locating and marking the fringes in full image is quite difficult. This offset is measured in experiments

by imaging a sharp object like pin. The pixel coordinates of the tip of the pin (or a cross-wire) are used for calculating the offset.

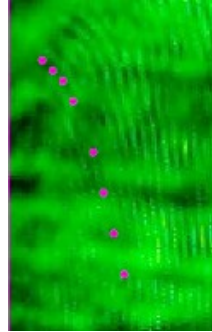


Figure C.3: *A magnified view of interference fringes in which one fringe is tracked.^a*

- d. In the interference fringes displayed, a fringe is then chosen and the coordinates of this fringe are stored by clicking on different parts of the fringe using a mouse using the ***ginput*** function. The selection starts from location where fringe shift is maximum and ends where the fringe shift becomes zero. The selection ends when the "Enter" key is pressed. (in some versions one has to enter twice at same location. when ***ginput*** function receives same points twice, it marks the end and returns to the calculations). The plasma density 'n' calculated in terms of the fringe shift 'δ' as

$$n = \frac{2\pi mc^2 \delta}{\lambda_p e^2 L \Delta x} \quad \text{..... C-7}$$

gives an average electron density. Here m, λ_p , L, and Δx are electron mass, wavelength of the probe, size of the plasma and fringe width respectively. Abel inversion is used out to get space resolved density profile. In order to do Abel inversion one generates fringe shift data at equi distance points by using interpolation technique on experimental fringe shift data measured at discrete points. Abel inversion technique gives a fringe shift at each

radial point. The electron density calculated like this is shown in Fig. C4 belong along with the fringe shifts. The radial density profile is calculated from Abel data $f_n(r)$ as¹³⁵

$$n(r) = \frac{f_n(r)}{4.46 \times 10^{-14} L \lambda} \quad \text{..... C-8}$$

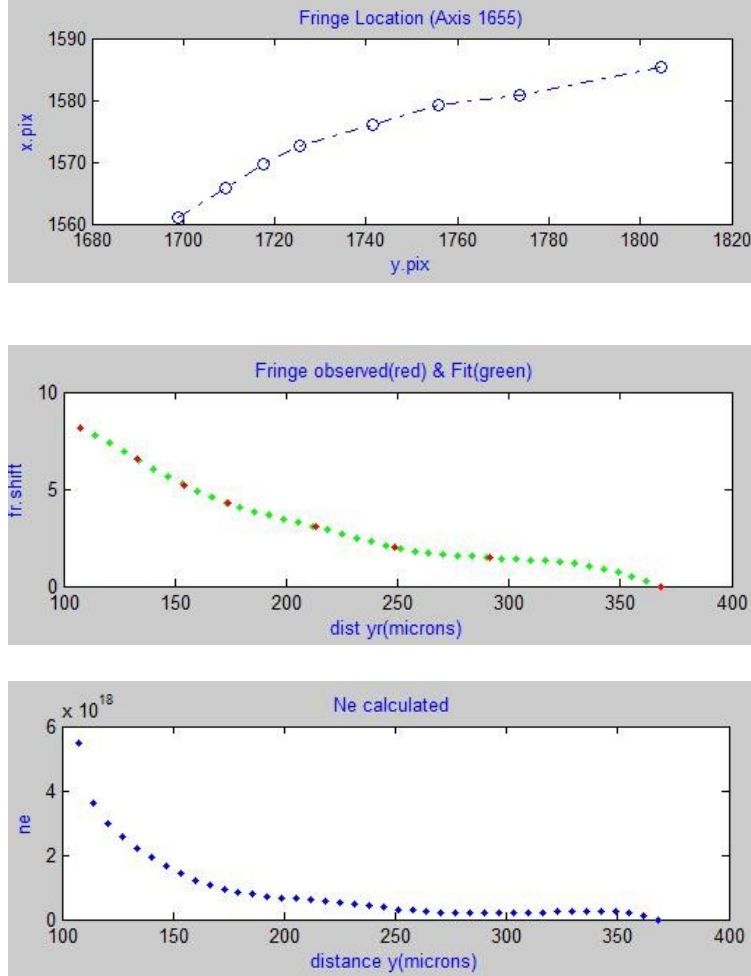


Figure C.4: *The fringe shift of a marked fringe and the electron density calculated.^a*

- e. Now the intensity data of the Faraday channel (I_p) and shadowgram (I_s) at points corresponding to the selected interference fringe (vertical line) are read from the image

file and the angle of rotation is calculated from the ratio I_p/I_s of these intensities. Since

$I_p/I_s = \tan^2((\theta_0 \pm \theta) \cot^2 \theta_0)$, one gets the Faraday rotation angle is expressed as

$$\theta = \tan^{-1} \left(\left(\sqrt{I_p/I_s} \right) * \tan(\theta_0) \right) \pm \theta_0 \quad \text{.....C-9}$$

- f. From the rotation angle data along this line, the normalized rotation angle (θ/y) values were calculated, fitted iteratively with spline / curve fitting, and this data is used for Abel inversion purposes, to retrieve the product of the the magnetic field (B) as¹³⁵

$$B(r) = \frac{29.73 * r * f_B(r)}{\lambda * f_n(r)} \quad \text{.....C-9}$$

This process is repeated for next fringe.

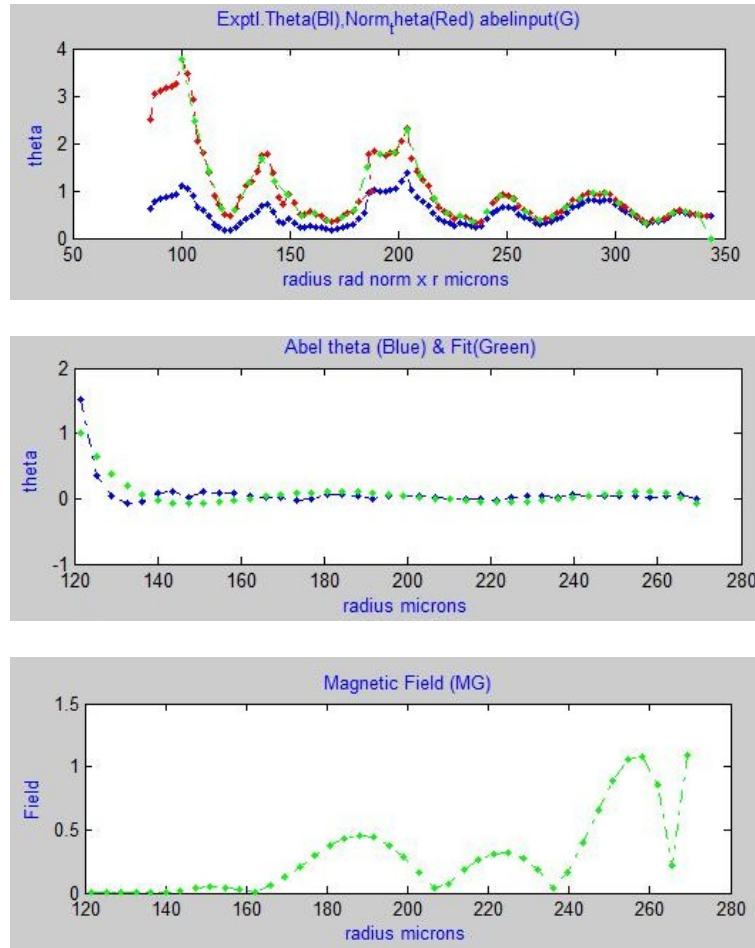


Figure C.5: *The experimentally measured Faraday rotation angle and the magnetic fields.*^a

Permissions for reprinting figures

^a Reprinted from *Calculation of self-generated magnetic fields in laser produced plasmas* by Y. B. S. R. Prasad, S. Barnwal, P. A. Naik, P. D. Gupta, E. A. Bolkhovitinov, and A. A. Rupasov , Journal of Russian Laser Research (2015) 36: 395, doi:10.1007/s10946-015-9516-x with the permission of *Springer*

C.3 Program

C.3.1 Two Dimensional Profile of the Rotation Angle

```
% ----Start  PROGRAM (MATLAB 2008A)
clear all;
clc

axdist=[]; rad=[];  theta=[]; % axial, radial dist & theta calculated at
                               % discret points using IF/Is formula

Int_Polari=[]; Int_Shadow=[];
targetfront = 628; rzero = 1648;
xoffset_ptoi = +882 ; yoffset_ptoi = 9 ; %pixels
xoffset_ptos = +918 ; yoffset_ptos = -969 ; %pixels

fid = fopen('rotangle.txt','w');
%-----
I=imread('F:\2.7 5_06 7J.JPG'); % <=====

K = menu('mark TopLeft & BottomRight corner of p region','Click to mark');

imshow(I);[px py]=ginput(2);% TopLft,BottmRight pixls of enhanced region

%K=menu('Click to continue','Continue');

%=====Calculating the rotation angle =====
theta0=1.4 ; % decrossing angle in degrees change here

theta0rad=(theta0*pi)/180; % from degrees to radians

G=I( :, :,2); % get only intensity data of Green pixels in image

curr_x=px(1) ;i=1;

while curr_x < px(2)

axdist(i)= (curr_x - targetfront)*6.4/2.6; % in microns

curr_y=py(1) ;j=1;

while curr_y < py(2) % corr to fringe begin to end
    rad(j) =(curr_y - rzero)*(6.4/2.6); % y_pixel to rad. distance
    (microns)<=====
    Int_Polari(1)=G(int16(curr_y),int16(curr_x)) ;
    Int_Shadow(1)=G(int16(curr_y+ yoffset_ptos),int16(curr_x+xoffset_ptos)) ;

    if (Int_Shadow(1)==0) Int_Shadow(1) =1; end;
    t1 = sqrt(Int_Polari(1)/Int_Shadow(1));
    t2 = tan(theta0rad)*t1 ;
    t3 = atan(t2)*180/pi; % degree
    t4 = t3-theta0; % in degrees
```

```

theta= abs(t4); % in degrees

fprintf(fid,'%8.4f %8.4f %8.4f\n',axdist(i),rad(j),theta);
j=j+1;curr_y=curr_y+1;% pixel by pixel increasing
end;
i=i+1;curr_x = curr_x + 1;% next line away from target
end
fclose(fid);

```

C.3.2 Calculation of the Density and Magnetic Fields

```

% PROGRAM SGMF (MATLAB 2008A)
% calculate magnetic field from polarointerferometer image
% You have to specify the image file to be loaded in the program itself.
% Now when you run the program
% a) it will show the full three channel image
% b) you select top left and bottom right corners of enhanced region[px,py]
%     (magnetic field) in lower part of the Faraday/Polari channel which
%     is at lower left side
% c) it will be show the corresponding fringe region in a new window
%     for this you need to know the offset between Faraday and shaodow
%     and Faraday and Interference. Measure experimentally and store
%     xoffset_ptos, yoffset_ptos, xoffset_ptoi, yoffset_ptoi

% d) you maximize the window and mark a fringe by clicking on different
%     points[fx fy],starting from top where fringe shift=max to bottom
%     where fringe shift is zero. Once you reach point where shift=0
%     mark by last point and press enter. This will collect all discrete
%     points on the fringe.
% e) from this fringe shift @ 41 equi spaced points are generated. This is
%     given as input to Abel inversion and we get radial density profile
%
% f) now we have to get the rotation angle corresponding for this fringe.
%     for a fringe
%     unshifted point(x,y):to get distance from target (x) and max rad.dist
%     top max shifted:(y) to get min. radial distance( x is same as above)
%     at the corresponding points in faraday and shadow channel
%     we take the ratios of  $I_F/I_S$  pixel strength(intensity)
%     get the rotation angle  $\theta$ . get normalized rotaion angle  $\theta/y$ 
%     get the Abel inversion output. get the Spline fitting for  $\theta$ 
% g) from the  $\theta$  and density get the radial profile of B Magnetic field

clear all;
clc;

% -----declarations ---
xr = [] ; yr = [] ; % fringe shift & radial distance in
                    % pixls at discrete pts(mouse click)
x  = [] ; y  = [] ; % fringe shift and radial distance in
                    % pixels at 41 equi-dist pts (spline

```

```

                                %fit from xr yr)

abel=[];                        % fringe shifts 41 given as input to
                                % abel inversion
frabelout= []; frabeloutfit= []; % abel inversion output in form of
                                % space resolved ref.indices
den=[];                         % density calculated from space
                                % resolved fringe shifts

Int_Polari = [];
Int_Shadow  = [];              % intensities inthe p and s channel

rad=[]; theta = [];           % radial dist & theta calculated at
                                % discret points using IF/Is formula
                                % at fringe base from <ymin - ymax>

norm_x=[];
norm_theta = [];              % radial dist & normalized theta
                                % (theta / (r/Rmax) upto Rmax where
                                % theta almost goes to zero

r=[]; theta41=[];             % radial dist & theta for region
                                % theta_max to 0 (ignoring region
                                % before theta_max)

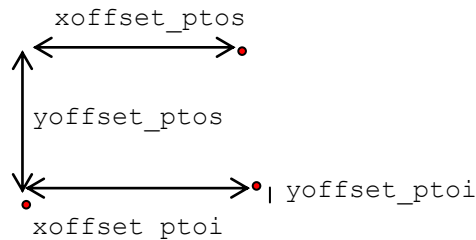
rotabelout = [];              % abel inversion out for rot.angle
                                % (input to Abel inversion =
                                % theta/(r/Rmax) )

abelP = [];
rotabeloutfit=[];             % coeffs of curve fitting for the
                                % abeloutput (theta) and the fitted
                                % abelout

denfit2 = [];                 % fitted densities spline

B=[]; B1=[];                  % calculated magnetic fields
% these are the values of offset (in pixels ) between interometry(i) and
%channel shadow(s) with respect to Polari(p) channel
xoffset_ptoi = 882 ;
yoffset_ptoi = 9 ;
xoffset_ptos = 918 ;
yoffset_ptos = -969 ;

```



```

plasmasize = 210*6.4e-4/2.6 ; % in cm
lamda      = 0.532e-4      ; %in cm

rzero      = 1655 ; %pixel of laser axis or center of the plasma
pixelsize  = 6.4 ; %in microns
demag      = 2.6 ; %demagnification factor image to plasma plane
fid = fopen('density.txt','w');
%-----
I=imread('F:\3.1 5_14.JPG');
K = menu('mark TopLeft & BottomRight corner of p region','Click to mark');
imshow(I);[px py]=ginput(2); % up.left,low.right pixel mf regions polari

%display corr.region of fringes

K = menu('Click with Mouse on different points on one fringe from top (max
shift)to bottom(shift=0),press Enter to finish','Continue');

I2=imcrop(I,[px(1)+xoffset_ptoi py(1)+yoffset_ptoi (px(2)-px(1)) (py(2)-
py(1))] );

imshow(I2); %display region of fringes corresponding to region marked

[fx fy] = ginput; % discrete pixel coordinates of fringe mouse click

nof1 = length(fx); % number of points marked

K = menu('Click to start fitting ','Continue');% show and wait

subplot(3,2,1);plot(py(1)+yoffset_ptoi+fy,px(1)+xoffset_ptoi+fx,'-.oB');
title(['Fringe Location (Axis 1655)'],'color','b');
xlabel('y.pix','color','B');ylabel('x.pix','color','B');

K = menu('Click on button to start fitting ','Continue');% show and wait

j = length(fx); % no of points marked on fringe

for i = 1: length(fx)
    if ( i< length(fx) )
        if ((fx(i) > fx(i+1)) ) % if fringe shift is not negative
            j=i ; break;
        end;
    end;
end;

nof = j ; % only upto fringe points with +ve shift

for i = 1 : nof % 1655 is the r = 0 axis % <=====
    yr(i)=(py(1)+yoffset_ptoi+fy(i)-rzero)*(pixelsize/demag) ;% distance yr(cm)
    xr(i)= abs ( fx(i)-fx(nof) ) / 3.0 ; % shift (fringes)
end;

```

```

    dr1=abs(yr(1)-yr(nof))/40 ; % get 41 equispaced pts from yr

for i = 1:41
    y(i)= yr(1) + (i-1)*dr1 ; % // equispaced distance (cm)
    x(i) = spline(yr,xr,y(i)); % shift in fringes
end;

subplot(3,2,2); plot(y*10000,x,'.G',yr*10000,xr,'.R');
title('Fringe observed(red) & Fit(green) ','color','B');
xlabel('dist yr(microns)','color','B');ylabel('fr.shift','color','B');

% now let us call abel inversion process function which takes 41 fringes
shifts as input and density as output

abel = x ;
abel(41)=0.0; %last element
frabelout=funabelinv(abel); % Abel output for fringe
den = frabelout/(4.46e-14*plasmasize*lamda); %ne from Abel output

subplot(3,2,3);plot(y*10000,den,'.b');
title(['Ne calculated ','color','B']);
xlabel('distance y(microns)','color','B');ylabel('ne','color','B');

fprintf(fid,'Distance From Target Surface (microns) : ');
fprintf(fid,'%8.4f\n', (px(1)+fx(nof1)-628)*6.4/2.6); % in microns
%622 is the target surface in Faraday channel

%=====CALCULATING THE THETA MEASURED =====
xp=px(1)+fx(nof) ; % X_Pixel value in Faraday corr to fringe lowest point

ypmin = py(1)+fy(1); % Y_Pixel in Faraday to read IF
xs=xp+xoffset_ptos; % X_Pixel value in Shadow corr to fringe
ysmin=ypmin+yoffset_ptos; % Y_Pixel in Shadow to read Is

theta0=1.4 ; % decrossing angle in degrees change here
theta0rad=(theta0*pi)/180; % from degrees to radians

curr_y=ypmin ;i=1;
% convert the RGB image to Green only image for easy processing
G=I( :, :,2); % get only intensity data of Green pixels in image

tan_theta_0 = tan(theta_0_in_rad); % tan of theta_0 in radians

while curr_y < py(1)+fy(nof) % corr to fringe begin to end
    rad(i)=(curr_y-rzero)*( pixelsize/demag); % y_pixel to rad. distance
    (cm)<=====
    Int_Polari(i) = G(int16(curr_y),int16(xp)) ;
    Int_Shadow(i) = G(int16(curr_y+ yoffset_ptos),int16(xs)) ;

    if (Int_Shadow(i) == 0) Int_Shadow(i)=1; end; % to avoid div by zero error

```

```

t1 = sqrt (Int_Polari(i)/Int_Shadow(i));
t2 = tan(theta0rad)*t1 ;
t3 = atan(t2)*180/pi; % degree
t4 = abs(t3-theta0); % in degrees
theta(i)= t4; % in degrees
curr_y=curr_y+1; % pixel by pixel increasing
j1=i;
i=i+1;
end;

Rmin= rad(1); Rmax= rad(j1); % rad.dist(cm) from theta max-frng_end

i =1;
while ( rad(i) < Rmax )
    norm_x(i) = rad(i);
    norm_theta(i) = theta(i) / (rad(i)/Rmax) ;
    i=i+1;
end;

% start the calculation only from the max.rot.angle
[maxtheta imax] = max(norm_theta); Rmin= rad(imax);

dR=(Rmax-Rmin)/40;
for i = 1: 41
    r(i)= Rmin + (i-1)*dR; end; % 41 rad.dist in cm

theta41=spline(norm_x,norm_theta,r); % norm_theta at 41 points
theta41(41)=0;

rotabelout=funabelinv(theta41);%output of Abel Invn for rotn angle
norm_x(41)=norm_x(40)+dR;

subplot(3,2,4);
plot (rad*10000,theta,'-..b',norm_x*10000,norm_theta,'-..r',r*10000, theta41,
'-..g');
title(['Expt1.Theta(B1),Norm_theta(Red) abelinput(G)'],'color','B');
xlabel('radius rad norm x r
microns','color','B');ylabel('theta','color','B');

N = 1;
while ( N > 0 ) %abc2 % smoothing the abelout
M = menu('Choose poly.order to fit','1','2','3','4','5','6','7','8','9');
abelP = polyfit(r,rotabelout,M); % fit rotn angle with a polynomials
rotabeloutfit=polyval(abelP,r); %generate input for theta abel inversion
subplot(3,2,5);plot (r*10000,rotabelout,'-..b',r*10000,rotabeloutfit,'.G');
title([' Abel theta (Blue) & Fit(Green)'],'color','B');
xlabel('radius microns','color','B'); ylabel('theta ','color','B');
N = menu('Pause','Try diff degree','Last fit is OK');
if ( N == 2 ) break; end;
end;

denfit2=spline(y,den,r);frabeloutfit=spline(y,frabelout,r);
for i=1:41

```



```

B(i)=29.73*r(i)*abs(rotabeloutfit(i))/(plasmasize*lamda*frabeloutfit(i));
end;

subplot(3,2,6); plot(r*10000,B/1e6,'-..g');
title(['Magnetic Field (MG)'], 'color', 'B');
xlabel('radius microns', 'color', 'B'); ylabel('Field', 'color', 'B');

fprintf(fid, '\n radial distance r(i) (microns)\n');

fprintf(fid, '\n %6.4f', r*10000);
fprintf(fid, '\n \n Density at points where Abel theta is available');
fprintf(fid, '\n %10.4e', denfit2);
fprintf(fid, '\n \n Abel inversion angle values for getting coefficients');
fprintf(fid, '\n %6.4f', rotabelout);
fprintf(fid, '\n \n Abel inversion angle values (Fit)');
fprintf(fid, '\n %6.4f', rotabeloutfit);
fprintf(fid, '\n Magnetic field (MG)\n \n');
fprintf(fid, '\n %10.4e', B/1e6);
status = fclose(fid);

```

% Program for Abel Inversion using coefficients given in Dhreshwar et al's report

% Program name : Abelinv

```

function [abelout] = funabelinv(fs)
% Read the Abel Coefficients from the 1-D array stored in Abel.dat ascii file
fid=fopen('abel.dat','r');
coef=fscanf(fid, '%f', 861);
status=fclose(fid);
% Write the coefficients to a 41x41 Abel coefficient matrix A
k = 0;
A = [];
mu = [];
eps = [];
for i = 1:41
    for j = i:41
        k = k + 1;
        A(j,i) = coef(k);
    end
end
% Abel Inversion begins
for i = 1:41
    sum = 0;
    n = i;
    k = i;

```

```

    for j = n : 41
        sum = sum + A(j,i) * fs(j);
    end
    mu(k) = sum;

end
% pass the array out through abelout array
    abelout = mu ;
end
% End of the program

```

ps: These programs are compatible with MATLAB version 2008a

References

- ¹ T. Maiman, *Nature* **187**, 493 (1960).
- ² F. Jin, K. Gabel, M. C. Richardson, M. Kado. A. F. Vasil'ev, D. Salzmann, *Proc. of the SPIE* **2015**, 151 (1994).
- ³ A.Krol, A. Ikhlef, J. C. Kieffer, D. A. Bassano, C. C. Chamberlain, Z. Jiang, H. Pépin and S. C. Prasad, *Med. Phys.* **24**, 725 (1997).
- ⁴ D.Strickland and G. Mourou, *Opt. Comm.* **56**, 219 (1985).
- ⁵ A.J. Gonsalves, K. Nakamura, J. Daniels, H.S. Mao, C. Benedetti, C.B. Schroeder, Cs.Tóth, J. van Tilborg, D.E. Mittelberger, S.S. Bulanov, J.L. Vay, C.G.R. Geddes, E. Esarey and W.P. Leemans, *Phys. of Plasmas* **22**, 056703 (2015).
- ⁶ J. Workman, M. Nantel, A. Maksimchuk and D. Umstadter, *Appl. Phys. Lett.* **70**, 312 (1997);
- ⁷ Z. Chang, *Phys. Rev. Lett.* **80**, 1795 (1998).
- ⁸ G. Mainfray and G. Manus, *Reports on Progress in Phys.* **54**, 1333 (1991).
- ⁹ G.M. Weyl "Physics of Laser-Induced Breakdown" chap. 1 from "*Laser Induced Plasmas and Applications*" ed. L.J Radziemski and D. A. Cremers, pub.by Marcel Dekker Inc., (1989).
- ¹⁰ M. V. Ammosov, N. B. Delone, and V. P. Krainov, *Soviet Physics, J. Exp. and Theoretical Phys.* **64**, 1191 (1986); N. B. Delone and V. P. Krainov, "*Multiphoton processes in atoms*," Springer Verlag, Heidelberg, 2nd edition, (1994).
- ¹¹ H. A. Bethe and E. E. Salpeter, "*Quantum mechanics of one- and two electron atoms*," Plenum, New York, 1977.
- ¹² W. L. Kruer, "*The Physics of Laser Plasma Interactions*", Addison-Wesley, New York (1988).
- ¹³ F.F. Chen, "*Introduction to Plasma Physics*", Second edition, Plenum Press (1984).
- ¹⁴ C.E. Max, "Physics of the Coronal Plasma ill Laser Fusion Targets," in *Laser Plasma Interaction*, ed. R. Balian and J.C. Adam (Les Houehes, Session XXXIV, North-Holland, 1982).
- ¹⁵ E. Louzon, A. Feigel, Y. Franka, E. Raicher, M. Klapisch, P. Mandelbaum, I. Levy, G. Hurvitz, Y. Ehrlich, M. Frankel, S. Mamana, Z. Henis *High Energy Density Physics* **7** 124 (2011).
- ¹⁶ Kruer W.L. , "*Theoretical interpretations of Enhanced Laser absorption*", Chapter 1 from "Progress in Lasers and Laser fusion" , Ed. Kursunoglu Behram, Springer, New York (1975); Garban-Labaune, C., E. Fabre, C. E. Max, R. Fabbro, F. Amiranoff, J. Virmont, M. Weinfeld, and A. Michard. *Phys. Rev. Lett* **48**, 1018-1021 (1982).
- ¹⁷ C. E. Turcu and J. B. Dance, "*X-Rays from Laser Plasmas: Generation and Applications*" Wiley, New York (1999).
- ¹⁸ T. W. Johnston, and J. M. Dawson, *Phys. Fluids* **16**, 722 (1973).
- ¹⁹ J. McAlister and E. A. Stern, *Phys. Rev.* **22**, 1599 (1963).
- ²⁰ L. D. Landau, E. M. Lifshitz, and L. P. Pitaevskii, "*Course of theoretical physics: physical kinetics*", vol. X (Pergamon Press, 1981).
- ²¹ D.G. Colombant and W.M. Manheimer, *Phys. Fluids* **23**, 1377 (1975).
- ²² F. Brunel, *Phys. Rev. Lett.*, **59**, 52 (1987).
- ²³ W. L. Kruer, and K. Estabrook, *Physics of Fluids*, **28**, 430 (1985).
- ²⁴ P. Gibbon, "*Short Pulse Laser Interactions with Matter*", Imperial College Press, London (2007).
- ²⁵ H. Popescu, S. D. Baton, F. Amiranoff, C. Rousseaux, M. Rabec Le Gloahec, J. J. Santos, L. Gremillet, M. Koenig, E. Martinolli, T. Hall, J. C. Adam, A. Heron and D. Batani, *Physics of Plasmas* **12**, 063106 (2005). and also S. D. Baton, J. J. Santos, F. Amiranoff, H. Popescu, L. Gremillet, M. Koenig, E. Martinolli, O. Guilhaud, C. Rousseaux, M. Rabec Le Gloahec, T. Hall, D. Batani, E. Perelli, F. Scianitti and T. E. Cowan, *Phys. Rev. Lett* **91**, 105001-1 (2003).
- ²⁶ Z. Najmudin, M. Tatarakis, A. Pukhov, E. L. Clark, R. J. Clarke, A. E. Dangor, J. Faure, V. Malka, D. Neely, M. I. K. Santala, and K. Krushelnick, *Phys. Rev. Lett* **87**, 215004 (2001).

-
- ²⁷ C.A. Cecchetti, M. Borghesi, J.Fuchs, G.Schurtz, S.Kar et al, Phys. of Plasmas **16**, 043102 (2009) .
- ²⁸ L. Bierman, Zs.f. Naturforsch. **5a** (1950).
- ²⁹ J.Stamper, K. Papadopoulos, R.N. Sudan, S.O. Dean, E.A. McLean and J.M. Dawson, Phys. Rev. Lett. **26**, 1012 (1971).
- ³⁰ A. Hasegawa, M.Y. Yu, P.K. Shukla and K.H. Spatschek, Phys. Rev. Lett. **41**, 1656 (1978).
- ³¹ R. Kolodner and E.Yablonovitch, Phys. Rev. Lett. **43**, 1402 (1979).
- ³² Y.Sakagami, Phys. Rev. Lett. **42**, 839 (1979).
- ³³ J.J. Thomson, C.E. Max, K. Estabrook, Phys. Rev. Lett. **35**, 663 (1975).
- ³⁴ S. Ali, J. R. Davies, and J. T. Mendonca, Phys. Rev. Lett. **105**, 035001 (2010).
- ³⁵ E. W. Weibel, Phys. Rev. Lett. **2**, 83 (1959).
- ³⁶ M. Borghesi, A.J. MacKinnon, L. Barringer, R. Gaillard, L.A. Gizzi, C.Meyer and O. Willi, Phys. Rev. Lett. **78**, 879 (1997).
- ³⁷ A. Pukhov and J. Meyer-ter-Vehn, Phys. Rev. Lett. **76**, 3975 (1996).
- ³⁸ A. Pukhov and J. Meyer-ter-Vehn, Phys. Rev. Lett. **79**, 2686 (1997).
- ³⁹ U. Wagner, M. Tatarakis, A. Gopal, F. N. Beg, E. L. Clark, A. E. Dangor, R. G. Evans, M. G. Haines, S. P. D. Mangles, P. A. Norreys, M.S. Wei, M. Zepf and K. Krushelnick Phys. Rev. E **70**, 026401 (2004).
- ⁴⁰ T. J. Ahrens, *Methods of Experimental Physics* Vol. 24, Part A, ed. C. G. Sammis and T. L. Henyey, Academic Press, Orlando, FL, USA, p. 185 (1987).
- ⁴¹ F. H. Shu, *The Physics of Astrophysics*, vol II Gas Dynamics, University Science Books, Sausalito, CA, USA, p 493 (1992).
- ⁴² S. Pfalzner , *An Introduction to Inertial Confinement Fusion* (Taylor & Francis 2006).
- ⁴³ R. Jeanloz, P. M. Celliers, G. W. Collins, J. H. Eggert, K. K. M. Lee, R. S. McWilliams, S. Brygoo, and P. Loubeyre, PNAS **104**, 9172 (2007).
- ⁴⁴ W. J. Nellis, A. C. Mitchell, M. van Thiel, G. J. Devine, R. J. Trainor, and N. Brown, J. Chem. Phys. **79**, 1480 (1983).
- ⁴⁵ N. C. Holmes, M. Ross, and W. J. Nellis, Phys. Rev. B **52**, 15835 (1995).
- ⁴⁶ G. T. Leifeste, Sandia's Shock Physics Capabilities for National Security Applications. No. SAND2015-3008PE. Sandia National Laboratories (SNL-NM), Albuquerque, NM (United States), 2015.
- ⁴⁷ A. S. Vladimirov, N. P. Voloshin, V. N. Nogin, A. V. Petrovtsev, and V. A.Simonenko JETP Lett., **39**, 82 (1984).
- ⁴⁸ A.L. Kritcher , T. Döppner, D. Swift, J. Hawreliak, G. Collins, J. Nilsen, B. Bachmann, E. Dewald, D. Strozzi, S. Felker, O.L. Landen, O. Jones, C. Thomas, J. Hammera, C. Keane, H.J. Lee, S.H. Glenzer, S. Rothman, D. Chapman, D. Kraus, P. Neumayer, R.W. Falcone, High Ene. Dens. Phys. **10**, 27 (2014).
- ⁴⁹ R. Fabro, E. Fabre, F. Amiranoff, C. Garban-Labaune, J. Virmont, M. Weinfeld, and C.E. Max, Phys. Rev. A **26** 2289(R) (1982).
- ⁵⁰ W. Grigsby, "Experimental Studies of High Energy Density Silicon Using Ultra-Fast Lasers," Ph.D. thesis, University of Texas at Austin, 2007.
- ⁵¹ C.E. Max, C.F. McKee and W.C. Mead Phys Rev. Lett **45** 28 (1980); C. E. Max, , J. D. Lindl and W. C. Mead, Nucl. Fusion **23** 131 (1983).
- ⁵² J. Lindl, Phys. of Plasmas, **2** 3933 (1995).
- ⁵³ P. Mora Phys. of Fluids **25**, 1051 (1982).
- ⁵⁴ Z. Henis and S. Eliezer, Phys. Review E **48**, 2094 (1993).
- ⁵⁵ S. Eliezer , Y. Gazit Journal of Appl. Physics **68**(1): 356. (1990).
- ⁵⁶ D. Batani, H. Stabile, A. Ravasio, G. Lucchini, F. Strati, T. Desai, J. Ullschmied, E. Krousky, J. Skala, L. Juha, B. Kralikova, M. Pfeifer, Ch. Kadlec, T. Mocek, A. Präg, H. Nishimura, and Y. Ochi Phys. Rev E **68**, 067403 (2003).
- ⁵⁷ G. E. Duvall and R. A. Graham, Rev. Mod. Phys. **49**, 523 (1977).
- ⁵⁸ Ya. B. Zel'dovich and Y.P. Raizer, Physics of Shock Waves and High- Temperature Hydrodynamic Phenomena (Academic, New York, 1966), Chapters. I , XI.

-
- ⁵⁹ P. Ehrenfest, Supplement No. 75b zu den Mitteilungen aus dem Kamerlingh Onnes-Institut, Leiden (1933).
- ⁶⁰ S Eliezer and Z Henis Applications of Laser Plasma Interactions (CRC Press, 2008) Ed. S Eliezer and K. Mima Chap 6 p212.
- ⁶¹ A. Al-Zein, P. Bouvier, A. Kania, C. Levelut, B. Hehlen, V.Nassif, T.C. Hansen, P.Fertey, J.Haines and J. Rouquette Journal of Phys. D: Appl. Phys., **48**, 504008 (2015).
- ⁶² T. Deschamps, C. Martinet, J.L.Bruneel and B. Champagnon, J. Phys CM **23**, 035402 (2011).
- ⁶³ D.B.Hayes, Journal of App. Phys **45** 1208 (1974).
- ⁶⁴ L. M. Barker and R.E. Hollenbach, Journal of App. Phys. **43** 4669 (1972).
- ⁶⁵ T. d'Almeida and Y. M. Gupta, Phys. Rev. Lett. **85** 330 (2000).
- ⁶⁶ A. Ng, P. Celliers, and D. Parfeniuk Phys. Rev. Lett. **58**, 214 1987; P. Celliers, A. Ng, G. Xu, and A. Forsman, Phys. Rev. Lett. **68**, 2305 (1992); A. Ng and T. Ao, Phys. Rev. Lett. **91**, 035002 (2003). P. Celliers, "Dynamics of Laser-Driven Shock Waves in Fused Silica", Ph.D Thesis, The University of British Columbia, (1987).
- ⁶⁷ A. Loveridge-Smith, A. Allen, J. Belak, T. Boehly, A. Hauer, B. Holian, D. Kalantar, G. Kyrala, R.W.Lee, P. Lomdahl, M. A. Meyers, D. Paisley, S. Pollaine, B. Remington, D. C. Swift, S. Weber and J. S. , Phys. Rev. Lett. **86**, 2349 (2001).
- ⁶⁸ A. Gleason, C. Bolme, H. Lee, B. Nagler, E. Galtier, D. Milathianaki, J. Hawreliak, R. Kraus, J. Eggert, D. Fratanduono, G. Collins, R. Sandberg, W. Yang, and W. Mao, Nature Commun. **6**, 8191 (2015).
- ⁶⁹ R. G. Trainor and Y. T. Lee, Phys. Fluids **25**, 1898 (1982).
- ⁷⁰ T. R. Boehly *et al*, Opt. Comm. **133**, 495 (1987).
- ⁷¹ A.S. Joshi, C. P. Navathe, M. S. Ansari, M. P. Kamath, S. Bandhyopadhyay, A. Upadhyay, A. P. Kulkarni, P. K. Tripathi, S. R. Patwa, J. D. Singh, N. Sreedhar, R. Chandra, M. N. Kumbhare, H. C. Pant, Fusion Engineering and Design **44**, 67 (1999).
- ⁷² E. M. Campbell, J. T. Hunt, E. S. Bliss, D. R. Speck, R. P. Drake, Rev. Sci. Instrum. **57**, 2101 (1986).
- ⁷³ G. Cheriaux, P. Rousseau, F. Salin, and J. P. Chambaret, Opt. Lett. **21**, 414 (1996).
- ⁷⁴ M. P. Kamath, P. K. Tripathi, A. P. Kulkarni, S. Jain, S. R. Patwa, R. Chandra, A. S. Joshi, C. P. Navathe and P. D. Gupta, Sadhana **33**, 443 (2008)
- ⁷⁵ E. Spence, P. N. Kean, and W. Sibbett, Opt. Lett. **60**, 42 (1990).
- ⁷⁶ E. Treacy, IEEE J. Quant. Electr. **5**, 454 (1969).
- ⁷⁷ E. Siegman, "Lasers", University Science books, USA, p. 359 (1986).
- ⁷⁸ Brun. P. Georges, G. Le Saux, and F. Satin, J. Phys. D: Appl. Phys. **24**, 1225 (1991).
- ⁷⁹ C.R. Petruck, R. Jimenez, T. Guo, A. Cavalleri, C.W. Siders, F. RaÅ ksi, J A. Squier, B.C. Walker, K. R. Wilson, C.P. J. Barty, Nature **398**, 310 (1999).
- ⁸⁰ M. Lindenberg, I. Kang, S. L. Johnson, T. Missalla, P. A. Heimann, Z. Chang, J. Larsson, P. H. Bucksbaum, H. C. Kapteyn, H. A. Padmore, R.W. Lee, J. S. Wark, and R.W. Falcone, Phys. Rev. Lett. **84**, 111 (2000).
- ⁸¹ K. S. Tinten and D. von der Linde, J. Phys. Condensed Matter **16**, R1517 (2004).
- ⁸² K. Li, F. H. Séguin, J. A. Frenje, J. R. Rygg, R. D. Petrasso, R. P. J. Town, P. A. Amendt, S. P. Hatchett, O. L. Landen, A. J. Mackinnon, P. K. Patel, V. A. Smalyuk, T. C. Sangster, and J. P. Knauer, Phys. Rev. Lett. **97**, 135003 (2006). See also: C. K. Li, F. H. Séguin, J. R. Rygg, J. A. Frenje, M. Manuel, R. D. Petrasso, R. Betti, J. Delettrez, J. P. Knauer, F. Marshall, D. D. Meyerhofer, D. Shvarts, V. A. Smalyuk, C. Stoeckl, O. L. Landen, R. P. J. Town, C. A. Back, and J. D. Kilkenny, Phys. Rev. Lett. **100**, 225001 (2008).
- ⁸³ J.R. Rygg, F.H. Séguin, C.K. Li, J.A. Frenje, M.J.-Manuel, R.D. Petrasso, R. Betti, J.A. Delettrez, O.V. Gotchev, J.P. Knauer, D.D. Meyerhofer, F.J. Marshall, C. Stoeckl, W. Theobald, Science **318**, 1223 (2008).
- ⁸⁴ R. Fedosejevs, I. V. Tomov, N. H. Burnett, G. D. Enright, and M. C. Richardson, Phys. Rev. Lett **39**, 932 (1977).
- ⁸⁵ E Takahashi, I Matsushima, Y Matsumoto, I Okuda, Y Owadano, Opt.Comm. **150**, 56 (1998).
- ⁸⁶ H. Houtman, L. E. Legault, and J. Meyer, Applied Optics **26**, 1106 (1987).

-
- ⁸⁷ J. A. Stamper, E. A. McLean, and B. H. Ripin, Phys. Rev. Lett **40**, 1177 (1978).
- ⁸⁸ J. A. Stamper and B.H. Ripin, Phys. Rev. Lett. **34**, 138 (1975).
- ⁸⁹ L.T. Hang, H.Z. Qiang, G. Xun, L.Z. Hao and L.J. Quan, Chin. Phys. B **23**, 085203 (2014).
- ⁹⁰ M.P Kamath, A.P Kulkarni, S Jain, P.K. Tripathi, A.S. Joshi, P.A. Naik and P.D. Gupta, Pramana **75**, 883 (2010).
- ⁹¹ M.C. Kaluza, M.I.K. Santala, J. Schreiber, G.D. Tsakiris, and K.J. Witte, Appl. Phys B **92**, 475 (2008).
- ⁹² A.S. Joshi, P.A. Naik, S. Barnwal, Y.B.S.R. Prasad and P.D. Gupta, Opt. Comm. **283**, 4713 (2010).
- ⁹³ S Kahaly, S. Mondal, G.R Kumar, S. Sengupta, A. Das and P.K. Kaw, Phys. Plasmas **16**, 043114 (2009).
- ⁹⁴ G. M. Maaswinkel, R. Sigel, H. Baumhacker, and G. Brederlow, Rev. Sci. Instrum. **55**, 48 (1984)
- ⁹⁵ J. Meyer and H. Houtman, Phys. Plasmas **3**, 745 (1991).
- ⁹⁶ Y.B.S.R. Prasad, P.A. Naik, A. Kumar, and P. D. Gupta, Rev Sci. Instrum **77**, 093106 (2006).
- ⁹⁷ A. Gopal, *Measurements of ultra strong fields in laser produced plasmas*, Ph.D. Thesis, Imperial College London (University of London), 2004.
(<https://workspace.imperial.ac.uk/plasmaphysics/Public/GopalPhD.pdf>)
- ⁹⁸ A. Gopal, S. Minardi, M. Burza, G. Genoud, I. Tzianaki, A. Karmakar, P. Gibbon, M. Tatarakis, A. Persson and C-G. Wahlström, Plasma Phys. Control. Fus. **55**, 035002 (2013).
- ⁹⁹ Ng, B.K. Godwal, J. Waterman, L. DaSilva, N. W. Ashcroft and R. Jeanloz, Phys. Rev. B **44**, 4872 (1991).
- ¹⁰⁰ Y. Chien, B. La Fontaine, A. Desparois, Z. Jiang, T. W. Johnston, J. C. Kieffer, H. Pepin, and F. Vidal, Opt. Lett. **25**, 578 (2000).
- ¹⁰¹ J.-P. Geindre, P. Audebert, S. Rebibo, and J.-C. Gauthier, Opt. Lett. **26**, 1612 (2001).
- ¹⁰² Batani, S.D. Baton, M. Manclossi, D. Piazza, M. Koenig, A. Benuzzi-Mounaix, H. Popescu, C. Rousseaux, M. Borghesi, C. Cecchetti, and A. Schiavi, Phys. Plasmas **16**, 033104 (2009).
- ¹⁰³ Benuzzi-Mounaix, M. Koenig, and J. M. Boudenne, T. A. Hall, D. Batani, F. Scianitti, A. Masini, and D. Di Santo, Phys. Rev. E **60**, R2488 (1999).
- ¹⁰⁴ J. Psikal, V. T. Tikhonchuk, J. Limpouch, and O. Klimo, Phys. Plasmas **17**, 013102 (2010).
- ¹⁰⁵ N.Vogel, Appl. Surf. Science **252**, 4850 (2006).
- ¹⁰⁶ G.R. Kumar, S. Kahaly, J. Sinha, S. Mohan, and S. S. Banerjee, J. Phys: Conf. Series **112**, 022083 (2008).
- ¹⁰⁷ M. Tatarakis, F. N. Beg, E. L. Clark, A. E. Dangor, R. D. Edwards, R.G. Evans, T. J. Goldsack, K.W. D. Ledingham, P. A. Norreys, M. A. Sinclair, M-S. Wei, M. Zepf, and K. Krushelnick, Phys. Rev. Lett. **90**, 175001 (2003).
- ¹⁰⁸ Chen, S. C. Wilks, W. L. Kruer, P. K. Patel, and R. Shepherd, Phys. Plasmas **16**, 020705 (2009).
- ¹⁰⁹ L. Clark, K. Krushelnick, M. Zepf, F. N. Beg, M. Tatarakis, A. Machacek, M. I. K. Santala, I. Watts, P. A. Norreys, and A. E. Dangor, Phys. Rev. Lett. **85**, 1654 (2000).
- ¹¹⁰ S. C. Wilks, A. B. Langdon, T. E. Cowan, M. Roth, M. Singh, S. Hatchett, M. H. Key, D. Pennington, A. MacKinnon, and R. A. Snavely, Phys. Plasmas **8**, 542 (2001).
- ¹¹¹ S. Sakabe, S. Shimizu, M. Hashida, F. Sato, T. Tsuyukushi, K. Nishihara, S. Okihara, T. Kagawa, Y. Izawa, K. Imasaki, and T. Iida, Phys. Rev. A **69**, 023203 (2004).
- ¹¹² Schwoerer, S. Pfoth, O. Jackel, K.-U. Amthor, B. Liesfeld, W. Ziegler, R. Sauerbrey, K. W. D. Ledingham, and T. Esirkepov, Nature **439**, 445 (2006).
- ¹¹³ Y. Sentoku, T. E. Cowan, A. Kemp, and H. Ruhl, Phys. Plasmas **10**, 2009 (2003).
- ¹¹⁴ Y. Okano, Y. Hironaka, K. G. Nakamura, and K. Kondo, Appl. Phys. Lett. **83**, 1536 (2003).
- ¹¹⁵ K. L. Lancaster, J. Pasley, J. S. Green, D. Batani, S. Baton, R. G. Evans, L. Gizzi, R. Heathcote, C. H. Gomez, M. Koenig, P. Koester, A. Morace, I. Musgrave, P. A. Norreys, F. Perez, J. N. Waugh, and N. C. Woolsey, Phys. of Plasmas **16**, 056707 (2009).
- ¹¹⁶ Malka, Ph. Nicolai, E. Brambrink, J. J. Santos, M. M. Aléonard, K. Amthor, P. Audebert, J. Breil, G. Claverie, M. Gerbaux, F. Gobet, F. Hannachi, V. Méot, P. Morel, J. N. Scheurer, M. Tarisien, and V. Tikhonchuk, Phys. Rev. E **77**, 026408 (2008).
- ¹¹⁷ B. Foldes, K. Koyama, R. Sigel, G. D. Tsakiris, A. Boswald, C. S. Shengs, A. G. M. Maaswinkel, R. F. Schmalz, and S. Witkowski, Europhys. Lett. **2**, 221 (1986).

-
- ¹¹⁸ Paul Gibbon, *Short Pulse Laser Interactions with matter an introduction*, Imperial College Press, Chap-5 (2005).
- ¹¹⁹ R. Benattar, J.P. Geindre, P. Audebert, J. C. Gauthier, A. Mysyrowiez, J. P. Chambaret and A. Antonetti, *Opt. Comm.* **88**, 376 (1992).
- ¹²⁰ X. Zeng, X. Mao, Sy-BorWen, R. Greif and R. E. Russo, *J. Phys. D: Appl. Phys.* **37**, 1132 (2004).
- ¹²¹ D.G. Colombant and N.K. Winsor, *Phys. Rev. Lett.* **38**, 697 (1977).
- ¹²² A. Raven, P. T. Rumsby, J. A. Stamper, O. Willi, R. Illingworth and R. Thareja, *Appl. Phys. Lett.* **35**, 526 (1979).
- ¹²³ G. Shvets, Fisch and J.M. Rax, *Phys. Rev. E.* **65**, 046403 (2002); J. Deschamps, M. Fitaire and M. Lagoutte, *Phys. Rev. Lett.* **25**, 1330 (1970).
- ¹²⁴ J. Fuchs, G. Malka, J. C. Adam, F. Amiranoff, S. D. Baton, N. Blanchot, A. Héron, G. Laval, J. L. Miquel, P. Mora, H. Pépin, and C. Rousseaux, *Phys. Rev. Lett.* **80**, 1658 (1998).
- ¹²⁵ G. R. Kumar, *J. Phys: Conf. Series* **244**, 012008 (2010).
- ¹²⁶ R.J. Mason, *Phys. Rev. Lett.* **42**, 239 (1979).
- ¹²⁷ H. Daido, F. Miki, K. Mima, M. Fujita, K. Sawai, H. Fujita, Y. Kitagawa, S. Nakai, and C. Yamanaka, *Phys. Rev. Lett.* **56**, 846 (1986).
- ¹²⁸ B.H. Ripin, E. A. McLean, C. K. Manka, C. Pawley, J. A. Stamper, T. A. Peyser, A. N. Mostovych, J. Grun, A. B. Hassam, and J. Huba, *Phys. Rev. Lett.* **59**, 2299 (1987).
- ¹²⁹ M.G. Drouet and H. Pepin, *Appl. Phys. Lett.* **28**, 426 (1976).
- ¹³⁰ Y. Sakagami, H. Kawakami, and C. Yamanaka, *Phys. Rev. A* **21**, 882 (1980).
- ¹³¹ J. Briand, J.C. Kieffer, A. Gomes, C. Arnas, J.P. Dinguirard, Y. Quemener, L. Berge, M.El Tamer, and M. Armengaud, *Phys. Fluids* **30**, 2893 (1987); B. B. Pollock, D.H. Froula, P.F. Davis, J.S. Ross, S. Fulkerson, J. Bower, J. Satariano, D. Price, K. Krushelnick, and S.H. Glenzer, *Rev. Sci. Instrum.* **77**, 114703 (2006).
- ¹³² M.D.J. Burgess, B. Luther-Davies and K. A. Nugent, *Phys. Fluids* **28**, 2286 (1985).
- ¹³³ E. Bolkhovitinov, I. A. Krayushkin, A. A. Rupasov, S. I. Fedotov and A. S. Shikanov, *Instrum. and Exptl. Techn.* **50**, 379 (2007).
- ¹³⁴ A. S. Sandhu, A.K. Dharmadhikari, P.P. Rajeev, G.R.Kumar, S. Sengupta, A. Das, and P.K. Kaw *Phys. Rev. Lett.* **89**, 225002, (2002).
- ¹³⁵ T. S. Pisarczyk, R. Arendzikowski, P. Parys and Z. Patron, *Laser and Particle Beams* **12**, 549 (1994); T. Pisarczyk, A. A. Rupasov, A.S. Sarkisov and A. S. Shikanov, *J. Soviet. Laser Res*, **11**, 1 (1990).
- ¹³⁶ L. Dubrovinsky, N. Dubrovinskaia, V.B. Prakapenka and A.M. Abakumov, *Nature Communications* **3**, 1163 (2012).
- ¹³⁷ L.C. Chhabildas and M.D. Knudson, *High-Pressure Shock Compression of Solids VIII: The Science and Technology of High-Velocity Impact*, edited by L.C. Chhabildas, Lee Davison, Y. Horie, Springer, Berlin, Chap. 4, p 143 (2005).
- ¹³⁸ W. D. Reinhart, L. C. Chhabildas, D. E. Carroll, T. G. Thornhill and N. A. Winfree, *International Journal of Impact Engineering*, **26**, 625 (2001).
- ¹³⁹ D. Batani, A. Balducci, D. Beretta, A. Bernardinello, T. Lower, M. Koenig, A. Benuzzi, B. Faral and T. Hall, *Phys. Rev. B* **61**, 9287 (2000).
- ¹⁴⁰ W. Grigsby, B. T. Bowes, D. A. Dalton, A. C. Bernstein, S. Bless, M. C. Downer, E. Taleff, J. Colvin, and T. Ditmire, *J. Appl. Phys.* **105**, 0935231 (2009).
- ¹⁴¹ R. Cauble, D. W. Phillion, T. J. Hoover, N. C. Holmes, J. D. Kilkenny, and R. W. Lee, *Phys. Rev. Lett.* **70**, 2102 (1993).
- ¹⁴² L. R. Henderson, *Handbook of Shock Waves*, Vol 1, Academic Press, San Diego, CA, USA, Chap- 2. (2001).
- ¹⁴³ F. Cottet and J. P. Romain, *Phys. Rev. Lett.* **52**, 1884 (1984).

-
- ¹⁴⁴ T. R. Boehly, E. Vianello, J. E. Miller, R. S. Craxton, T. J. B. Collins, V. N. Goncharov, I. V. Igumenshchev, D. D. Meyerhofer, D. G. Hicks, P. M. Celliers and G. W. Collins , Phys. Plasmas **13**, 056303 (2006).
- ¹⁴⁵ R. Ecault R.L. Berthe, M. Boustie, F. Touchard, E. Lescoute, A. Sollier, P. Mercier and J. Benier, J. Phys. D: Applied Physics **46**, 235501 (2013).
- ¹⁴⁶ C.P.J. Barty, T. Guo, C. Le Blanc, F. Raksi, C. Rose-Petruck, J. Squier , Opt. Lett . **21**, 668 (1996).
- ¹⁴⁷ A.K. Sharma M. Raghuramaiah, K.K. Mishra, P.A. Naik, S.R. Kumbhare and P.D. Gupta, Opt. Comm. **252**, 369 (2005).
- ¹⁴⁸ E. Grady and L.C. Chhabildas , 1996 *Shock wave properties of soda lime glass* Report No: SAND-96-2571C, Sandia National Labs., Albuquerque, NM, United States.
- ¹⁴⁹ M. Koenig, B.Faral,J.M.Boudenne,D.Batani,A.Benuzzi and S.Bossi, Phys. Rev. E **50** R3314 (1994).
- ¹⁵⁰ Ya. B. Zeldovich and Yu. P. Raizer, 1967 *Physics of Shock Waves and High Temperature Hydrodynamic Phenomena* (Academic Press, New York).
- ¹⁵¹ R.Jeanloz and T.J.Ahrens *Pyroxenes and Olivines: Structural Implications of Shock-Wave Data for High pressure Phases* pg 446 from **High-Pressure Research: Applications in Geophysics** Ed Murli H. Manghnani, Syun-Iti Akimoto (Academic Press) 1977; Also R.Jeanloz, Fig. 4 on Page 44 from Thesis " *Physics of mantle and Core materials*", California Institute of Technology , 1979.
- ¹⁵² R. Fedosejevs , Y. Teng, R. Sigel, K. Eidmann and R. Petsch, J. Appl. Phys. **52**, 4186 (1981).
- ¹⁵³ R.F.Benjamin , G.H. McCall and A.W. Ehler, Phys. Rev . Lett. **42**, 890 (1979).
- ¹⁵⁴ J. L.Borowitz, S. Eliezer, Y. Gazit, M. Givon, S. Jacket, A. Ludmirsky, D. Salzmann, E. Yarkoni, A. Zigler and B Arad, J. Phys. D: Appl. Phys. **20**, 210 (1987).
- ¹⁵⁵ D.von der Linde and H.Schuler, J. Opt. Soc. Am. B **13**, 216 (1996).
- ¹⁵⁶ Z. Lin A. Lei W. Fan S. Zhou and Li Wang, High Power Laser Sci. and Engg. **1**, 110 (2013).
- ¹⁵⁷ O. Willi, P.T. Rumsby, C. Hooker, A. Raven and Z.Q.Lin , Opt. Comm. **41**, 110 (1982).
- ¹⁵⁸ M. Shukla, V.N. Rai, H.C. Pant, and D.D. Bhawalkar, *A picosecond Streak camera*, RRCAT Internal Report : CAT/I/2000-19, R2814 (2000).
- ¹⁵⁹ J. Upadhyay, B.Singh, M.L. Sharma and C.P. Navathe, *Development of PCI controlled Gated Grid Optical Streak Camera*, RRCAT Internal Report : RRCAT/2012-12 (2012)
- ¹⁶⁰ H. Azechi, S. Oda, K. Tanaka, T. Norimatsu, T. Sasaki, T. Yamanaka, and C. Yamanaka, Phys.Rev. Lett **39**, 1144 (1977).
- ¹⁶¹ W. Lochte, Holtgreven " Evaluation of Plasma Parameters" from "Plasma Diagnostics" North Holland p 135, (1968).
- ¹⁶² https://www.researchgate.net/publication/259156605_sgmfprogram